Impact de la dynamique à petite et moyenne échelles sur le devenir des particules exportées dans l'océan profond

Lu Wang

COLLEGE SCIENCES
DOCTORAL DE LA MER
BRETAGNE ET DU LITTORAL

UBO
Université de Bretagne Occidentale

THESE DE DOCTORAT DE

L'UNIVERSITE
DE BRETAGNE OCCIDENTALE

ECOLE DOCTORALE N° 598
Sciences de la Mer et du Littoral
Spécialité : *Océanographie physique et environnement*

Par
Lu WANG

Impacts of mesoscale and submesoscale dynamics on the fate of exported particles to the deep ocean

Thèse présentée et soutenue à Brest, le 22 mai 2024
Unité de recherche : LEMAR / LOPS

Rapporteurs avant soutenance :

Guillaume LAPEYRE	DR CNRS, LMD, Paris
Adrian MARTIN	Prof., NOCS, Southampton, GB

Composition du Jury :

Président :	Xavier CARTON	Prof UBO, LOPS, Brest
Examinateurs :	Amala MAHADEVAN	Prof., WHOI, Woods Hole USA
Dir. de thèse :	Laurent MEMERY	DR CNRS, LEMAR, Brest
Co-dir. de thèse :	Jonathan GULA	MC UBO, LOPS, Brest

Invité(s)

Andrea DOGLIOLI	Prof. AMU, MIO, Marseille
Lionel GUIDI	DR CNRS, LOV, Villefranche/mer

Acknowledgements

My PhD started a few months before the onset of the COVID-19 pandemic, a period that presented numerous challenges and uncertainties. Nonetheless, life has been back on track, and I made my PhD to the finish line. Here I would like to express my gratitude to the exceptional individuals who supported and guided me throughout this journey, enabling me to successfully obtain my doctorate despite the many unforeseen obstacles that arose.

First and foremost, I would like to thank my PhD supervisors, Dr. Laurent Mémery and Prof. Jonathan Gula, for their constant support, guidance, and encouragement throughout the entire process. From the initial stages of refining my research to the final submission of my thesis, their unwavering presence and wealth of wisdom have been instrumental in shaping my academic growth. The weekly meetings we held were highly valuable and helpful. These meetings, even part of them were online for a few months during the pandemic, not only served as crucial checkpoints to keep me on track but also provided me with plenty of inspiration and encouragement. Although I went through a long difficult time before and after I came back to China, my supervisors understood and supported me all the time. I cannot complete the PhD without such wonderful supervisors.

In addition to my supervisors, I would like to express my special thanks to the scientific engineer of my project, Jérémy Collin. He consistently assisted me with my technical issues throughout my PhD, in person or online, no matter where I was. He also contributed a lot to my first paper and the PhD thesis. I appreciate his efforts in helping me deal with the questions proposed by reviewers on the technical side and his thoughtful suggestions for my paper and thesis. I also thank Mathieu Le Corre for providing outputs of the POLGYR simulation, and Clément Vic for helping me with the code of computing particle dispersion in the first part of my work.

I would also like to thank my Individual Supervisory Committee (CSI), Prof. Andrea M. Doglioli and Dr. Lionel Guidi. Thank you for your advice and encouragement during my annual CSI meetings. Your kind words and suggestions are valuable to my PhD time.

I want to thank my office mates, Anais Medieu and Lucien Besnard, for their help in my first year. We had a great time in the office with chocolate and laughter.

Huge thanks to my friends. First I would like to thank Yingjie Liu, for your accompany in both worktime and daily life. I remember the courses we attended together in the first year, the news we shared on the bus, the walks near the lab after lunch, and our trips to Paris and towns near Brest. Thanks to Yingjie Liu and Yue Cheng for inviting me to the parties held at your apartment, I enjoyed the food and drinks, songs and dance, and girl talks during those happy nights. Thanks to Hong Chin Ng for your accompany at the lab and on the tram, for your kind help during the week when I got COVID, and for the happiness you brought to us at Yingjie and Yue's place. Thanks to Li Ji and Tao Jing, for the delicious meals at your home, for our good time at the beach and in the forest, and for your help in my life. Thanks to the best friend I met in the UK, Yue Wu, you fully understand my feelings for research and future career, and you are always there to listen and comfort me. Thanks to my friend since my childhood, Ziwei Zhao, the chat and phone calls with you made me peaceful and clear. Your enthusiasm for research and life has encouraged me a lot during the past year.

Lastly, I want to express my appreciation to my parents, Jun Wang and Lijun Wu. Thank you for everything, especially your unconditional support for the eight years when I was abroad to study. I'm sorry for my absence from being with you during the pandemic. Your love and encouragement provided emotional support for my PhD. I also want to thank my little brother, Xinke Wang, for your company with mom and dad during my absence in these years.

My deepest gratitude goes to my husband, Xiaolong Yu, who is the most important person in my life. We have been together for almost nine years and in marriage for six years. We spent a lot of great time in the UK and France. Thank you for your endless love and support. You are not only a good husband in daily life, but also an excellent model in research. I hope we can work together after my PhD, moving forward to a bright future for both of us.

Abstract

An important route in the biological carbon pump is gravitational sinking particles which export the organic carbon produced by photosynthesis to the ocean interior. Long-term observations of the downward particle flux are mainly made by deep-moored sediment traps. In this thesis, impacts of mesoscale and submesoscale dynamics on the export of fast-sinking particles ($\geq$20 m day^{-1}) are investigated through backward and forward Lagrangian particle tracking experiments, using outputs from a 2-km resolution simulation of the North Atlantic Ocean over 7 years. The study area is an open ocean region in the Northeast Atlantic, centered around the long-term observatory PAP site (16.5°W, 49.0°N).

The backward simulations show that mesoscale eddies can transport particles from hundreds of kilometers to sediment traps at the PAP site. The vertical profile of 7-year integrated particle trajectories is related to changes in EKE and vertical flows, mostly in the twilight zone (200-1000 m). The variability of monthly particle sources shows a locally dominant eddy at the PAP site can significantly trap particles within a small region. The anticyclonic eddies accelerate particle sinking by downward velocities in strain-dominated structures, while the upward velocities in the vortex of cyclonic eddies decelerate particles. Starting with a homogeneous seeding of particles at 200 m, the forward simulations reveal that the seasonality and spatial variability of particle collections at 1000 m can result from the physical dynamics only. Particles collected within a 200 $\times$ 200 km target zone are grouped into 9 clusters using a machine learning clustering algorithm. The seasonal variations of particle amounts in clusters active in winter-spring time are related to the mesoscale eddy activities and the development of fronts. In autumn and early winter, the local background flow (defined by low eddy and frontal activities) contributes most to the particle collection. The heterogeneous spatial patterns of particle collection display a large-scale meridional gradient over the 7 years and more patchiness increasing towards a shorter sampling scale.

Overall, this study investigates the impacts of dynamics in the twilight zone on particles collected in the deep ocean from two different points of view. It also demonstrates how mesoscale dynamics impact the heterogeneity of particle distribution, and thus collection in the deep ocean. The findings have implications for the sampling design and data interpretation during regional surveys to study the biological carbon pump.

Abstract

Les particules qui sédimentent par gravité et exportent le carbone organique produit par la photosynthèse vers l'intérieur de l'océan constituent une voie importante de la pompe biologique de carbone. Les observations à long terme du flux de particules qui sédimentent sont principalement effectuées par des pièges à particules profonds. Dans cette thèse, les impacts de la dynamique à mésoéchelle et à sous-mésoéchelle sur l'export de particules qui s'enfoncent rapidement ($\geq$20 m jour^{-1}) sont étudiés par le biais d'expériences de suivi lagrangien de particules, backward et forward, en utilisant les résultats d'une simulation à 2 km de résolution de l'océan Atlantique Nord sur une période de 7 ans. La zone d'étude est une région en océan ouvert dans l'Atlantique Nord-Est, centrée autour du site de l'observatoire à long terme PAP (16,5°W, 49,0°N).

Les rétrotrajectoires montrent que les tourbillons de mésoéchelle peuvent transporter des particules sur des centaines de kilomètres jusqu'aux pièges à particules du site PAP. Le profil vertical des trajectoires intégré sur 7 ans est associé aux changements de propriété de l'EKE et des flux verticaux, principalement dans la zone mésopélagique (200-1000 m). La variabilité mensuelle des sources de particules montre qu'un tourbillon localement dominant sur le site PAP peut piéger efficacement les particules dans un domaine restreint. Les tourbillons anticycloniques accélèrent la sédimentation des particules par des vitesses descendantes dans les structures dominées par de fortes déformations, tandis que les vitesses ascendantes dans le vortex des tourbillons cycloniques décélèrent les particules. En partant d'un ensemencement homogène de particules à 200 m, les simulations forward révèlent que la saisonnalité et la variabilité spatiale des collectes de particules à 1000 m peuvent résulter uniquement de la dynamique océanique. Les particules recueillies dans une zone cible de 200 $\times$ 200 km sont regroupées en 9 classes à l'aide d'un algorithme d'apprentissage automatique. Les variations saisonnières du nombre de particules dans les classes majoritaires en hiver et au printemps sont liées aux activités tourbillonnaires à mésoéchelle et au développement des fronts. En automne et au début de l'hiver, les classes les plus importantes de particules sont avant tout associées à une dynamique local 'de fond' (définie par de faibles activités tourbillonnaires et frontales). Les structures spatiales hétérogènes de la distribution de particules présentent un gradient méridien à grande échelle en moyenne sur les sept années simulées et une plus grande disparité à mesure que l'échelle temporelle d'échantillonnage diminue.

Dans l'ensemble, cette étude examine les impacts de la dynamique dans la zone mésopélagique sur les particules récoltées dans l'océan profond de deux points de vue différents. Elle démontre également l'impact de la dynamique à méso-échelle sur l'hétérogénéité de la distribution des particules, et donc sur leur collecte dans l'océan profond. Les résultats ont des implications dans la stratégie de l'échantillonnage et l'interprétation des données lors des campagnes régionales visant à étudier la pompe biologique de carbone.

Contents

Chapter 1

Introduction

This chapter gives a research background of the thesis. It starts with the role of oceanic carbon cycle in the context of global climate change. The main part consists of the introduction of biological carbon pump, followed by a review of mesoscale and submesoscale dynamics and their biogeochemical impacts. An overview of Lagrangian ocean analysis and its application on carbon export are also introduced. Lastly, the aim and objectives of this thesis are provided with a brief outline of the rest chapters.

1.1 In a broad context

Carbon is one of the most vital elements in the earth's system for its indispensable role in living organisms and their environments. The carbon cycle is a complex network where myriad processes exchange and transform carbon among different reservoirs. Compared to long-term carbon storage at time scales of millions of years in the geological reservoir (lithosphere), carbon cycles in the atmospheric, terrestrial, and oceanic reservoirs have much shorter time scales ranging from hours to thousands of years. Therefore, these reservoirs can react more efficiently to perturbations in the global carbon cycle (Sarmiento and Gruber, 2006).

Carbon dioxide (CO_2) is the most important greenhouse gas on Earth because it absorbs and radiates heat so that the average global surface temperature can be kept above freezing. However, excess CO_2 to the atmosphere supercharges the natural greenhouse effect, consequently increasing global temperature. The amount of atmospheric CO_2 shows a long-term trend of rising levels associated with anthropogenic emissions, primarily due to burning fossil fuels since the Industrial Revolution in the 18th century (NOAA Climate.gov). The CO_2 increase over the last 60 years is 100 times faster than any previous natural increases (Lüthi et al., 2008). In 2021, the global average carbon dioxide was 414.72 parts per million (ppm) which sets a new record high (data from NOAA's Global Monitoring Lab).

The ocean is thought to be the largest active CO_2 sink in the global carbon cycle. It takes up atmospheric CO_2 through two primary mechanisms, the "Solubility Pump" and the "Biological Carbon Pump (BCP)" (Volk and Hoffert, 1985). The former is based on the equilibration of CO_2 concentration between the atmosphere and the surface ocean. Depending on the gradient of the partial pressure of CO_2 (pCO_2) across the sea surface, atmospheric CO_2 can physically dissolve into the ocean. The cold, dense water rich in dissolved inorganic carbon (DIC) is delivered to depth. The latter mechanism, BCP, is conducted by oceanic primary producers via photosynthesis. Dissolved CO_2 is transformed into organic carbon in the surface ocean, subsequently exported as biogenic particles and dissolved organic matter to the ocean interior where carbon can be sequestered from the atmosphere on time scales of months to millennia. This procedure is defined as "carbon export". The biological pump exports particulate organic carbon (POC) globally, whereas the solubility pump operates mainly at high latitudes (Boyd et al., 2019).

The BCP has been estimated to account for about two-thirds of the vertical gradient of carbon in the ocean, while the rest is attributed to the solubility pump (Passow and Carlson, 2012). Carbon flux associated with BCP is estimated between ∼5 and 20 Gt Cyr^{-1} (Eppley and Peterson, 1979; Henson et al., 2011), comparable to the magnitude of current carbon emissions from fossil fuels (∼15 to 40 Gt Cyr^{-1}, data from the Global Carbon Project). The pre-industrial atmospheric CO_2 level would be 200 ppm (almost 100%) higher than the estimated value of 280 ppm before the anthropogenic CO_2 increase in the scenario without BCP (Parekh et al., 2006). Thus, advancing our knowledge of BCP is essential to understanding its role in the global carbon cycle under climate change.

1.2 Biological Carbon Pump

1.2.1 Definition and mechanisms

The BCP is a multifaceted system driven by a suite of processes in the ocean that remove photosynthetically produced organic carbon from the surface layer to depth. Figure 1.1 shows a schematic of the BCP with key components and processes involved. It can be simplified into three phases - production, transport, and remineralization. Phytoplankton utilizes sunlight and nutrients to convert CO_2 into organic carbon. At the transport stage, three primary pathways are responsible for carbon export. A significant vehicle is the gravitational sinking of particles (Boyd and Trull, 2007), known as the "Gravitational Pump". Zooplankton grazes on phytoplankton, and their fecal pellets along with dead organisms, form aggregates sinking toward the deep ocean. An alternative export pathway is the "Migrant Pump" which refers to the active transport of carbon by diel and seasonal vertical migrators in the water column (Bianchi et al., 2013; Jónasdóttir et al., 2015). The third pathway, known as "Mixing Pump" is the passive transport of non-sinking forms of organic carbon, mediated by physical processes such as subduction (Omand et al., 2015), advection and diffusion (Stukel and Ducklow, 2017). During the descending process, microbial organisms, zooplankton, and other heterotrophs consume and remineralize most particles, which return CO_2 to the seawater.

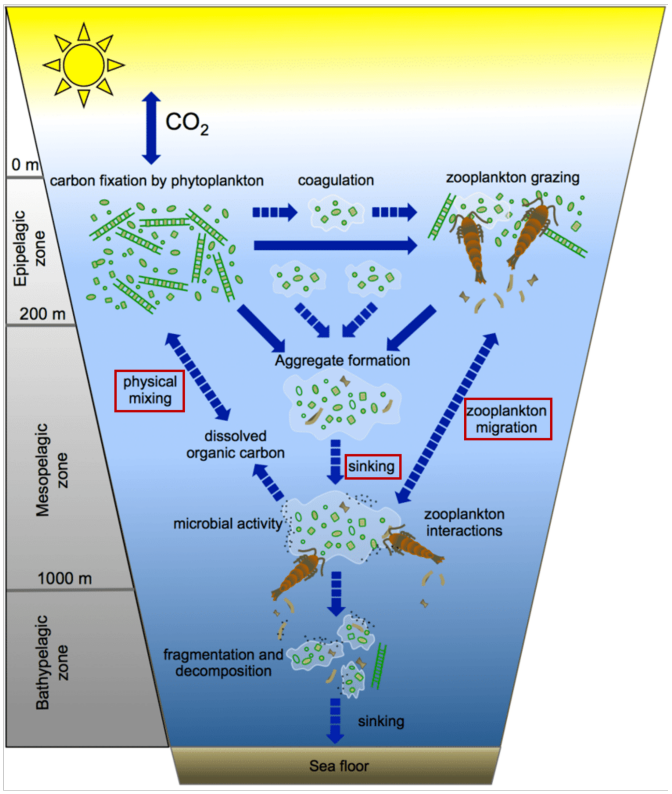

FIGURE 1.1: A simplified diagram of the biological carbon pump showing principal components and processes. Figure from Puigcorbé Lacueva (2016).

1.2.2 The strength and efficiency

As noted on the left side of Figure 1.1, processes in BCP take place across different layers of the water column. After the POC production in the epipelagic zone (or "euphotic zone", 0-200 m), the downward carbon flux is transported and remineralized in the mesopelagic layer ("twilight zone", 200-1000 m) or probably deeper in the bathypelagic zone. The gravitational pump is a crucial link between the upper-ocean POC production, the mid-water carbon consumption by biota, and interior carbon storage (Boyd et al., 2019). Its strength and efficiency collectively impact the capability of biological carbon sequestration, highlighting the pivotal role the twilight zone plays in the BCP. The strength of the gravitational pump is the rate of particle export from the euphotic zone, the mixed layer, or a fixed depth (Buesseler and Boyd, 2009). The downward flux attenuates with depth due to the multiple recycling processes that particles undergo as they descend. In the first order, the vertical attenuation of particle flux is described using a power-law relationship known as the "Martin curve" (Martin et al., 1987).

The efficiency refers to the time that carbon is stored within the ocean interior out of contact with the atmosphere. The BCP has both short-term (months to decades) and long-term (centuries to millennia) effects on carbon storage. The remineralization depth (or the remineralization length scale, RLS) of exported carbon determines the timescale of carbon removal and hence the extent of carbon storage in the interior (Figure 1.2). The POC remineralized at a few hundred meters is circulated back to the atmosphere within 10 years. It takes 100 years for the POC entering the mesopelagic layer to be returned, and the carbon can be sequestered for up to 1000 years once sinking below 1000 m (Passow and Carlson, 2012). In reality, the critical depth in BCP varies regionally as the winter mixed layer depth (MLD) spans a wide range. For instance, the winter MLD in the subpolar region of the North Atlantic can be around 1000 m (de Boyer Montégut et al., 2004). It means that in some regions, the local POC export is supposed to reach well below the mesopelagic layer for long-term carbon removal from the atmosphere.

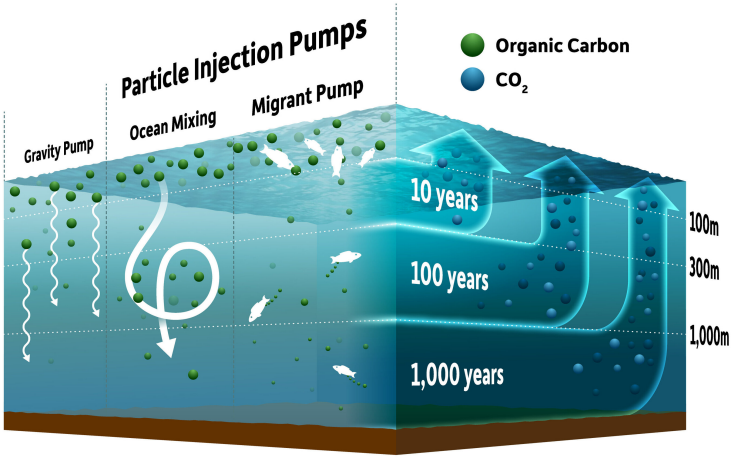

FIGURE 1.2: Time scales of organic carbon sequestered at different depths returning to the ocean surface layer as CO_2. (Image courtesy of University of Rochester illustration / Michael Osadciw)

1.2.3 Sampling the downward particle flux

A direct method to quantify the downward flux of organic particles is the deployment of underwater equipment (Figure 1.3). Large water samplers and Niskin bottles associated with the CTD rosette are deployed to collect water samples at specific depths during research cruises. Only dissolved matter or small particles

with low sink rates are sampled in this way. Time-series measurements are conducted using devices called "sediment traps" designed like rain gauges equipped at a certain depth to collect falling particles. The device consists of a cylindrical or conical funnel for trapping and transferring sediment particles to individual sample bottles switching at time intervals. Sediment traps are currently the most commonly used means of assessing the amount and types of particles exported from surface waters. Among a set of trap designs, only the prolonged sediment trap moorings can be used to measure the downward particle flux to the deep ocean since collecting enough particles for a sample in deep water takes a long time. The time resolution of sediment trap sampling is often between one and two weeks for the long-term mooring lasting at least one year, and several hours for specific process studies during a cruise. Over the past decades, there have been numerous studies based on the sampling by deep-moored sediment traps deployed below 1000 m at sustained observatory sites (Wong et al., 1999; Steinberg et al., 2001; Lampitt et al., 2010) and process study stations spanning a wide range of the global ocean (Boyd and Newton, 1995; Lampitt and Antia, 1997; Francois et al., 2002). These studies reveal strong regional and temporal variations of the downward particle flux, which provides insights into the link between upper ocean processes and deep ocean carbon fluxes.

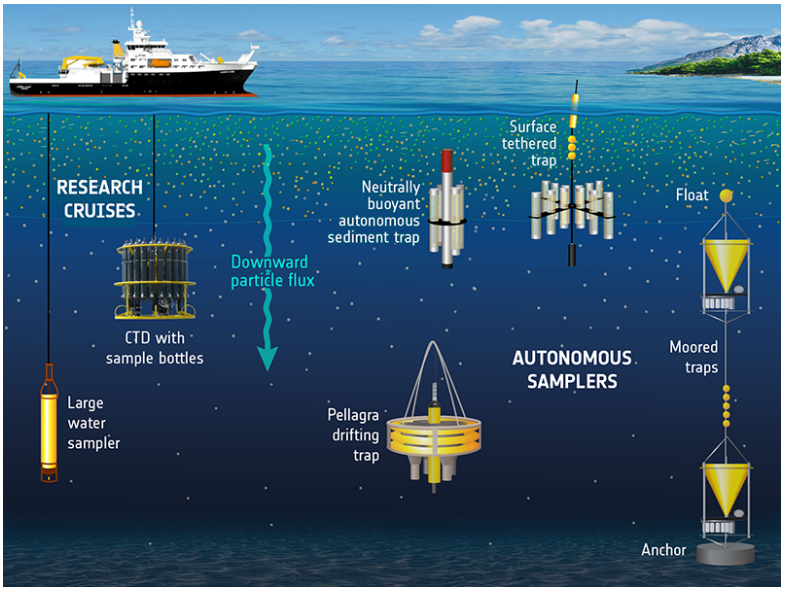

FIGURE 1.3: Sampling tools to measure the downward particle flux. (Image courtesy of NOC/V.Byfield)

1.3 Mesoscale and Submesoscale Dynamics

1.3.1 Mesoscale Eddies and Submesoscale Currents

The ocean is an inherently turbulent fluid varying with time. Time series measurements of current and temperature conducted in the 1960-1970s discovered that the energy and spatial scales of ocean variability are highly inhomogeneous (Wunsch, 1981). The dominant component of the variability is defined using the terminology - "eddies", and the associated scales as the "mesoscale" (Robinson, 1983). Mesoscale eddies are generated by barotropic and baroclinic instabilities from large-scale currents (Olson, 1991), with spatial scales from approximately 10 to 100 km and temporal scales of weeks to months. It has been assumed in geostrophic balance, which means the pressure gradients are balanced with the Coriolis force. Advances in satellite altimetry since the 1990s allowed the global mapping of mesoscale variability (Ducet et al., 2000). The merged altimeter dataset revealed that mesoscale eddies are ubiquitous in the global ocean, showing numerous isolated cyclonic and anticyclonic features (Chelton et al., 2007). Beneath the surface signatures of mesoscale eddies visible in satellite images, mesoscale structures are indeed three-dimensional with depth scales of 500-1000 m in the ocean interior (Klein et al., 2019).

In the last two decades, an emerging body of theoretical, numerical, and observational research has highlighted a new class of ocean dynamics at the submesoscale, with smaller spatial scales (typically 0.1-10 km) and temporal scales of hours to days (McWilliams, 2016). From a dynamical view, oceanic submesoscale currents (SMCs) are between the rotation-dominated dynamics and the three-dimensional turbulence insusceptible to rotation effects. Contrary to mesoscale eddies in geostrophic balance, SMCs are referred to as "agesotrophic" motions (Thomas et al., 2008). They are preferentially generated through nonlinear interaction between mesoscale eddies and stirring of mesoscale currents (Capet et al., 2008; Ferrari and Wunsch, 2009). SMCs in the mixed layer have been found to have significant seasonality, with winter more energetic than summer, mainly regulated by mesoscale-driven frontogenesis and mixed-layer baroclinic instabilities (Callies et al., 2015; Thompson et al., 2016). SMCs embedded in the background mesoscale eddy field are characterized by ephemeral vortices, elongated fronts and filaments (Figure 1.4). These features generally occur in the surface mixed layer

and bottom boundary layers (Yu et al., 2019a; Srinivasan et al., 2017), but also exist in the ocean interior (Gula et al., 2019; Siegelman et al., 2020).

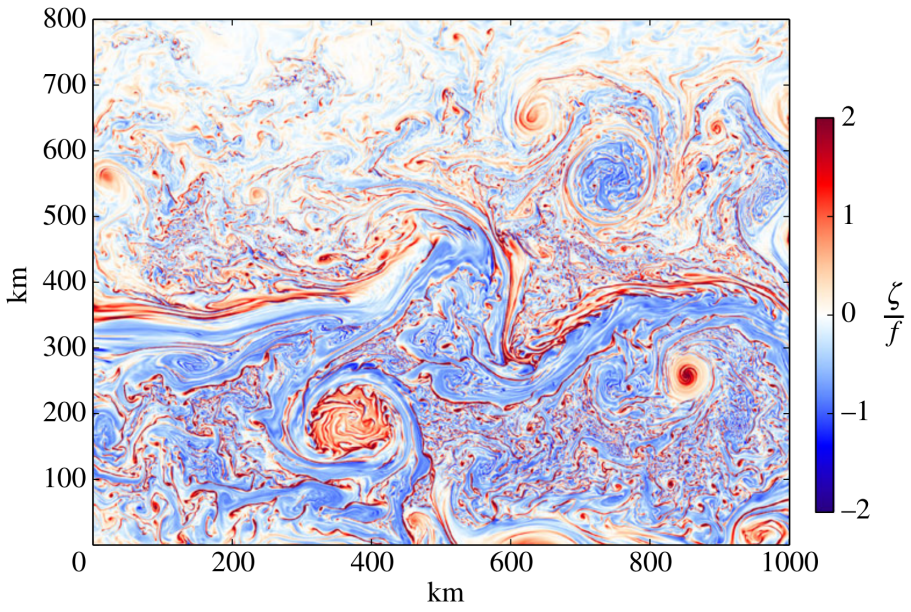

FIGURE 1.4: A snapshot of the eddy field in the wintertime Gulf Stream from a submesoscale-resolving simulation. Surface vertical vorticity ζ normalized by f shows the meandering stream and mesoscale eddies associated with a soup of submesoscale features in between. Figure from McWilliams (2016).

1.3.2 Impacts on the carbon export

1.3.2.1 On the production

Ocean dynamic processes exert influences on POC export by generating a heterogeneous distribution of primary production (PP) and hence particle production. They modulate the major temporal and spatial scales of bulk biological variability, including biomass, production, and export (Garçon et al., 2001). The network of satellite observations has highlighted the impact of mesoscale eddies on chlorophyll distribution and, thus primary production. Infrared and ocean color images show rich signatures of eddies and fronts, where the high chlorophyll concentration corresponds to the eddy structures (Figure 1.5). The underlying mechanisms to observe such a patchy pattern are predominantly the horizontal transport of chlorophyll by the stirring and trapping effects of eddies (Martin, 2003; d'Ovidio et al., 2010; Lehahn et al., 2011; Gaube et al., 2014). On the vertical, eddy pumping, eddy-wind interaction, eddy impacts on mixed-layer depth and transport due

to ageostrophic vertical velocities come into play by altering the availability of nutrients and light (McGillicuddy et al., 2007; McGillicuddy, 2016).

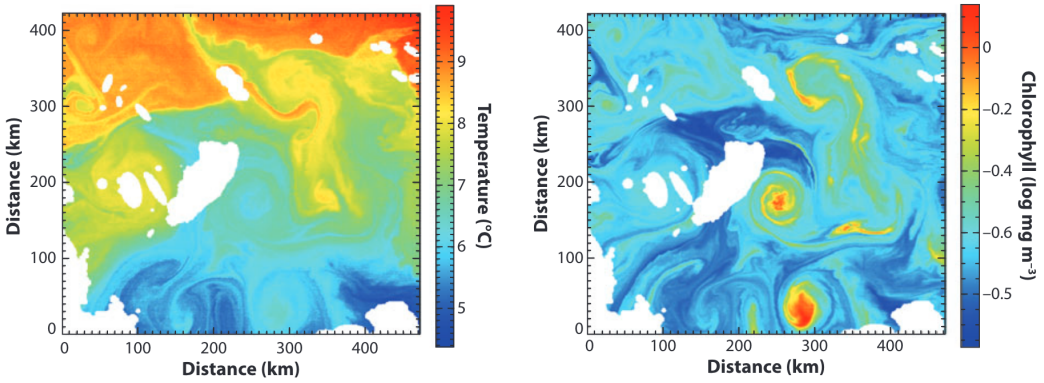

FIGURE 1.5: Sea surface temperature (left) and chlorophyll concentration (right) inferred from satellite data (From Klein and Lapeyre (2009). Image courtesy of Jordi Isern-Fontanet).

As a transition between mesoscale and microscale, submesoscale dynamics show an enormous potential of their local impacts on the fate of biogeochemical properties in space and time (Klein and Lapeyre, 2009; Lévy and Martin, 2013). High-resolution (1 km) satellite-derived sea surface chlorophyll exhibits elevated concentration at the submesoscale range (Mahadevan, 2016), and this phenomenon has been reproduced by numerical simulations showing phytoplankton blooms triggered by restratification at submesoscale fronts (Taylor and Ferrari, 2011). Furthermore, large vertical velocities generated at submesoscale frontal structures can reach a magnitude of $\mathcal{O}(10)$ to $\mathcal{O}(100)$ m d^{-1} from the surface down to hundreds of meters (Mahadevan and Tandon, 2006; Klein and Lapeyre, 2009). The vertical transport enhanced by SMCs along the periphery of eddies is likely to intensify the nutrient supply to the euphotic layer, which consequently stimulates the primary production (Mahadevan et al., 2008; Lévy et al., 2018). Elevated particle flux in the anticyclonic eddy core was suggested to be the inward transport of higher particle production at the eddy edge enhanced by the uplifted nutricline due to submesoscale upwelling (Zhou et al., 2013).

However, the decoupling due to the time lag between PP and export is generally recognized (Estapa et al., 2015; Mcgillicuddy et al., 2019). Only a limited fraction of POC produced by PP is exported from the surface ocean to mesopelagic depths, which is referred to as export efficiency (e-ratio=export/PP). Although in situ quantification of e-ratio is challenging, the e-ratio has been noted to broadly differ

in space and time (Henson et al., 2015). As such, the interest of this thesis is placed on the direct impact of the eddy field on BCP in terms of particle transport.

1.3.2.2 On the transport

A more direct way that mesoscale and submesoscale dynamics influence carbon export is by modulating particle transport. Known as oceanic counterparts of the atmospheric weather systems, mesoscale eddies account for approximately 80% of the total kinetic energy (Ferrari and Wunsch, 2009). The mesoscale eddy field incorporates coherent vortices and other structures like filaments, spirals, and squirts. These energetic features play a pivotal role in the mixing and transport of properties such as heat, salt and carbon. The eddy field shapes the horizontal transport of particles through advection and diffusion (Siegel et al., 1990, 1999). It can also structure the subsurface distribution of particles into a deep-reaching funnel of particles towards the eddy center (Waite et al., 2016). Moreover, the accumulation of floating materials is associated with specific flow structures (Figure 1.6), which provides implications for potential carbon particle transport. A numerical study by Samuelsen et al. (2012) demonstrates the physical origin of non-sinking particle accumulation at the rim of an eddy. Surface drifter trajectories combined with a numerical Lagrangian experiment reveal a preferential clustering of buoyant materials in mesoscale cyclones (Vic et al., 2022). Furthermore, strong surface convergent zones associated with submesoscale cyclonic fronts are found to concentrate materials into tight clusters within a short time (Poje et al., 2014; McGillicuddy, 2016; D'Asaro et al., 2018).

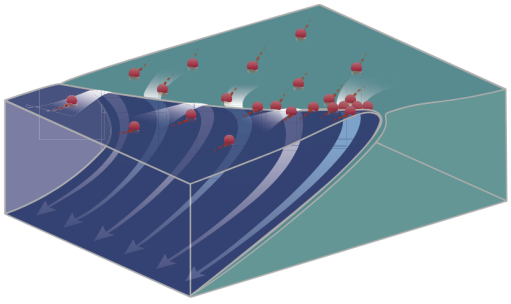

FIGURE 1.6: Floating material swept by the convergence and downwelling of surface currents accumulates at a density front. Figure from D'Asaro et al. (2018).

In addition to the redistribution of particles on the horizontal, vertical sinking affected by the eddy field is more related to the export flux. Liu et al. (2018)

show the vertical advection of gravitationally sinking particles enhanced in a high-resolution (1 km) regional model. The export rate corresponding to gravitational sinking can increase due to the reduced vertical mixing by the mixed layer restratification associated with submesoscale processes (Taylor et al., 2020). Also, intense vertical velocities (10-100 m d^{-1}) arising from mesoscale eddies and submesoscale frontal dynamics can locally subduct POC from the surface layer to the interior (Lévy et al., 2012; Resplandy et al., 2019). Mesoscale eddies and frontal regions at their periphery are often sites associated with intensified POC export (Figure 1.7). The strong straining field at the edge of eddies can facilitate particle export via secondary ageostrophic circulation induced by frontogenesis. Such an enhanced export by the eddy-driven localized and intermittent subduction episodes is called "eddy-pump" (Llort et al., 2018). Both in situ observations and coupled modelling revealed the deep intrusion of elevated POC along the perimeter of mesoscale eddies (Guidi et al., 2012; Omand et al., 2015). A recent study on particle export in the California Current Ecosystem highlights the importance of POC vertical export by subduction, especially in offshore oligotrophic regions (Stukel et al., 2018). Nevertheless, it suggests subducted particles with slow sinking speeds (3–10 m d^{-1}) were predominantly remineralized at shallower depths (<150 m), in contrast with gravitationally exported POC remineralized below 500 m.

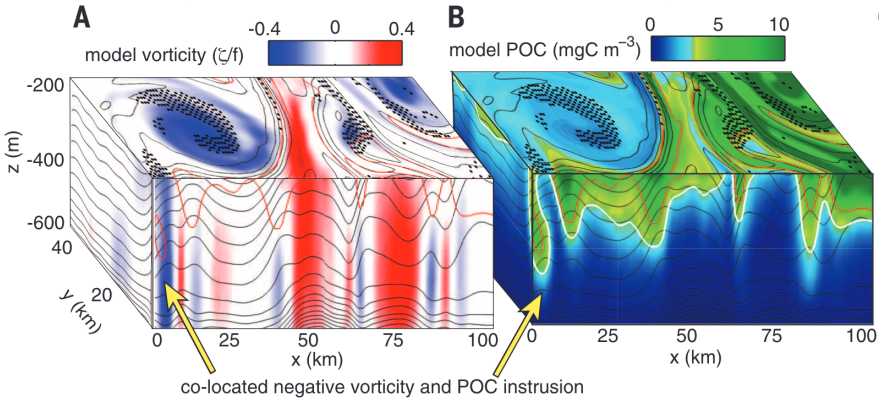

FIGURE 1.7: Subduction of POC at the periphery of an anticyclone: (A) relative vorticity ζ normalized by f and (B) POC concentration in a process-study ocean model coupled to a simple phytoplankton model. Figure from Omand et al. (2015).

1.4 Lagrangian Analysis

1.4.1 Overview

The Lagrangian analysis is a powerful approach to studying the dispersal and transport of materials by ocean currents. An ensemble of virtual particles is released in the time-evolving velocity fields produced by ocean circulation models or surface geostrophic velocities derived from satellite altimetry. The transport pathways are analyzed by statistics of particle trajectories and other properties (physical, chemical, biological) assigned to the flow of particles in postprocessing.

There are two techniques of Lagrangian integration when using an ocean model. The first is an online computation, in which trajectories are computed at each time step that the Eulerian model is updated. The second is an offline method using stored velocity fields sampled from the Eulerian model. Offline computations can be conducted in both forward (from particle starting point forward in time) and backward (from ending points backward in time) directions. The trajectory computation requires two operations: one to integrate the trajectory and one to interpolate the Eulerian velocity field to the particle position in space and time. Temporal interpolation is necessary for offline computation working with stored velocity data since the interval between consecutive velocity fields is mostly longer than the time step for the particle trajectory update. On the other hand, Lagrangian trajectory computation requires continuous velocity fields. However, ocean models are based on discretized grids with velocities only known on the corners or edges of the grid cells. Therefore, spatial interpolation is obligatory to reconstruct the continuous velocity field inside grid cells.

A review of Lagrangian ocean analysis by van Sebille et al. (2018) summarizes three advantages of Lagrangian particle experiments. A key advantage is the feasible reverse advection of particles backward in time, offered by the offline mode using stored velocity fields. Hence the origins of particles in a specific area can be identified. Also, the storage of the entire trajectory history allows empirical analysis of "connectivity" between different regions in the ocean and "conditional statistics" which refers to the analysis of particle subsets associated with certain conditions based on their properties. The last but not least advantage is the low computational cost at each time step. Therefore, the Lagrangian analysis is complementary to the analysis of tracers in the Eulerian framework with a different experimental design and a higher computational cost.

1.4.2 Applications on studying carbon export

In recent years, the Lagrangian analysis of virtual particle tracking has been applied to various study areas and issues in oceanography (van Sebille et al., 2018). Depending on the study objectives, the virtual particles mimic diverse objects such as particulate matter (Frigstad et al., 2015), larvae (Vic et al., 2018), plastics (De La Fuente et al., 2021) and surface drifters (Döös et al., 2011). The application of Lagrangian analysis on carbon export can be dated back to the 1990s. Typical usage is the backward tracking of particles to interpret downward particle flux measured by deep-ocean sediment traps. As noted earlier in this chapter, the prolonged deep-moored sediment traps are the only device to provide long-term measurements of the carbon flux to the deep ocean. The sampling of gravitational sinking particles is traditionally viewed as a 1D process (Deuser and Ross, 1980). However, particles sink not only vertically but nearly horizontally in the energetic eddy field, where they can be transported over long distances and redistributed in the water column.

The concept of a "statistical funnel" was proposed by Deuser et al. (1988) for connecting the sediment trap at depth to the sea surface. The funnel contains all likely positions during the particle sinking before they enter the trap, whose intersection with the sea surface delineates the catchment area of the sediment trap (Figure 1.8). The Lagrangian particle backtracking is an effective tool to characterize and estimate the statistical funnel. In early Lagrangian analyses, particles are horizontally advected by the random mesoscale eddy field (Siegel et al., 1990), the time-mean current overlaid with fluctuating components (Siegel and Deuser, 1997), and velocity data from observed vertical profiles in the Eulerian frame at the trap location (Waniek et al., 2000). These works demonstrate the catchment area as a function of eddy diffusion, particle sinking rate and trap depth. More importantly, they highlight that understanding the temporal and spatial characteristics of the overlying flow field is important to interpret particle flux measurements by sediment traps.

A more comprehensive study on the statistical funnel made the first attempt to use a three-dimensional velocity field for particle tracking by projecting satellite-derived geostrophic currents to depth based on the velocity profile from ADCP data (Siegel et al., 2008). They point out the ephemeral nature of sediment trap sampling, with the horizontal scales of the daily source region for a deep-moored trap at 4000 m on the order of 100 km distance from the trap location. In recent

years, Lagrangian particle analyses using 3D velocity field from circulation models reveal strong temporal variability of statistical funnels from interannual to daily scales, with seasonality indicated (Qiu et al., 2014; Frigstad et al., 2015; Wekerle et al., 2018; Ruhl et al., 2020). From a spatial perspective, particle backtracking forced by current data of modeled mesoscale eddy composites presents the vertically tilted statistical funnels and lateral transport of particles from the edge to the eddy center (Ma et al., 2021).

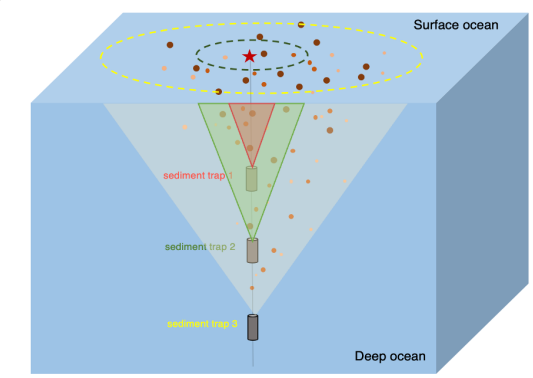

FIGURE 1.8: Conceptual diagram of the statistical funnel for an array of deep-moored sediment traps in the deep ocean. The mooring location is marked as the red star on the top. Organic carbon particles are shown as dots of different sizes at the surface ocean layer. The three cylindrical containers are sediment traps at different depths, with colored shadings representing the statistical funnels and dashed circles at the surface circumscribing the catchment area.

Lagrangian analysis has also been used to investigate the pathways of carbon export. Stukel et al. (2018) combined in situ measurements with a data-assimilative physical circulation model and a Lagrangian particle tracking model to study the role of subduction and gravitational sinking in the California Current Ecosystem. They suggest subduction is critical for carbon export out of the euphotic zone, while gravitational sinking is a prevailing pathway for export to the deep ocean. Dever et al. (2021) released particles with different sinking velocities in two process-oriented model simulations of an upper-ocean eddy field. Their findings emphasize the transition of the leading export mechanism from gravitationally-driven to advectively-driven for the slow-sinking particles in a dynamical regime with more active submesoscale dynamics. By analyzing Lagrangian trajectories of water parcels leaving the mixed layer, the subduction was found to be transient in coherent regions along the frontal region induced by submesoscale dynamics coupled with mesoscale frontogenesis (Freilich and Mahadevan, 2021).

1.5 Aims and Outline of the PhD

The BCP has attracted considerable attention over the last few years with new international programs focused on the export of organic carbon from the euphotic zone and its fate in the twilight zone (depths of 500 m or deeper). A new, detailed understanding of POC transport processes and pathways linking primary production in the surface layer to the exported organic carbon in the underlying deep ocean requires a combination of field campaigns, remote sensing and numerical modeling. This thesis is directly linked to sea cruises on the BCP, more specifically, the approaching French program APERO (Assessing marine biogenic matter Production, Export and Remineralization: from the surface to the dark Ocean) in June 2023, proposed to quantify the physical and ecological connections between surface and mesopelagic processes (https://www.aperocruise.fr/). This program is part of a large international consortium, JETZON, which is a UN Ocean Decade Programme. Moreover, this work has a potential impact on the use of upcoming advanced satellite observations of surface chlorophyll and particles with ocean color data (PACE) and (sub)mesoscale dynamics with the new generation of altimetry data (SWOT) to support estimates of particle export from space.

This PhD thesis aims at connecting the downward flux of gravitationally sinking particles sampled by deep-ocean sediment traps with the surface particle sources. This work is intended to answer three scientific questions:

(i) Where do the particles collected in the deep ocean sediment traps come from?

(ii) How do mesoscale dynamics shape the transport of particles?

(iii) Is it possible to connect particle collection in the deep ocean with signatures of particle production in the upper ocean?

The primary investigation tool is numerical modelling. This work relies on a high-resolution (2 km) simulation of the North Atlantic and a code of Lagrangian trajectories suited for sinking particles. Virtual Lagrangian particles are released in the eddy field constructed by outputs from a mesoscale-resolving circulation model. Chapter 2 describes the numerical framework in more detail. The particle seeding patch is centered on the location of the Porcupine Abyssal Plain Sustained Observatory (PAP-SO) site in the Northeast Atlantic (48°50′N 16°30′W, 4850 m water depth). The PAP site is one of the two abyssal long-term open-ocean time

series sites globally, focused on the study of connections between the surface and deep ocean.

From a bottom-up view, chapter 3 addresses the impact of mesoscale dynamics on the source area and subsurface transport of sinking particles eventually collected by deep-ocean sediment traps at a fixed location. The method is backtracking particle trajectories from sediment traps to the surface layer. This chapter presents the source locations of particles at the export depth and Lagrangian quantities of the horizontal transport. Finally, it illustrates the role of vertical motions associated with specific eddy structures.

Chapter 4 uses forward tracking of particle trajectories to link particle interceptions in the deep ocean with particle productions, where they are exported. From a top-down view, this work categorizes and characterizes particle clusters based on metrics such as horizontal displacement, trajectory length, and physical properties along particle trajectories. These clusters are further linked with specific compositions in the flow field (fronts/eddies) at the export depth.

Chapter 5 summarizes the main results of this PhD thesis and offers perspectives for future work toward more localized studies involving particle complexity and submesoscale dynamics.

Chapter 2

Data and Methods

This chapter presents the numerical framework and the Lagrangian experimental design. Here, we briefly introduce the physical model and provide information on the configuration setup, followed by a subsection about particle tracking and trajectory data post-processing. The second part of this chapter describes how we designed two different types of experiments (backward and forward) to address specific questions, including the choice of the study region and details about the particle tracking simulations.

2.1 Numerical framework

2.1.1 Physical model outputs

2.1.1.1 The CROCO model

Physical model outputs used in this thesis are from simulations using the CROCO (Coastal and Regional Ocean Community) model built upon the Regional Oceanic Modelling System (ROMS) (Shchepetkin and McWilliams, 2005). A complete description and documentation of CROCO are available on its website (https://www.croco-ocean.org/). It is a split-explicit, free-surface ocean model that solves primitive equations obtained from Navier-Stokes equations based on the Boussinesq approximation and hydrostatic vertical momentum balance. The model uses terrain-following coordinates, with a curvilinear grid of the Arakawa C type on the horizontal and σ-coordinate stretching and condensing with the bottom topography on the vertical. The advection scheme is 3^{rd} order upstream-biased advection scheme, which allows the generation of steep tracer gradients with a weak dispersion and diffusion. There is no need to impose explicit horizontal diffusion or viscosity to avoid numerical noise in the case of 3D modeling.

2.1.1.2 The POLGYR simulation

The simulation (POLGYR) covers the North Atlantic Subpolar Gyre with a horizontal grid spacing of 2 km. It is based on a coarser simulation at 6 km resolution over the entire North Atlantic (NATL) using a one-way grid nesting approach (Figure 2.1). The child grid has 1600 $\times$ 2000 grid points spanning from 72°W to 10°E in longitude and from 36°N to 70°N in latitude. The 2 km resolution is much smaller than the first Rossby deformation radius over this domain (10-30 km) (Chelton et al., 1998), such that this model is expected to be eddy-resolving and submesoscale-permitting. The 80 vertical levels of POLGYR allow a vertical resolution of 3.6 m at the surface and no more than 15 m at the bottom along the topographic slopes. The bathymetry used in this configuration is constructed from the Shuttle Radar Topography Mission (SRTM30 plus) dataset with a resolution of 30 arcseconds. The topography is smoothed to avoid aliasing due to the resolution difference between the topographic grid and the computational grid, as well as errors induced by the steep bathymetric slopes in shallow regions. For the parameterization of the vertical mixing, the POLGYR simulation adopts the Generic Length scale (GLS) scheme with the $k - \epsilon$ closure (k is the turbulent

kinetic energy, ϵ is the rate of dissipation) (Umlauf and Burchard, 2003). This choice takes advantage of the fact that in GLS the mixing coefficient is adapted to the local characteristics, which generates appropriate dissipations to limit the numerical noise in the vertical velocity field.

The NATL simulation is initialized with the initial and lateral boundary data from the Simple Ocean Data Assimilation (SODA; Carton and Giese, 2008) from January 1, 1999 to December 31, 2008. The POLGYR uses the same atmospheric forcing as the NATL (ERA interim data) and is initialized after the first two years used for the NATL spin-up (2001-2008). The studies in this thesis are limited to 2002-2008, leaving one year of spin-up time to reach a quasi-equilibrated state in POLGYR. There is no tidal forcing in the model, which greatly reduces the generation of internal waves and high-frequency variability.

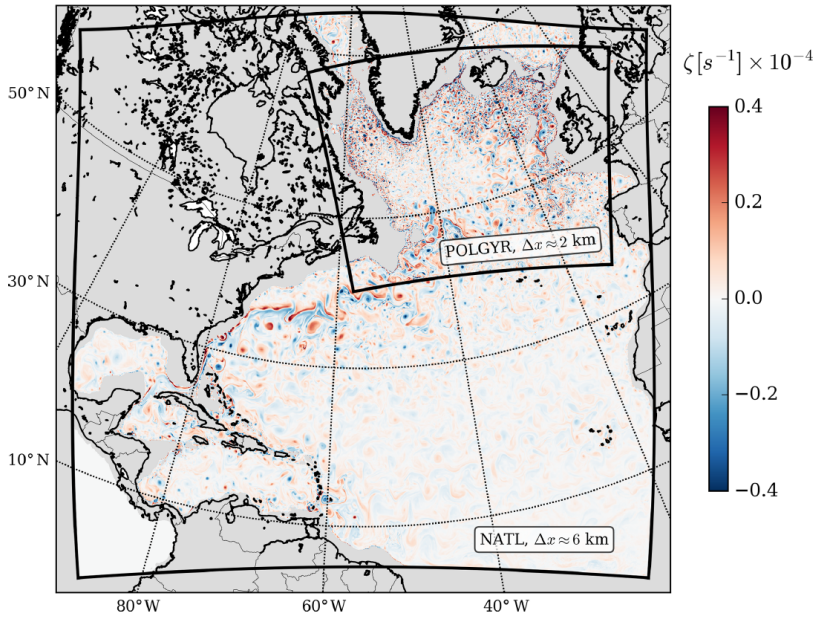

FIGURE 2.1: Snapshot of the relative vorticity at 500 m depth in the North Atlantic for the NATL and POLGYR simulations. From Le Corre et al. (2020).

The simulation has been validated in terms of the mean circulation and the mesoscale activity using observational datasets. The model well reproduces the mean circulation at the surface and 1000 m depth, compared with surface velocities derived from the GDP drifter climatology and deep currents from the Argo-based ANDRO dataset, respectively (Le Corre et al., 2020). Surface mesoscale activity is assessed by comparing simulated eddy kinetic energy (EKE) with that derived

by GDP drifters. The POLGYR simulation shows similar patterns as observations with comparable amplitudes over most of the domain. Mesoscale activity at depth is evaluated by the eddy available potential energy (EAPE), validated using Argo data. In general, the simulation successfully captures EAPE hotspots shown in observations. An average winter depth of 200 m in POLGYR is consistent with the ISAS (In Situ Analysis System) data (Gaillard et al., 2016).

Note that the simulation was run by Mathieu Le Corre. For more details about the simulation setup and validations, the reader is referred to Le Corre et al. (2020).

2.1.2 Particle tracking and postprocessing

2.1.2.1 Pyticles

The particle tracking tool we used is Pyticles (Gula and Collin, 2021). It is a Python/Fortran hybrid parallel code for offline advection of Lagrangian particles using high-resolution ocean model output. It allows particle seeding in 2D and 3D velocity fields, with or without sedimentation (i.e., particle sinking velocity). This tool has been used to seed synthetic neutrally buoyant particles in several studies of mesoscale and submesoscale dynamics (Gula et al., 2014; Vic et al., 2015; Gula et al., 2016; Klymak et al., 2016).

Pyticles initializes a particle patch in the model coordinate system (x_u, y_v, σ), where x_u and y_v are coordinates on the u-grid and v-grid, respectively. The trajectory of a particle is tracked by its position (x_p, y_p, z_p) at a given time t, where the model fields are linearly interpolated in space. Also, linear interpolation in time is applied to model outputs to obtain sufficiently frequent and temporally smooth velocity sampling for accurate particle advection. The time scheme for advection is 4^{th} order Runge-Kutta, with a time step of 2 minutes which respects the Courant-Friedrichs-Lewy condition (Courant et al., 1967).

Pyticles has a good performance in the reversibility of particle tracking. We tested it by backtracking particles sinking at 50 m d^{-1} from 1000 m to 200 m, then forward tracking them in time back to the initial time steps. The particle trajectories in the three back-forth trackings show that the starting points of the backtracking and the endpoints of the forward tracking visually overlap (Figure 2.2). We compute the difference between the end position of the forward tracking and the start position of the backward tracking. The errors are $\mathcal{O}(10^{-4})$ m for the horizontal difference and $\mathcal{O}(10^{-7})$ m for the vertical difference over a distance of $\mathcal{O}(10)$ km

(Figure 2.3). Such numerically induced errors are much smaller than the ocean data grid (2 km) and can be considered insignificant.

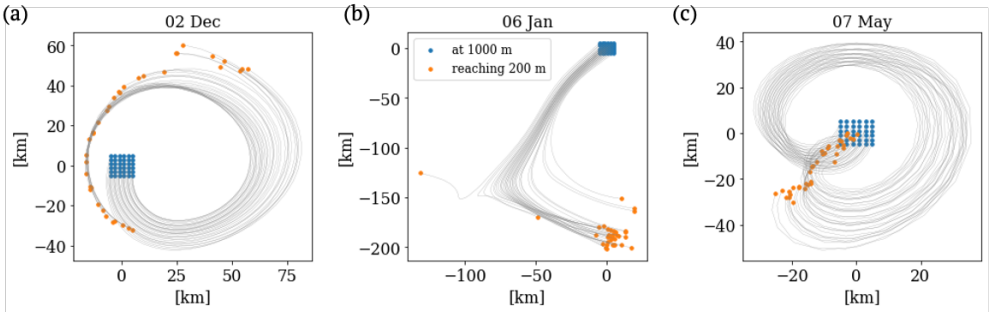

FIGURE 2.2: Particle trajectories (grey lines) marked with the start (blue dots) and end (orange dots) positions of backward tracking. The endpoints of forward tracking overlap the blue dots on the patch.

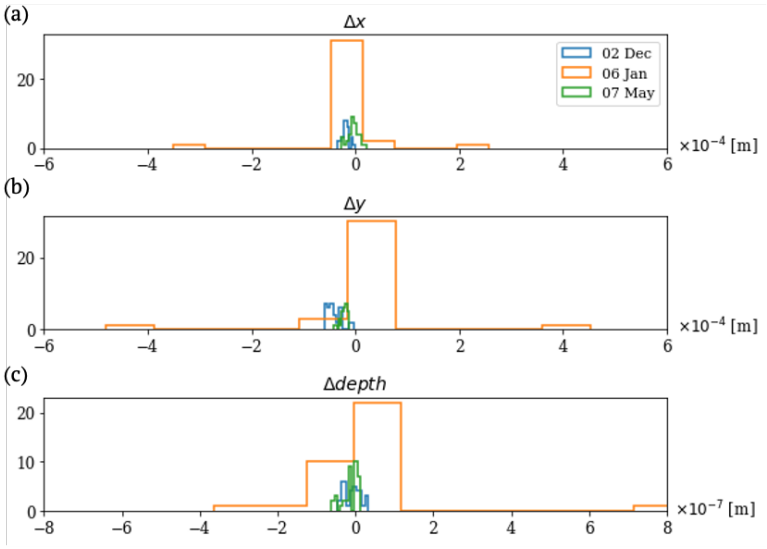

FIGURE 2.3: Histograms of particle position difference between the start points of backward simulation and end points of forward simulation: horizontal Δx and Δy, vertical $\Delta depth$.

2.1.2.2 Sensitivity tests

The eddy field is constructed using 12-hourly instantaneous outputs from the POLGYR simulation. We made some sensitivity tests to compare statistics derived from particle trajectories advected by instantaneous/averaged POLGYR outputs at different temporal frequencies. Hourly outputs were used to obtain snapshots and temporal averages at intervals of 1h, 3h, 6h, and 12h. We assess the horizontal displacement and vertical velocity of particles sinking at 20 m d^{-1} and 200 m

d^{-1}. The three basic measures of horizontal displacement vary little as the time resolution of the flow field changes (Figure 2.4).

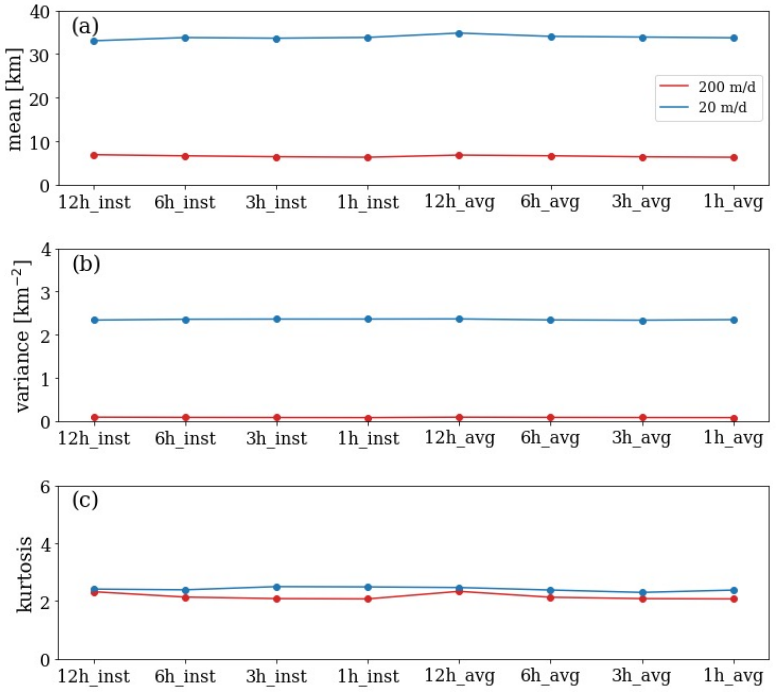

FIGURE 2.4: Horizontal dispersion in the sensitivity test runs, assessed by metrics derived from the PDF of horizontal displacements: (a) mean; (b) variance; (c) kurtosis. The x-axis is labeled by the types of outputs used for test runs: instantaneous ('inst') or average ('avg') at 12/6/3/1 hour intervals.

Also, the vertical variations in terms of vertical velocity recorded by particles and residence time anomaly show minor differences between these sensitivity experiments (Figure 2.5). Therefore, 12h instantaneous outputs are sufficient to capture particle dynamics in the eddy field of such a typical open-ocean region where mesoscale currents dominate, and sources of high-frequency variability such as submesoscale currents and internal waves are not fully resolved.

2.1.2.3 Postprocessing of the trajectory data

Particle trajectory data mainly consists of particle position, depth and velocity. In the postprocessing, horizontal displacement and trajectory length are computed using particle position. On the vertical, we are concerned about the time that particles take from the initial depth to the target depth, i.e., travel time t. We commonly use travel time anomaly Δt as an indicator of vertical variations ($\Delta t =$

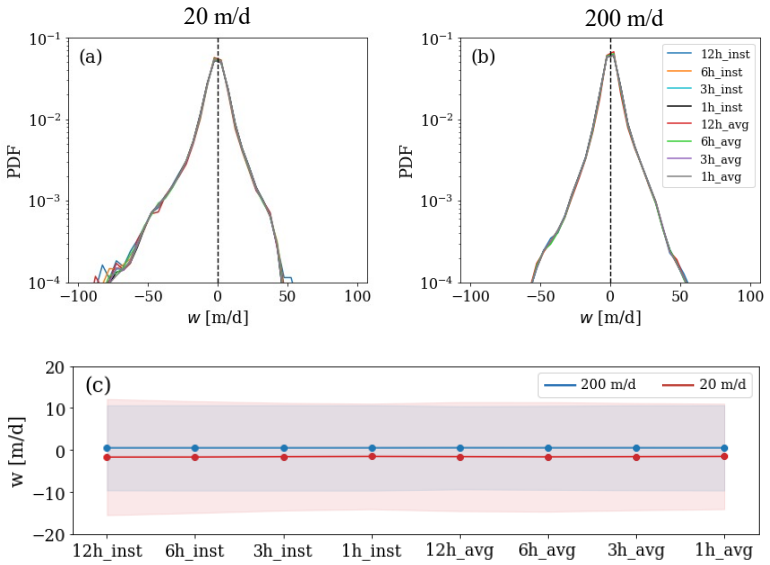

FIGURE 2.5: Vertical velocity w recorded by particles in the sensitivity test runs: (a) PDF of w for 20 m/d; (b) for 200 m/d; (c) mean w with standard deviations.

$t - t_0$, where t_0 is the standard sinking time of a particle without the influence of vertical flow).

We also derive physical parameters along particle trajectories by interpolating variables calculated in the Eulerian frame on particle positions. The diagnostics include relative vorticity ($\zeta = v_x - u_y$), strain rate ($\sigma = \sqrt{(u_x - v_y)^2 + (v_x + u_y)^2}$), divergence ($\delta = u_x + v_y$), Okubo-Weiss parameter ($OW = \sigma^2 - \zeta^2$), and vertical velocity w.

2.2 Experiment design

2.2.1 The study region

This thesis focuses on an open-ocean region encompassing the Porcupine Abyssal Plain (PAP, 48.63-48.75°N, 16.09-16.27°W) in the northeast Atlantic Ocean. The PAP is a vast, relatively flat plain with water depths ranging from 4000 to 4850 m. It lies south of the main flow of the North Atlantic Current (NAC) and is subject to the return flow of the NAC from the west and northwest. The weak mean flow around 0.05 m s^{-1} (Le Cann, 2005) and moderate kinetic energy make this area representative of a substantial fraction of the global ocean. Nevertheless, satellite and in situ observations reveal an intermittent stream of cyclonic and anticyclonic mesoscale eddies propagates across the area, sometimes extending thousands of meters into the water column (Painter et al., 2010; Damerell et al., 2016). Such a pattern is also shown in our simulation (Figure 2.6).

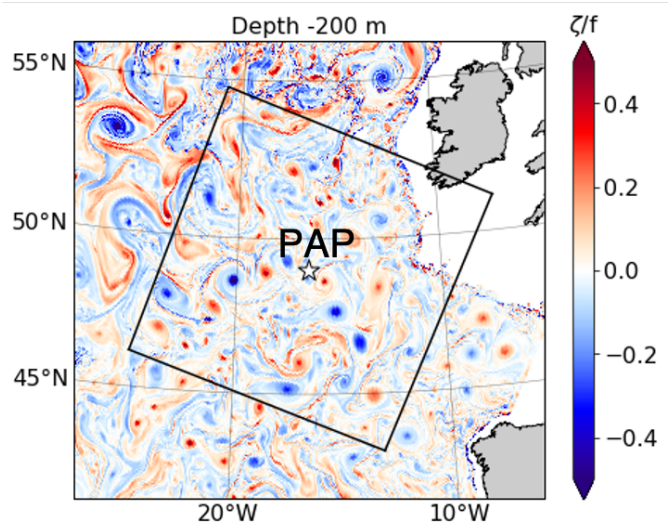

FIGURE 2.6: Snapshot of relative vorticity ζ at 200 m depth, normalized by Coriolis parameter f. The white star in the center marks the location of a long-term sustained observatory site at PAP. The black box outlines the study region in this thesis.

The North Atlantic Ocean is one of the key regions where oceanic carbon uptake and organic carbon storage in the interior are at climate-relevant timescales (>100 years; Baker et al., 2022). Our study region centered on the sustained observatory (PAP-SO) at 49°N 16.5°W with a depth of 4800 m. The PAP site hosts a multi-disciplinary observing system coordinated by the National Oceanography Centre

Southampton for over 20 years to monitor and investigate the response of open-ocean and deep-sea ecosystems to climatic change (https://projects.noc.ac.uk/pap/). A prolonged series of downward particle flux observations in the deep ocean reveal apparent seasonal and interannual variability driven by variations of upper-ocean physical processes in this region (Lampitt et al., 2010). Previous studies in the past two decades suggest that mesoscale activity exerts important influences on the biogeochemical properties in this region (Martin and Richards, 2001; Hartman et al., 2010; Painter et al., 2010). Recent observational studies from the OSMOSIS (Ocean Surface Mixing, Ocean Submesoscale Interaction Study) project have reported the role of submesoscale processes in determining open-ocean dynamics (Thompson et al., 2016; Buckingham et al., 2016; Yu et al., 2019a), and in physically driving the carbon export (Erickson and Thompson, 2018). The upper-ocean dynamics are known to highly depend on the variability of mixed layer depth (MLD) (de Boyer Montégut et al., 2004; Boccaletti et al., 2007). Although the model underestimates the winter MLD, there is a significant annual cycle in both simulated and observed MLD, typically varying from 30-40 m in summer to 200-300 m in winter (Figure 2.7).

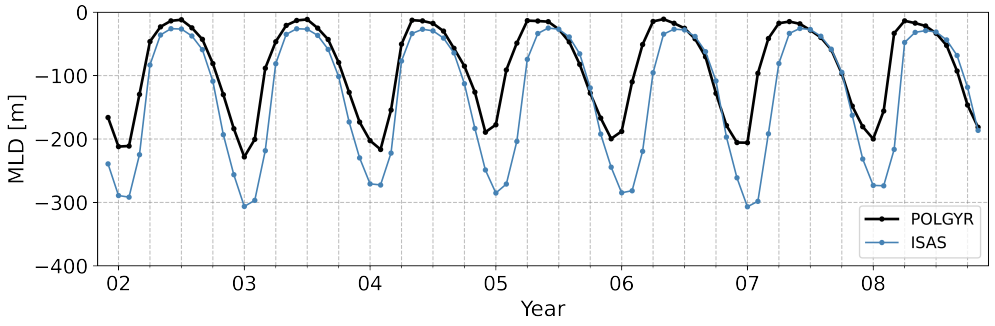

FIGURE 2.7: Monthly averaged mixed layer depth (MLD) from the model (POLGYR) and observations (ISAS). Both MLDs are calculated using the temperature threshold ($\Delta T = 0.2$ °C).

2.2.2 Lagrangian experiments

We performed backward and forward particle tracking experiments, referred to as "backward simulation" and "forward simulation" in the rest of the thesis. Figure 2.8 shows different designs for the two types of simulations. The backward simulation is designed to characterize statistical funnels of deep-ocean sediment trap sampling and to relate their spatiotemporal variability to underlying mesoscale dynamics between the trap locations and the upper boundary of the twilight zone.

In the backward simulation, we seed particles at the two locations of virtual sediment traps in the deep ocean and track particles using the time-reversed velocity field until they reach the export depth in the upper ocean (here fixed at 200 m). The goal of the forward simulation is to explore the impact of ocean dynamics on the mesoscale distribution of particles at depth. For the forward simulation, a large number of particles are released from the export depth and tracked down to the target zone at two depths in the deep ocean.

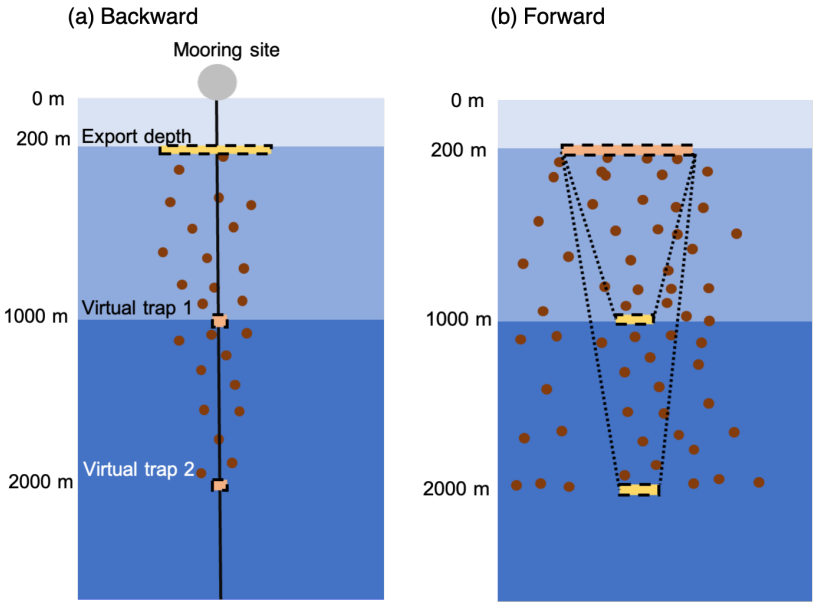

FIGURE 2.8: Schematic diagrams of the two types of Lagrangian experiments: (a) Backward simulation; (b) Forward simulation.

Details of the experiments, including some basic settings, are in the following parts.

2.2.2.1 Basic settings

Start and end depth In this numerical work, the export depth is the end depth where the source locations of particles are determined in the backward simulation. It is also the initial depth where particles are seeded in the forward simulation. As mentioned in Chapter 1, the scope of this work lies in the dark ocean, with a major focus on the twilight zone (200-1000 m). Although the mixed layer is essential as the interface between the ocean surface and deep layers, the travel time of particles with sinking velocities of 50 m d^{-1} in the ML is about 4 days if we assume that the particles are "created" just at the surface (which is not the case). Considering the mixed layer involves making assumptions about the depth of particle formation,

we focus here on the fate of the particles after they are formed and exported below the productive surface layer. Hence the export depth here is the upper bound of the twilight zone, 200 m, which is also a typical depth of the deep winter mixed layer in this region (Yu et al., 2019a; Coatanoan, 2021).

The other depth setting is the depth at which the seeding patch is placed in the backward simulation, and the deep-ocean target zone is located in the forward simulation. We use 1000 m and 2000 m, representing the bottom of the twilight zone and the standard depth of the deep-ocean sediment traps, respectively.

Sinking velocity The intrinsic sinking velocity of particles is also a key parameter in our experiments. In the real ocean, it can vary by a few orders of magnitude, from <1 m d^{-1} to more than 1000 m d^{-1} (Siegel et al., 1990). Detrital POC can be loosely classified into three pools based on the sinking velocity: fast sinking (> 20 m d^{-1}), slow sinking (< 20 m d^{-1}), and suspended (Baker et al., 2017). Our study focuses on particles penetrating deep into the twilight zone and finally reaching the deep ocean. Estimates of bulk particle sinking speeds at the PAP site provide a minimum value of 30 ± 6 m d^{-1} at 50 m (Villa-Alfageme et al., 2014). Observations suggest slow-sinking particles are an unlikely source of POC in the abyss at the PAP site, and estimate the fast sinking velocity of particles to be around 180 ± 22 m d^{-1} (Riley et al., 2012). Based on the above concerns, we adopt 20 m d^{-1} as the lower limit and 200 m d^{-1} as the largest value of sinking velocity in our experiments.

Seeding patch The Pyticles model is based upon Arakawa C-grid, where particles can be seeded anywhere within the domain. We sample initial conditions with the same resolution as the CROCO ocean model, i.e., seeding on the model grid points. First, it is coherent with CROCO passive tracers. Secondly, uniform seeding seems a good approach to avoid oversampling some coherent structures, by using a number of particles at an affordable computational cost to run our experiment over 7 years. We have verified that subgrid seeding does not qualitatively and statistically change particle distributions. As a result, a uniform initial seeding on grid points is a reasonable compromise to obtain statistics independent from initial conditions on a period long enough to investigate seasonality. The Lagrangian tool allows particles to be released either once or in a continuous injection at a given frequency. For both types of simulations, we mainly use the continuous mode to broadly sample the spatiotemporal variability of the subsurface transport

of particles. The physical model outputs we used have a time step of 12 h, and we kept the same frequency for particle seeding.

2.2.2.2 Backward simulations

In the backward simulation, particles are assigned four constant sinking speeds (20, 50, 100, 200 m d^{-1}). These values mostly fall in the observed range of particle sinking rates at the PAP site and are common choices in literature (Siegel and Deuser, 1997; Waniek et al., 2000; Siegel et al., 2008; Frigstad et al., 2015; Liu et al., 2018). We use different lengths of integrations for particles being continuously injected with various sinking velocities from different trap depths. This strategy ensures the consistency of the sample size of various particle ensembles.

The seeding patch is a 10×10 km slice corresponding to a 5×5 grid-cell square centered on the location of the PAP site in the model. However, the real sediment traps have a surface area of 1 m^2. To test the sensitivity to the seeding patch size, we conducted backtracking experiments using a one-point grid-size patch for two example periods. First, particles were released over one grid point every 1h based on the interpolation of the model flow field. A second test uses subgrid seeding with 400 m as horizontal spacing over a 2×2 km area every 12h. The two initializations over the smaller patch have comparable amounts of particles to that of the 10 × 10 km patch. Figure 2.9 indicates that the source location does not visually differ much when using the small seeding patches. Quantitatively, the mean displacement (r_{mean}) and the radial distance containing 95% of the source regions ($R_{95\%}$) have minor differences as well.

The goal of the backward simulation is to understand how much the circulation, in particular the presence of eddies, affects particle collection by sediment traps at the PAP site. We do not aim to realistically reproduce observations. Using either a 10 × 10 km patch or a 2 × 2 km patch does not differ much from a real sediment trap (~ 1 m^2). Given the similarity of the source regions obtained by the different methods, we prefer to use the larger patch for physical reasons. At the grid scale, the dynamics are not fully resolved. It takes about 5 to 8 grid points for a numerical model to competently represent a physical phenomenon. Also, using the larger patch implicitly accounts for dispersion due to mixing, since there is no added diffusivity in the Lagrangian model. Finally, the continuous injection of 36 particles every 12 h from the seeding patch gives a total of about 2100 particles over a month, which is a considerable amount of particles for our analysis.

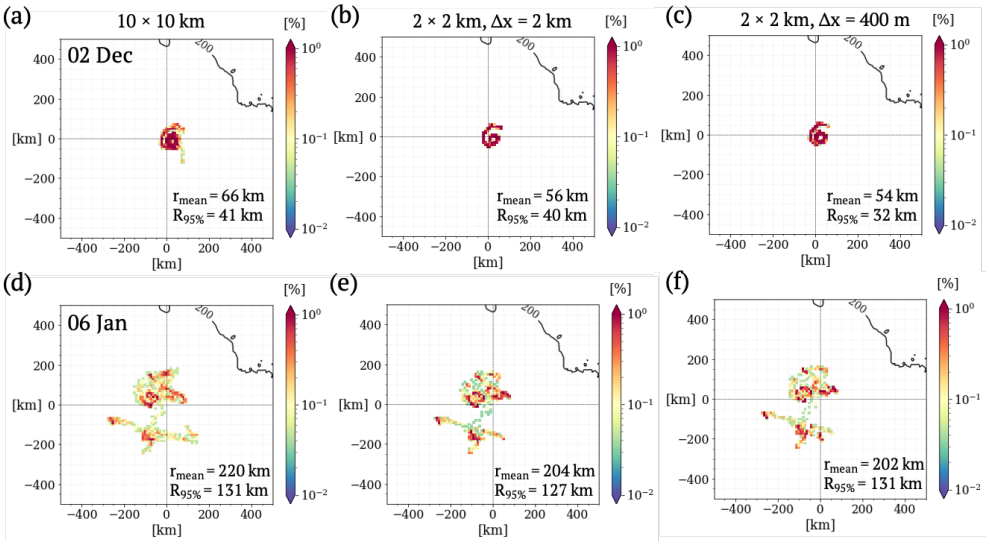

FIGURE 2.9: Source location of particles (w_{sed} = 50 m d^{-1}) backtracked during two example periods, (a-c) 2002 December and (d-f) 2006 January. The left column is for the original 10 × 10 km patch. The middle column is for the 2 × 2 km patch with particles seeded on grid points every 1 h, and the right column is for the 2 × 2 km patch with particles seeded every 12h at 400 m intervals.

2.2.2.3 Forward simulations

Forward simulations use the same physical model outputs as backward simulations spanning 7 years (2002-2008). By continuously seeding particles on a large initial patch at the export depth, the size of the particle data set for analysis is enormous compared to the limited number of particles seeded from a tiny patch in backward simulations. We can statistically characterize the eddy field to specify the contribution of different circulation features to particle exports. Also, forward simulations allow an analysis of particle distribution in the deep ocean, which is different from the spot-like particle location in backward simulations.

We specify a 200 × 200 km target zone centered on the PAP site at 1000 m and 2000 m depth. The sinking velocity in forward simulations is 50 m d^{-1}, for a good compromise between the realistic range of sinking velocity and the ability to reflect the influence of flow dynamics. The size of the initial patch at 200 m is estimated by performing a series of backward simulations using the seeding patch described in the part about backward simulation. We released particles from nine 10×10 km patches centered on points at the border and center of the target zone at 2000 m (Figure 2.10a). Based on the distribution of particle trajectory endpoints at

200 m integrated over the 7-year backward simulations from 9 points, the seeding patch has 1200 km on the side with a center lying 100 km to the south and 100 km to the west of the PAP site (Figure 2.10b). This patch size guarantees the full coverage of the deep target zone by particles sinking from the export depth. Again, we use the continuous injection every 12 h to obtain sufficient and stable particle collection at depth. The total number of particles released in the forward simulations is 2,530,944,780, and the amount of particles reaching the target zone at each time step is approximately 9000 after a setup period.

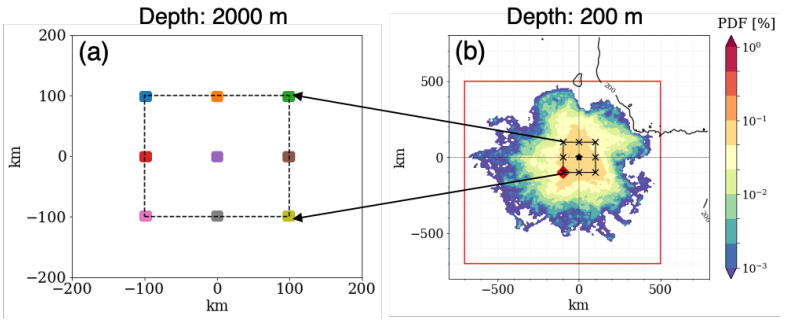

FIGURE 2.10: (a) The location of 9 seeding patches on the 200 × 200 km target zone at 2000 m, the purple patch in the middle is centered on the PAP site. (b) Distribution of particles from the 9 patches backtracked to 200 m during the 7 years. The black markers show the centers of 9 backward seeding patches, while the red diamond marks the center of the forward seeding patch southwest of the PAP site. The red square confines the initial seeding patch used for forward simulations.

The comparison of backward simulation and forward simulation is summarized in the table below.

Simulation	Start depth	End depth	Sinking velocity	patch size	particle amount
Backward	1000, 2000	200	20, 50, 100, 200	10×10 km	∼180,000
Forward	200	1000, 2000	50	1200×1200 km	∼52,000,000

TABLE 2.1: Summary of the key settings for the backward and forward simulation. The last column "particle amount" refers to the approximate total number of particles in a group (one start/end depth + one sinking velocity) used for postprocessing during the entire period (2002-2008).

Chapter 3

Effects of mesoscale dynamics on particles exported to the deep ocean

This chapter consists of a short introduction to the work based on backward simulations of particles and the published paper with supplementary materials.

3.1 Introduction

We introduced the concept of the "statistical funnel" of sediment traps in Chapter 1. In this chapter, we assess the long-term (multiple years) and monthly statistical funnels for deep-ocean sediment traps at the PAP site location. As we are interested in the fate of the particles once they have been exported below the surface layer, we do not consider the mixed layer dynamics. We focus on the role of the mesoscale (and the larger submesoscale) below the mixed layer, whose role is not that well understood. The base of the twilight zone, 1000 m, is the criterion depth for the long-term sequestration (over 100 yr) of carbon in the ocean interior (Passow and Carlson, 2012). The main purpose of this work is to assess how dynamics in the twilight zone (200-1000 m) affect particles exported to the deep ocean.

Using the backward particle tracking experiments described in Chapter 2, we find that deep-ocean sediment traps sample across hundreds of kilometers over the long term. However, on monthly time scales, when eddies generally associated with a deep signature occur near the PAP station, particle collection can be more locally confined in an area of several tens of kilometers. We applied a set of dispersion metrics to characterize particle trajectories and link them with mesoscale dynamical features. The inhomogeneous horizontal distribution of particles is related to various lateral dispersion regimes throughout the water column in conjunction with the substantial influence of vertical flows. Overall, the vertical flow acts to enhance particle export. Particles in anticyclonic eddies tend to sink faster than expected from gravitational sinking only, which is contrary to those in cyclonic eddies.

The results emphasize the role of mesoscale dynamics in affecting particle collection in a typical open ocean region. With the presence of a coherent eddy at the sampling site, the particle flux sampled by deep-moored sediment traps can be more correlated to the production of organic carbon in the upper ocean. The finding also has implications for the sampling strategy during cruises and the interpretation of particle export measurements in regional surveys.

3.2 Article published in Journal of Geophysical Research

Wang, L., Gula, J., Collin, J., & Mémery, L. (2022). Effects of Mesoscale Dynamics on the Path of Fast-Sinking Particles to the Deep Ocean: A Modeling Study. *Journal Of Geophysical Research-oceans*, 127(7).

JGR Oceans

RESEARCH ARTICLE
10.1029/2022JC018799

Effects of Mesoscale Dynamics on the Path of Fast-Sinking Particles to the Deep Ocean: A Modeling Study

Lu Wang[1], Jonathan Gula[2,3], Jérémy Collin[1], and Laurent Mémery[1]

[1]University Brest, CNRS, IRD, Ifremer, Laboratoire des Sciences de l'Environnement Marin (LEMAR), IUEM, Plouzané, France, [2]University Brest, CNRS, IRD, Ifremer, Laboratoire d'Océanographie Physique et Spatiale (LOPS), IUEM, Plouzané, France, [3]Institut Universitaire de France (IUF), Paris, France

Abstract The gravitational sinking of organic particles is a vital component of the biological carbon pump. This sinking process is strongly modulated by the spatiotemporally varying eddy field, complicating the interpretation of particle flux measured by deep-moored sediment traps. By backtracking particles to 200 m depth based on the outputs of a realistic eddy-resolving simulation, we characterize the origins of particles collected at a long-term observatory site in the Northeast Atlantic and focus on the impact of mesoscale dynamics on particle transport. Our results show that mesoscale dynamics between 200 and 1,000 m control the statistical funnel. Over the long term, the horizontal sampling scales of traps are estimated as hundreds of kilometers, with containment radius ranging from 90 to 490 km, depending on sinking velocities. Particle travel time suggests that overall vertical flow acts to facilitate the export, with estimated deviations up to 1 ± 2 days for particles sinking at 50 m d^{-1} to 1,000 m. Statistical analyses of horizontal displacements reveal that mesoscale eddies at the site confine particle sources in a more local area. On average, particles in anticyclonic eddies sink faster to depth than expected from purely gravitational sinking, contrary to their counterparts in cyclonic eddies. The results highlight the critical role of mesoscale dynamics in determining particle transport in a typical open ocean region with moderate eddy kinetic energy. This study provides implications for the sampling design of particle flux measurements during cruises and the interpretation of deep-ocean mooring observations.

Plain Language Summary As plants in the ocean, phytoplankton organisms transform the atmospheric CO_2 into organic carbon that forms particles of various sizes sinking to the deep ocean due to gravity. The falling particles can be collected by containers called sediment traps. However, particles may originate far from the surface ocean directly above the trap as ocean currents horizontally transport particles. Also, the time taken by particles to sink to the deep ocean varies due to vertical motions of seawater. To study the impact of ocean currents on sinking particles, we use an ocean model and virtual particles. We release particles at a fixed location, representing a sediment trap, and track particle trajectories back in time to identify their source regions. Our results show that the size of this source region is mainly determined by currents between 200 and 1,000 m. On average, particles tend to sink faster than expected from purely gravitational sinking. Large whirlpools of water above the trap lead to a local source region, which suggests that the particle flux can be better correlated to the surface production of organic carbon in this case. The finding has implications for the sampling strategy and the interpretation of particle export measurements in regional surveys.

Key Points:

- The statistical funnel of deep-ocean sediment traps is mainly determined by mesoscale dynamics in the twilight zone
- On average the vertical flow enhances particle sinking, but with more variance in spring than in other seasons
- Coherent eddies reduce the particle dispersion within a local area, with vertical acceleration (deceleration) by anticyclones (cyclones)

Supporting Information:

Supporting Information may be found in the online version of this article.

Correspondence to:

L. Wang,
Lu.Wang@univ-brest.fr

Citation:

Wang, L., Gula, J., Collin, J., & Mémery, L. (2022). Effects of mesoscale dynamics on the path of fast-sinking particles to the deep ocean: A modeling study. *Journal of Geophysical Research: Oceans*, *127*, e2022JC018799. https://doi.org/10.1029/2022JC018799

Received 11 MAY 2022
Accepted 8 JUL 2022

1. Introduction

A vital process of oceanic carbon cycling is the biological carbon pump (BCP) which sequesters atmospheric CO_2 by exporting photosynthetically produced organic carbon from the surface layer to the deep ocean (Falkowski et al., 1998). The BCP is mainly regulated by the sinking particulate organic carbon (POC) produced in the euphotic zone (Henson et al., 2015; Riley et al., 2012; Sanders et al., 2014; Turner, 2015). Long-term observations of the downward particle flux are available from moored sediment traps over recent decades (Buesseler et al., 2007; Lampitt & Antia, 1997; Lampitt et al., 2010; Le Moigne et al., 2013). Traditionally, POC export through gravitational sinking is evaluated from a quasi-one-dimensional (1D) viewpoint, which couples particle interception by sediment traps with particle production in the surface ocean directly above the trap (Armstrong et al., 2001; Asper et al., 1992; Deuser & Ross, 1980). However, particles are also affected by horizontal advection during their vertical sinking (Burd et al., 2010; Deuser et al., 1990; Siegel et al., 1990). Consequently,

Journal of Geophysical Research: Oceans 10.1029/2022JC018799

impacts of hydrodynamics on sinking particles challenge the link of particle collection at depth with surface signatures (Dever et al., 2021), and hence promote the extrapolation of POC export in a spatiotemporally varying circulation field.

The concept of the statistical funnel has been raised to construct a dynamical source region enclosing the likely origins of particles settling to time-series sediment traps (Siegel & Deuser, 1997). The statistical funnel is often characterized by analyzing Lagrangian particles backtracked from the trap location to the surface ocean. Waniek et al. (2000) identified origins of particles from separated, distant regions by daily mean observed current profiles at a quasi-time-series station in the northeast Atlantic. Siegel et al. (2008) constructed statistical funnels for a deep-moored trap in the Pacific ocean using a combination of satellite-derived geostrophic velocities and shipboard ADCP profiles. They estimated horizontal scales larger than 300 km for a trap at 4,000 m collecting particles sinking at 50 m d^{-1}. Such a sampling scale is confirmed by Qiu et al. (2014) with the use of a time-dependent 3D velocity field of a circulation model. Furthermore, studies of Liu et al. (2018) and Wekerle et al. (2018) both showed that the statistical funnels vary with the trap location and seasons, and highlighted the presence of eddies in determining the particle sources. These studies have shown that the statistical funnel of moored sediment traps depends on trap depth, particle sinking velocity, collection time, and regional advective processes.

Ocean mesoscale dynamics exert influences on POC export by generating a heterogeneous distribution of primary production that produce sinking particles (Lévy et al., 2018; Mahadevan, 2016), and by directly modulating particle transport (Boyd et al., 2019). Mechanisms of the physical-biological interactions at mesoscale have been demonstrated in terms of eddy stirring, trapping, and pumping (McGillicuddy, 2016; McWilliams, 2008; Olson, 1991). Eddies can horizontally advect and diffuse particles (Deuser et al., 1988; Siegel et al., 1990, 2008), and add an additional advective vertical flux of POC in the eddy-related frontal region (Stukel et al., 2017). Also, eddies can structure the subsurface distribution of particles, leading to a deep-reaching funnel of particles toward the eddy center (Waite et al., 2016). Furthermore, mesoscale dynamics may have an impact on the POC export at smaller scales (Klein & Lapeyre, 2009). In the horizontal, strong surface convergent zones associated with submesoscale cyclonic fronts are found to concentrate materials into tight clusters within a short time (D'Asaro et al., 2018; McGillicuddy, 2016; Poje et al., 2014), leading to a preferred accumulation of buoyant material into mesoscale cyclones (Vic et al., 2022). While in the vertical, large vertical velocities generated at submesoscale frontal structures extend from the surface down to hundreds of meters (Klein & Lapeyre, 2009; Lévy et al., 2012; Mahadevan & Tandon, 2006). The magnitude of vertical velocity in different dynamical regimes ranges from $\mathcal{O}(10)$ to $\mathcal{O}(100)$ m d^{-1} (Pietri et al., 2021), comparable to the majority of particle sinking velocities accounting for carbon fluxes at depth (50–200 m d^{-1}) (Turner, 2002). The control of vertical flows on the travel time of particles is important for sediment trap measurements, especially during the period of rapid spring blooms (Asper et al., 1992). In this manner, the local vertical velocity field may considerably affect particle export from the upper ocean. Observations have shown elevated POC flux generated by the stretching features in the frontal region between mesoscale eddies (Guidi et al., 2012). The elevations were mostly detected within the mixed layer, though the mixed layer base did not appear to obstruct the particle export. Intensified mesoscale eddies may also produce deep-reaching submesoscale fronts that penetrate well below the mixed layer (Siegelman et al., 2020; Yu et al., 2019). Such findings suggest enormous potential impacts of mesoscale eddies and their associated submesoscale dynamics on the fate of particle export to the deep ocean.

As an interface between the well-studied epipelagic layer (sunlight zone) and the dark deep ocean, the mesopelagic layer (also known as the "twilight zone") spanning from 200 to 1,000 m is a crucial element in the rapid removal of carbon further down to the deep ocean. However, the understanding of the role of the twilight zone in carbon transport remains to be improved from physical, biogeochemical, and ecological perspectives (Martin et al., 2020). Since 2019, the Joint Exploration of the Twilight Zone Ocean Network (JETZON) has been set up to provide a new scientific understanding of the twilight zone. It coordinates a variety of international projects, one of which is the French project Assessing marine biogenic matter Production, Export and Remineralization from the surface to the dark Ocean (APERO), built on an upcoming intensive field program at the Porcupine Abyssal Plain sustained observatory (PAP-SO) in the open-ocean region of Northeast Atlantic. The PAP site allows simultaneous studies of both upper ocean and abyssal depths, where deep-sea POC flux has been measured over decades using a long-term sediment trap mooring. Scheduled for June 2023 when the export peaks, the cruise of APERO follows the US EXPORTS cruise to the same location during the bloom/post-bloom period in May 2021 (Siegel et al., 2016).

Journal of Geophysical Research: Oceans 10.1029/2022JC018799

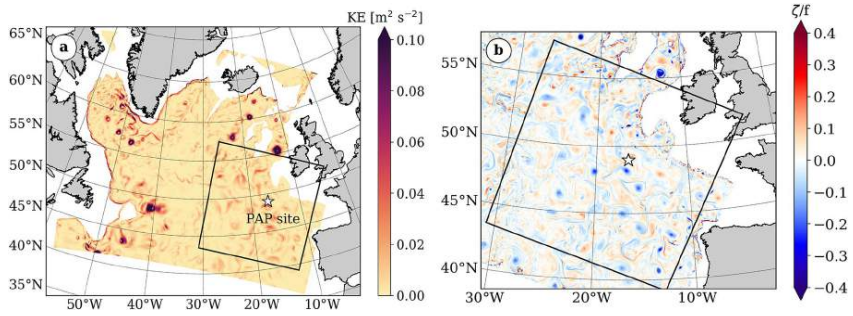

Figure 1. Snapshots of (a) kinetic energy at 1,000 m for the whole POLGYR domain and (b) a zoomed relative vorticity field at 1,000 m. The study region is in the black box centered on the Porcupine Abyssal Plain site (white star).

Motivated by the sustained observations and upcoming APERO cruise in the PAP region, this study aims to identify the source region of particles collected by deep-ocean sediment traps, and investigate how mesoscale patterns shape the statistical funnel of particles. We use outputs from an eddy-resolving regional ocean model to backtrack particles from the PAP site. The findings will have implications for the design of the Process Study Stations to be deployed during the APERO cruise. This work assesses for the first time the impact of small/medium-scale dynamics on the dispersion of sinking particles in the mesopelagic layer (200–1,000 m), once exported below the surface mixed layer. The paper is organized as follows. Section 2 provides information on the ocean circulation simulations and Lagrangian experiment design. Section 3 presents results of particle backtracking, including statistical funnels, horizontal and vertical dispersion, and the role of specific flow structures on particle transport. Finally, we offer conclusions and discussion on the findings in Section 4.

2. Experiment Setup

The particle backtracking experiments are designed to reconstruct a large number of particle trajectories from sediment trap locations to the upper boundary of the twilight zone. Our goals are to characterize statistical funnels of deep-ocean sediment trap sampling, and to relate their spatio-temporal variability to underlying mesoscale dynamics.

2.1. Numerical Model Outputs

Instantaneous outputs at 12 hourly intervals from a realistic eddy-resolving model are used to compute particle trajectories. The simulation was performed using Coastal and Regional Ocean COmmunity model (CROCO) built upon ROMS (Shchepetkin & McWilliams, 2005) which solves the hydrostatic primitive equations for the momentum and state variables. The configuration (POLGYR) has 2,000 × 1,600 grid points covering the North Atlantic Subpolar Gyre. The horizontal grid spacing is 2 km, much smaller than the first Rossby deformation radius over this domain (10–20 km) (Chelton et al., 1998). There are 80 vertical sigma levels, with a variable resolution following the topography (about 5 m at the surface and 40 m at the bottom, up to 100 m for the maximum vertical spacing in the intermediate layer). After a two-year spin-up time, the simulation is run from 2001 to 2009, and we use the seven years between 2002 and 2008. The use of 12-hourly wind forcing and the absence of tides largely reduces the generation of internal waves and high-frequency variability.

Le Corre et al. (2020) provide a detailed description of the simulation, and validation through comparisons of the mean circulation as well as mesoscale activity, with observations from drifters and Argo floats. In this study, we focus on the southeastern portion of the whole domain, with a size of 1,600 × 1,600 km centered on the PAP site (49°N, 16.5°W). The study region is characterized by moderate kinetic energy compared to the western and northern parts of the subpolar gyre (Figure 1a). The mean flow in this region is around 0.05 m s^{-1} (Le Cann, 2005); such a weak advection enables particles initially seeded at the PAP site to stay within this subdomain for several

Journal of Geophysical Research: Oceans 10.1029/2022JC018799

months. The circulation in this region is dominated by mesoscale eddy activity. A stream of cyclonic and anticyclonic eddies intermittently crosses the PAP site (Figure 1b), feeding the site with an eastward meandering North Atlantic Current branch, and flows from the European shelf (Hartman et al., 2010).

2.2. Lagrangian Particle Tracking

We use a Python/Fortran hybrid parallelized code, named "Pyticles" (Gula & Collin, 2021), to track offline particles backward to their source locations. Particles evolve in the native Arakawa C-grid and terrain-following vertical coordinates of the ocean model. The model fields are linearly interpolated at particle positions in space and time. The numerical time scheme for advection is Runge-Kutta 4, with a time step of 2 min, which ensures that the Courant-Friedrichs-Lewy condition is satisfied. The Lagrangian model has a good performance in the reversibility of particle tracking, with errors of $\mathcal{O}(10^{-4})$ m for horizontal displacement and $\mathcal{O}(10^{-7})$ m for vertical displacement, over a travel distance of $\mathcal{O}(10)$ km. Sensitivity tests verified that increasing the frequency of CROCO snapshots used for experiments from 12 to 1 hr, or using averages instead of snapshots, has a negligible impact on the statistical results of particle dispersion (Figure S1 in Supporting Information S1) and vertical velocities (Figure S2 in Supporting Information S1). Therefore, 12 hr instantaneous outputs are sufficient to capture particle dynamics for such a typical open-ocean region where mesoscale currents dominate, and sources of high-frequency variability such as submesoscale currents and internal waves are not fully resolved.

A series of experiments is performed to backtrack particles monthly collected over the seven years (2002–2008). The seeding depths are chosen at 1,000 and 2,000 m, representing the bottom of the twilight zone and a standard depth of the deep-ocean sediment traps, respectively. This study focuses on the impact of mesoscale dynamics in the mesopelagic layer once particles are exported below the mixed layer. Hence the base of the epipelagic layer, 200 m, is chosen as the end depth where source locations of particles are determined. This depth is also a typical depth of the deep winter mixed layer in this region (Coatanoan, 2021; Yu et al., 2019). Four constant sinking speeds (200, 100, 50, and 20 m d^{-1}) are assigned to particles. They are mostly endorsed by observations at the PAP site giving the range of particle sinking rates from 30 m d^{-1} (Villa-Alfageme et al., 2014) to 180 m d^{-1} (Riley et al., 2012). Particles are initialized every 12 hr within a 10 × 10 km seeding patch centered on the PAP site, corresponding to 6 × 6 grid points with one particle located at each grid point. The choice of the patch size implicitly considers the dispersion due to subgrid-scale mixing, as there is no parameterized diffusivity in the Lagrangian model. We have tested that the exact location of the particles inside the patch does not impact our results by performing additional experiments with particles randomly seeded in the patch (not shown). In each experiment, particles are injected continuously every 12 hr over one month and are tracked until they reach 200 m. The total number of particles for a monthly analysis is 2,160 (i.e., 36 × 60).

To investigate how the dynamical regimes of horizontal advection change with depth, we also deploy depth-keeping particles on the horizontal plane at different depths. The seeding patch and the timing of particle release in these 2D experiments are the same as in the 3D ones.

3. Results

3.1. Statistical Funnel of Deep-Ocean Sediment Traps

3.1.1. Overview of the Source Regions

The distribution of particle source regions at 200 m shows a synoptic picture of the sampling area resulting from the integrated horizontal advection over time and space (Figure 2). Mesoscale eddies transport particles from distant regions to the PAP site, which forms a diffuse cloud of particle sources at the export depth. Such an effect has been indicated in Vic et al. (2018) by comparing the dispersion pattern driven by mesoscale currents to that by the mean flow. The sensitivity experiments here indicate that the catchment area of a moored sediment trap increases with the trap depth (top panel vs. bottom panel) and decreases with particle sinking velocity (e.g., from (a) to (d) on the top panel). Qualitatively, changes in the sampling area with sinking velocity are more significant than changes due to the trap depth. The area with particle density exceeding 10^{-2}% for 2,000 m trap remains almost the same as for the 1,000 m trap, whereas the radius of this area reduces by hundreds of kilometers when particle sinking velocity increases from 20 to 200 m d^{-1}. It suggests that the dynamics between 1,000 and 2,000 m does not effectively alter the statistical funnel as much as that in the twilight zone (200–1,000 m).

Journal of Geophysical Research: Oceans 10.1029/2022JC018799

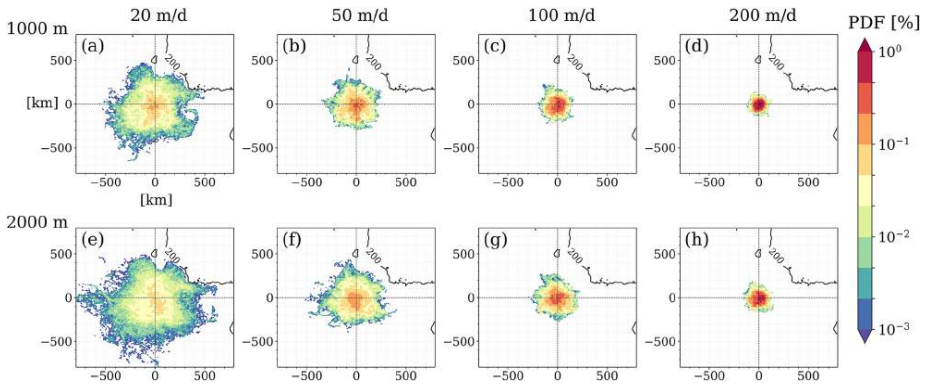

Figure 2. Source region at 200 m for particles collected by the moored sediment traps over the seven years (2002–2008), with different sinking velocities from two trap depths (a–d, 1,000 m; e–h, 2,000 m). Particle positions are binned into a 10 km × 10 km grid. The color indicates the percentage, that is, the number of particles in each bin divided by the total amount of particles. The black contour is the 200 m isobath.

The source regions are further quantified using a set of basic metrics (Table 1). Mean displacements (r_{mean}) range from 47 to 190 km for the collection at 1,000 m, with only a modest increase of <50 km for the collection at 2,000 m. The collection scale of deep-moored sediment traps is as large as 100 km, even for fast-sinking particles. Containment radii ($R_{95\%}$), defined as the radial distance covering 95% of a source region, are 90 and 118 km for particles sinking velocity of 200 m/d. The $R_{95\%}$ dramatically increases as the sinking velocity decreases, with the largest value of 490 km for particles sinking at 20 m d^{-1} to the trap at 2,000 m. Our estimates of the mean displacement and containment radii are much larger than the estimates obtained by Siegel et al. (2008) due to the higher-resolution velocity field and the larger subsurface EKE in our study region. The percentage of area with probability densities larger than 10^{-2}% confirms that changes of source area with sinking velocity are more significant than with trap depths.

Figure 3 shows the vertical structure of statistical funnels by integrating trajectories of particles from 2000 m projected on the zonal section. The funnels of particles sinking at 100 m d^{-1} and 200 m d^{-1} have limited widths with less variability over depth. By contrast, the collection of the two slower sinking classes is primarily controlled by the dynamics changing with depth, especially the twilight zone, as indicated by the widened bounds. The broadening of funnels between 200 and 1,000 m coincides with vertical profiles of eddy kinetic energy (EKE) and root-mean-square vertical velocity w_{rms} (Figures 3e and 3f). The former indicates horizontal transport, while the latter influences the shape of statistical funnels by affecting the sinking time of particles. The magnitude of EKE and w_{rms} are comparable to the OSMOSIS mooring observations (Yu et al., 2019). EKE shows a rapid decay from over 100 cm^2 s^{-2} in the upper ocean, down to 20 cm^2 s^{-2} at 1,000 m, and remains at such low level from here. The vertical velocity w_{rms} is intensified up to 40 m d^{-1} at 200 m during winter months when submesoscale motions are active, and at around 20 m d^{-1} for autumn and summer when mesoscale activity dominates. The slight linear increase of w_{rms} with depth below 1,000 m corresponds to a bottom intensification of vertical flows due to interactions with topography. As such, the influence of vertical flows is considerable for the 20 and 50 m d^{-1} particle groups. Based on the two profiles, the water column below the epipelagic layer can be divided into three layers with different regimes: Energetic layer (200–500 m) with high EKE and large w_{rms}, Active layer (500–1,000 m) with

Table 1
Quantitative Information for Particle Source Regions

Depth [m]	w_{sed} [m d^{-1}]	r_{mean} [km]	$R_{95\%}$ [km]	$S_{PDF>10^{-2}\%}$ [%]
1,000	20	190	394	41.6
1,000	50	116	230	62.5
1,000	100	76	146	72.8
1,000	200	47	90	80.7
2,000	20	236	490	31.4
2,000	50	141	280	52.6
2,000	100	96	194	66.1
2,000	200	64	118	76.8

Note. The left two columns list trap depths and particle sinking velocities. The right three columns are mean displacement (r_{mean}), the radial distance containing 95% of the source region ($R_{95\%}$), and the percentage of source area with PDF larger than 10^{-2}%, respectively.

Journal of Geophysical Research: Oceans 10.1029/2022JC018799

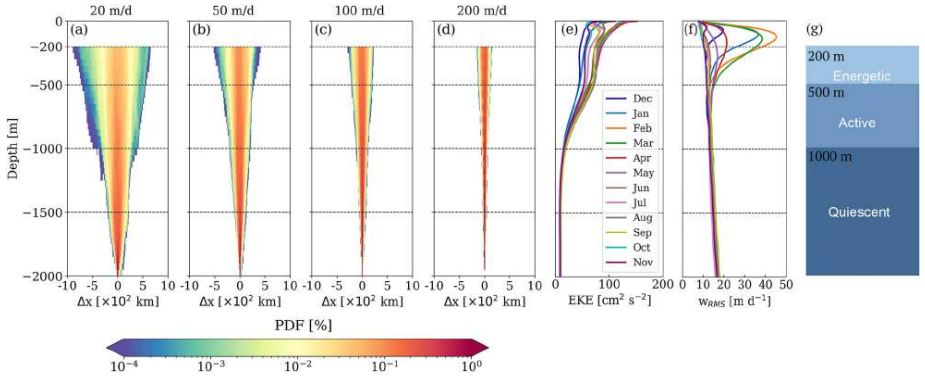

Figure 3. (a–d) Seven-year integrated particle trajectories backtracked from 2000 m, projected on the zonal section with a bin size of 10 km × 50 m. The color indicates the percentage, that is, the number of particles in each bin divided by the total amount of particles (e and f) Vertical profiles of monthly climatology eddy kinetic energy and root-mean-square vertical velocity w_{rms} averaged over 200 × 200 km domain. (g) A conceptual diagram of the three-layer structure of the water column based on the change of dynamics.

still relatively high but decaying EKE and small w_{rms}, Quiescent layer (>1,000 m) with weak and relatively steady flows (Figure 3g).

3.1.2. Statistics of the Source Regions

A source region of particles is taken as a particle cloud for statistical analysis. We adopt the general notions in LaCasce (2008) to quantify the variability of particle source regions. Three moments (mean, variance, and kurtosis) are derived from the probability density function (PDF) of the horizontal displacements for monthly backtracking of particles.

The mean describes the movement of the center of mass

$$M = \sqrt{M_x{}^2 + M_y{}^2} \tag{1}$$

with

$$M_x = \frac{1}{N}\sum_{i=1}^{N}\left[x_i - x_{i_0}\right], \tag{2}$$

$$M_y = \frac{1}{N}\sum_{i=1}^{N}\left[y_i - y_{i_0}\right], \tag{3}$$

where (x_i, y_i) gives the horizontal position of particle i when it reaches 200 m depth, and $\left(x_{i_0}, y_{i_0}\right)$ is its initial position.

The horizontal displacement relative to the center of mass for a single particle is given by

$$r_i = \sqrt{\left[x_i - x_{i_0} - M_x\right]^2 + \left[y_i - y_{i_0} - M_y\right]^2}. \tag{4}$$

The variance measures how particles spread out, namely, the size of the particle cloud (also referred to as "cloud dispersion")

Journal of Geophysical Research: Oceans 10.1029/2022JC018799

$$D = \frac{1}{N-1}\sum_{i=1}^{N}\left(\left[x_i - x_{i_0} - M_x\right]^2 + \left[y_i - y_{i_0} - M_y\right]^2\right) = \frac{1}{N-1}\sum_{i=1}^{N} r_i{}^2. \quad (5)$$

The kurtosis is used to reflect the spatial distribution of particles

$$ku \equiv \frac{\sum_i r_i{}^4}{\left[\sum_i r_i{}^2\right]^2}. \quad (6)$$

A kurtosis close to 3 corresponds to a PDF following a nearly Gaussian distribution, which is the case for randomly moving particles. In contrast, particles advected by turbulent flows tend to distribute in tight clusters, characterized by a kurtosis higher than 3.

We choose particles sinking at 50 m d^{-1} backtracked from 1,000 m as an example for the following analyses. This choice is a good compromise between the realistic range of sinking velocity and the ability to reflect the influence of flow dynamics in the twilight zone. The 20 m d^{-1} sinking group is shown in the time series as well to indicate how slow-sinking particles are affected.

The center of mass mostly moves around the PAP site within a diameter of 100 km for particles sinking at 50 m d^{-1} and 200 km for the sinking group 20 m d^{-1} (Figure 4a), as shown by the source areas in Figure 2. The two sinking groups show similar variability in the monthly statistical funnel: local kurtosis peaks appear to arise with low mean and variance. Since the end of 2002, valleys of variance often occur with small means and large kurtosis, corresponding to a local source region with a center of mass adjacent to the PAP site. Kurtosis peaks larger than 3 indicate extended tails in the PDF of horizontal displacement, which means the distribution of particles is highly heterogeneous (Figure 4c).

The presence of mesoscale eddies is most likely responsible for shaping particle distributions. Three indicators depict local mesoscale activity within a 100 × 100 km area centered on the PAP site (Figures 4d–4f). Sea level anomaly (SLA) reveals eddy features at the surface, relative vorticity $\zeta = v_x - u_y$ and Okubo-Weiss parameter $OW = \sigma^2 - \zeta^2$ where the strain magnitude $\sigma = \sqrt{(u_x - v_y)^2 + (v_x + u_y)^2}$, indicate signatures of mesoscale eddies at 500 m. We highlight eight periods based on their dispersion metrics showing local peaks of kurtosis with low mean and variance, associated with distinct signals of mesoscale eddies (half anticyclones and half cyclones, marked by the blue/red vertical lines in Figure 4). A reference period, January 2006, is chosen to compare with the former periods. Note that the reference period is characterized by a higher variance, much lower kurtosis, and no signature of local mesoscale dynamics.

3.2. Horizontal Advection

3.2.1. Horizontal Dispersion in the 3D Field

Source distributions of particles collected at 1,000 m during two representative eddy-dominated periods and the reference period are shown in the top panel of Figure 5. Particle sources were highly concentrated around the PAP site during December 2002 and May 2007, in response to the local presence of mesoscale eddies (Figures 5d and 5f). In contrast, no particular hot-spot of particle source locations is seen embracing the PAP site in January 2006 when the vorticity does not dominate (Figure 5e). This situation is representative of conditions without a single-dominant eddy structure.

The measures in Figure 4 derived from the PDF of horizontal displacements have described the shape of statistical funnels as a result of particle dispersion. We adopt notions in Poje et al. (2010) to further describe the temporal evolution of horizontal dispersion by computing single-particle dispersion and pair dispersion (Figures 5g and 5h). The former, also termed absolute dispersion, describes the spreading of particles. Denoting the trajectory of a particle by $\mathbf{x}(\mathbf{a}, t)$ where the label $\mathbf{a} = \mathbf{x}(\mathbf{a}, t_0)$, the horizontal absolute dispersion $A_h{}^2$ is defined as the mean-squared horizontal displacement

Journal of Geophysical Research: Oceans 10.1029/2022JC018799

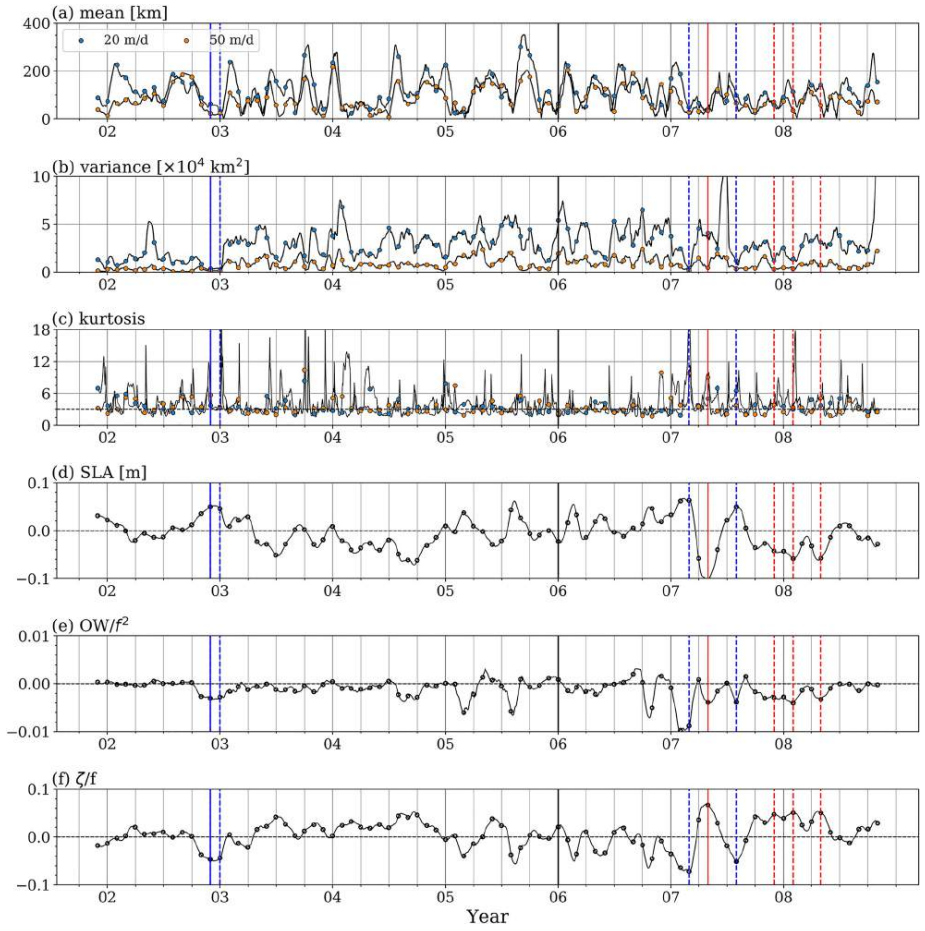

Figure 4. Time series of dispersion metrics derived from the probability density function (PDF) of particle horizontal displacements, for particles backtracked from 1,000 m sinking at 50 and 20 m d^{-1}: (a) mean; (b) variance; (c) kurtosis. (d–f) Monthly averaged sea level anomaly (SLA), Okubo-Weiss parameter normalized by f^2 and relative vorticity normalized by f in a 100 × 100 km square centered on Porcupine Abyssal Plain site. The vertical lines mark the typical months selected for further analysis: blue for the anticyclonic eddy dominated period, red for the cyclonic eddy dominated period, and black for the reference period (non-vorticity-dominated case). Solid lines highlight the main examples used in detailed analyses in Section 3.2, while the dashed lines mark alternative cases to firm the results presented in Section 3.4. The *x*-axes are labeled with "year" at the beginning of each year.

$$A_h^2(t) = < (\mathbf{x_h}(\mathbf{a}, t) - \mathbf{a_h})^2 > \quad (7)$$

where < > denotes the ensemble average. The horizontal relative dispersion D_h^2 measures particle pair dispersion that depicts the stirring process. That is, the mean-squared horizontal separation of particle pairs initially defined at the beginning of particle release. The relative separation of a particle pair ($\mathbf{a_1}$, $\mathbf{a_2}$) is computed as

Journal of Geophysical Research: Oceans 10.1029/2022JC018799

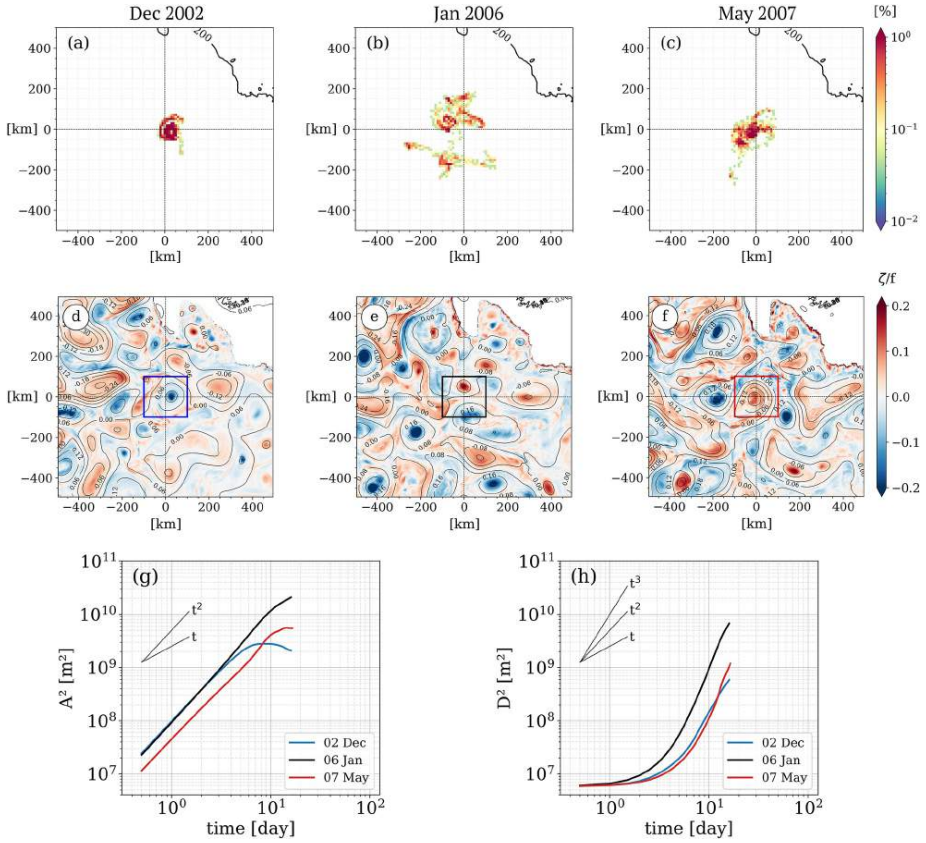

Figure 5. (a–c) Probability density of particles sinking at 50 m d^{-1} to the 1,000 m trap during three example periods. (d–f) Monthly averages of relative vorticity at 500 m with contours of sea level anomaly. (g–h) The group averaged absolute and relative dispersion. The "time" on the *x*-axis represents days after particles are released, that is, particle "age".

$$\mathbf{D}(t, \mathbf{D_0}) = \mathbf{D_0} + (\mathbf{x}(\mathbf{a_1}, t) - \mathbf{x}(\mathbf{a_2}, t)) \tag{8}$$

with the initial distance between the two particles in a pair $\mathbf{D_0} = \mathbf{a_1} - \mathbf{a_2}$. Here we consider the horizontal separation only:

$$D_h^2(t) = < \mathbf{D_h}(t) \cdot \mathbf{D_h}(t) > \tag{9}$$

The horizontal absolute dispersion ${A_h}^2$ first follows a ballistic regime ${A_h}^2(t) \propto t^2$ at small time scales of several days. The non-locality indicates the dominance of mesoscale dynamics in absolute dispersion. At intermediate time scales, an anomalous dispersion regime occurs with ${A_h}^2(t) \propto t^{\alpha}$ where α varies between 1 and 2. A diffusive regime ${A_h}^2(t) \propto t$ characterized by a slope close to 1 is expected after a long time when the absolute dispersion linearly grows in time. However, the large spatio-temporal inhomogeneities in mesoscale ocean flow

Journal of Geophysical Research: Oceans 10.1029/2022JC018799

often prevent the presence of such a regime. The slopes for December 2002 and May 2007 ultimately fall below 1 as most particles stay trapped within an eddy and cannot spread further.

Relative dispersion depicts smaller-scale motions affecting relative diffusivity. It shows less difference in slopes. The horizontal relative dispersion D_h^2 first shows an exponential growth within approximately 5 days, typically occurring at spatial scales smaller than the deformation radius (10–20 km). In the next stage, D_h^2 follows a regime $D^2(t) \propto t^\beta$ with $2 < \beta < 3$ related to motions at local scales. The evolution of absolute and relative dispersion suggests reduced particle spread when a strong eddy persists around the PAP site.

3.2.2. Dynamical Regimes of Horizontal Dispersion

Horizontal dispersion in the 3D field is also affected by vertical dispersion. Particles of the same age can vertically separate by a few hundred meters when backtracked into the upper ocean. Particles may thus experience different dynamical regimes over a range of depths and may also be affected by a vertical shear (Berti & Lapeyre, 2021). Results of 2D experiments illustrate different dynamical regimes from 200 down to 4,000 m. The visual appearance of particle trajectories suggests the dominance of mesoscale activity in transporting and trapping particles (Figures 6a–6c). Comparisons between trajectories at different depths identify that the transition depths for dynamical regimes are 500 and 1,000 m, consistent with the three-layer structure of the water column in Figure 3. In the energetic regime of horizontal advection above 500 m, particles from 200 km away or further can also reach the site in the reference case (January 2006). At the base of the twilight zone (1,000 m), the regime switches from the upper ocean with active eddies to the quiescent deep ocean. The clusters of dispersion curve for the upper ocean, middle, and deeper depths verify the regimes categorized by 2D trajectories. At intermediate stage (about 5 days), the power-law regime $D^2(t) \propto t^\beta$ with $2 < \beta < 3$ is only seen at depths above 1,000 m. It underlines the existence of small-scale motions in the upper two layers. Similar to 3D experiments, the flattening dispersion curves starting from about 5 days after the release for December 2002 and May 2007 illustrate lower dispersion of particles in the twilight zone, mostly confined within the 200 × 200 km box.

3.3. Vertical Advection

To evaluate the impact of vertical advection, we examine the time taken by particles to sink from the export depth to the trap depth, termed as "travel time." The influence of vertical flow on particle sinking can be reflected by the travel time anomaly Δt, which is the difference between the travel time t and the standard sinking time t_0 without the presence of ocean vertical flows. The amplitude of the monthly mean Δt for particles backtracked from 1,000 m can reach up to 7% (~1 day) of the expected travel time for 50 m d^{-1} particles and 12% (~5 days) for 20 m d^{-1} (Figures 7a and 7b). For individual particles, the maximal amplitude can reach up to 5 days for 50 m d^{-1} particles and 20 days for 20 m d^{-1}. Such time lags are significant for POC measurements during bloom/post-bloom periods when the production rapidly varies over days. On average, the negative $\Delta t/t_0$ in most of the experiments indicates that particles take less time to reach the trap due to the acceleration by downward ocean vertical velocity. There is no distinct seasonality found in mean Δt. However, the variance $V(\Delta t)$ commonly peaks in spring, in agreement with large vertical velocities between 200 and 400 m during this period (Figures 3e and 3f). The standard deviation reaches up to 2 days for 50 m d^{-1} particles and 6 days for 20 m d^{-1}. In Figure 7c, the distribution of seasonal and full-period Δt for particles sinking at 50 m d^{-1} shows a broader PDF in spring, in line with the seasonal variability of $V(\Delta t)$. The PDF of travel time t for the full period also displays slight asymmetry toward shorter time, and the asymmetry is more distinct for smaller sinking velocities and deeper trap depth (Figures 7d and 7e). Liu et al. (2018) found that the vertical advection in the upper 200 m largely intensifies particle export with sinking speeds from 20 to 100 m d^{-1}. Our results additionally show that the vertical advection below 200 m also enhances the export of particles.

3.4. Linking the Particle Export With Specific Features

Following the work of Balwada et al. (2021), we use the joint probability distribution function (JPDF) of vorticity and strain to decompose the flow field into regions with different dynamical features. The term "vorticity" refers to the vertical component of vorticity normalized by the Coriolis frequency ζ/f, where $\zeta = v_x - u_y$. The "strain" is the strain magnitude normalized by the Coriolis frequency σ/f, where $\sigma = \sqrt{(u_x - v_y)^2 + (v_x + u_y)^2}$. The JPDF

Journal of Geophysical Research: Oceans 10.1029/2022JC018799

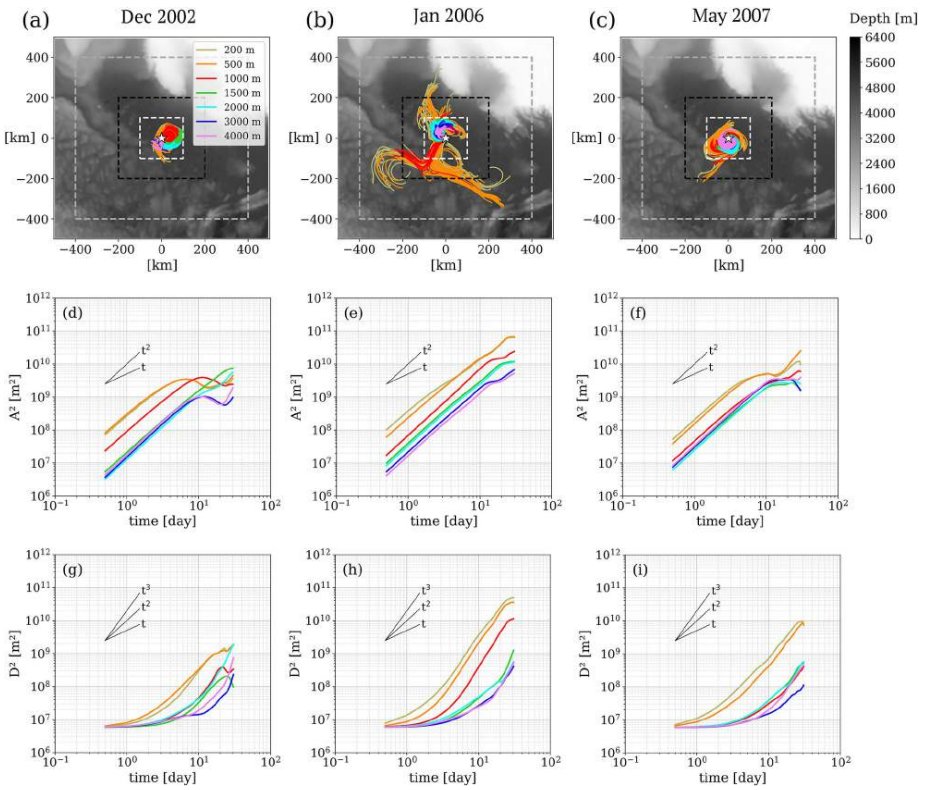

Figure 6. Trajectories and dispersion of particles in 2D simulations during the three example periods. (a–c) Trajectories of 200 particles randomly selected from 2,160 particles backtracked at each depth in a month. The white star in the center represents the Porcupine Abyssal Plain site. The small white square (200 × 200 km) highlights the region with particles concentrated at all depths. The medium black square (400 × 400 km) covers most particle trajectories backtracked below 1,000 m. The large gray square (800 × 800 km) contains all particle trajectories. The middle and bottom rows are (d–f) absolute dispersion and (g–i) relative dispersion as a function of release time.

identifies three regions in the flow field separated by the lines of $\sigma = |\zeta|$: anticyclonic vorticity dominated (AVD) region where $\zeta < 0$ and $\sigma < |\zeta|$; cyclonic vorticity dominated (CVD) region where $\zeta > 0$ and $\sigma < |\zeta|$; and strain dominated (SD) region where $\sigma > |\zeta|$. Figure 8 shows the JPDF of full-period Lagrangian data and Eulerian field for the two layers of the twilight zone (200–500 and 500–1,000 m). The Lagrangian JPDF on the top row of Figure 8 displays no distinct skewness. Hence, particles do not show a specific preference in sampling different flow structures over the long term.

Vertical velocity patterns are qualitatively similar between the Eulerian and Lagrangian diagnostics. At all depths, the AVD region is featured with downwelling, whereas the CVD region is dominated by upwelling, in accord with the picture of the vertical velocity below the mixed layer in Balwada et al. (2021). In the SD region, vertical velocity patterns change with depth. Below 500 m, vertical velocities are negative close to the line $\sigma = \zeta$, corresponding to the cyclonic side of fronts, and positive on the anticyclonic side (Figure 8h). Such a pattern

Journal of Geophysical Research: Oceans 10.1029/2022JC018799

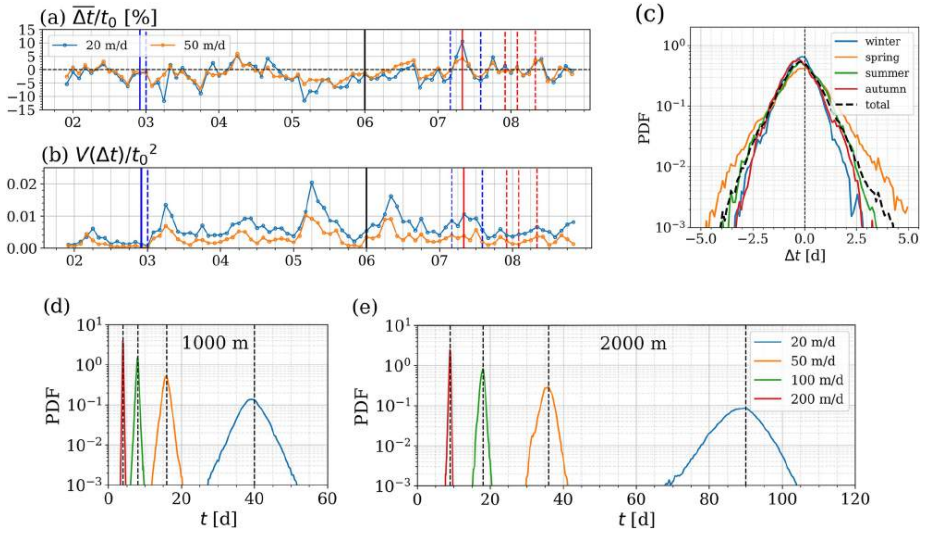

Figure 7. Metrics of vertical dispersion for particles backtracked from 1,000 m sinking at 50 and 20 m d^{-1}: (a) The percentage of mean travel time anomaly $\left(\overline{\Delta t}\right)$ to the standard travel time t_0; (b) Variance of Δt normalized by $t_0{}^2$. The colored vertical lines are the same as those in Figure 4, which marks months with local coherent anticyclonic eddy (in blue), cyclonic eddy (in red), and a reference case without coherent structure at the site (in black). (c) Probability density function (PDF) of the travel time anomaly Δt for particles sinking at 50 md^{-1} backtracked from 1,000 m depth, over full-period (7 years) and different seasons. (d and e) The PDF of travel time t over the 7-year full period for four sinking velocities and two trap depths.

is expected from frontal dynamics, and again in accord with results shown in Balwada et al. (2021) below the mixed-layer. However, between 200 and 500 m, only upwelling is visible in the SD region on both sides, apparently contradicting classical expectations.

An important difference in our computation is that the vorticity and strain are computed at the same depth as the vertical velocity, which is different from the vorticity-strain space defined at the surface only in Balwada et al. (2021). Comparisons between the w patterns depending on the depth chosen to compute vorticity and strain are shown in Figure S3 in Supporting Information S1. If the vorticity and strain are computed at the surface, we recover the expected signs for vertical velocity: downwelling on the cyclonic side and upwelling on the other side at all depths (100 m, 200 m, 500 m). However, when the vorticity and strain are computed at the corresponding depth of vertical velocity, the patterns are reversed at 200 and 500 m. This can be attributed to the presence of numerous frontal structures with an inversion of sign for relative vorticity in the vertical, while the sign of vertical velocity remains vertically homogeneous (Figure S4 in Supporting Information S1). This is a robust feature in our simulation for all times and locations, and it will be addressed further in future research.

Patterns of particles and their associated vertical velocities are shown more specifically for cases corresponding to the presence of anticyclonic or cyclonic eddies in Figure 9. On the top row, the composite distribution of particles on the vorticity-strain space for months with coherent anticyclonic eddies shows a high density of particles along the $\sigma = -\zeta$ line, with a preference in the SD region (Figure 9a). These particles are likely located in the filamentary vorticity streaks along with the swirl, which highlights the footprints of particles on the periphery of the eddy. Vertical velocities recorded by particles in Figure 9b also show upward velocities despite the dominance of downward velocities, consistent with the full-period pattern in Figures 8b and 8d. From the PDF of travel time anomaly Δt, we find that the upward velocities are mostly associated with March 2007, which has a longer tail toward positive Δt and slight skewness. It differs from the other 3 months in winter and summer with apparently

Journal of Geophysical Research: Oceans 10.1029/2022JC018799

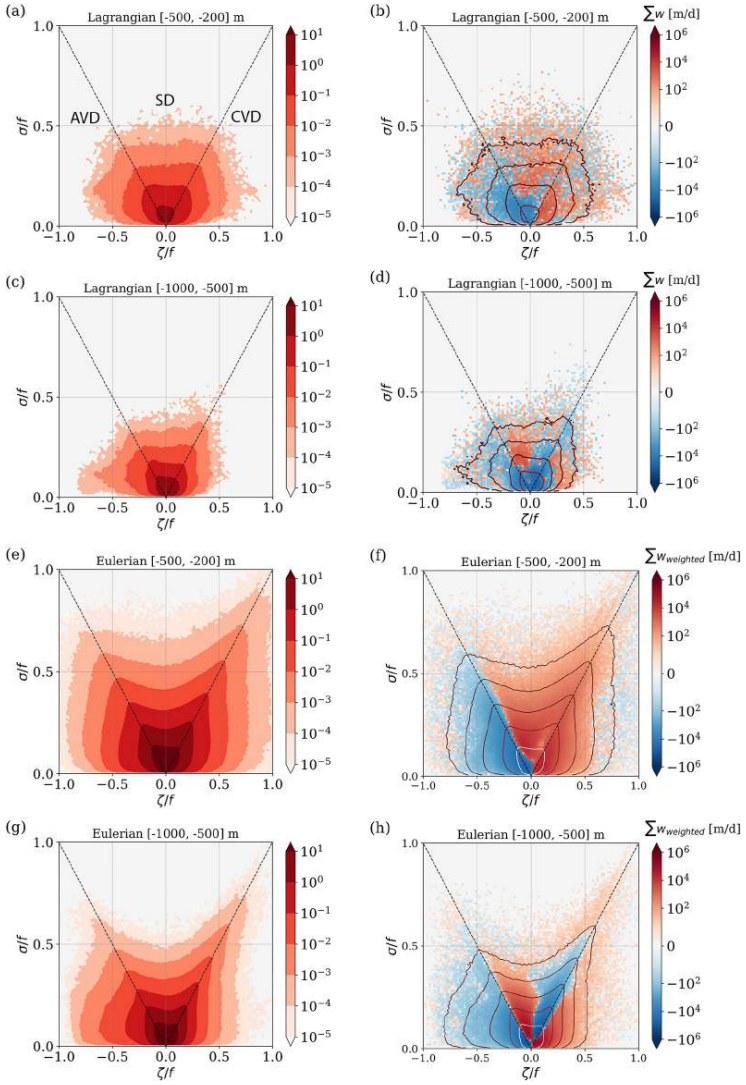

Figure 8. Comparison of Lagrangian trajectories (sinking velocity 50 m d^{-1}) and Eulerian field (domain size: 200 × 200 km) on the vorticity-strain space. Left column: Joint Probability Density Function (JPDF). The *x*-*y* space is divided into three regions: anticyclonic vorticity dominated (AVD), cyclonic vorticity dominated (CVD), and strain dominated (SD). Right column: vertical velocity *w* conditioned on the vorticity-strain space, shown as the sum of *w* in each bin, contoured by the particle density. The sum of Eulerian *w* is weighted by the thickness of each depth layer in the sigma coordinate. (a and b) For particle footprints in 200–500 m. (c and d) For particle footprints in 500–1,000 m. (e and f) For the Eulerian field in 200–500 m. (g and h) For the Eulerian field in 500–1,000 m.

Journal of Geophysical Research: Oceans 10.1029/2022JC018799

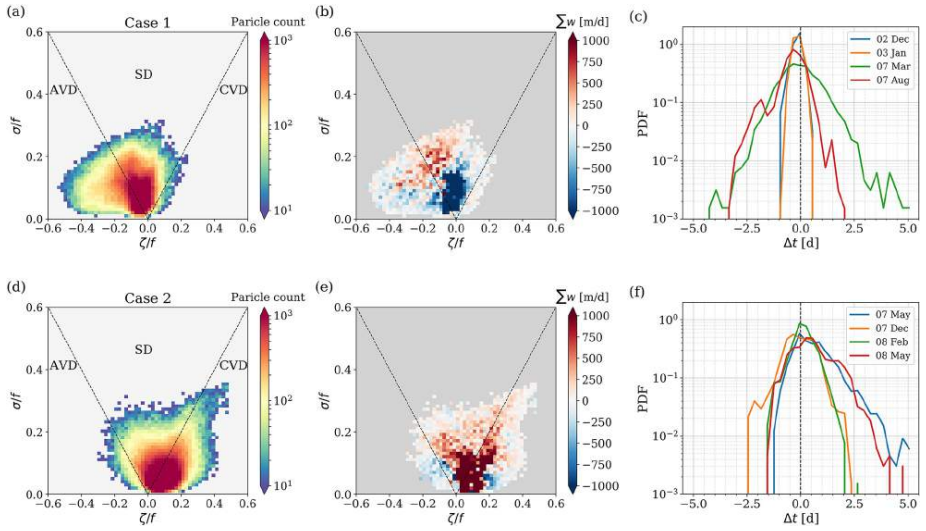

Figure 9. Composite plots of the eddy dominated periods: (a–c) Case 1: anticyclonic eddy-dominated periods; (d–f) Case 2: cyclonic eddy-dominated periods. From left to right columns are particle count on the vorticity-strain space, the conditioned sum w, and PDF of travel time anomaly Δt.

skewed PDF toward negative Δt, as more energetic eddies in spring allow particles to sample complex flow structures. Therefore, even the same type of mesoscale features can exert different impacts on the vertical dispersion of particles. Unlike the strain-dominated pattern in the anticyclone case, particle trajectories in cyclonic eddies concentrate in the CVD region with only a smaller portion in the SD part (Figure 9d). The cyclonic vortex is responsible for the majority of upward velocities recorded by particles, leading to a PDF of Δt significantly extended to the positive side, especially in spring months.

Overall, JPDFs show major trends here: at monthly time scales, anticyclonic eddies accelerate the downward transport while cyclonic eddies delay the descent of particles. However, the patchy vertical velocity patterns in mesoscale eddies are more complicated than the classic eddy-pumping mechanism that upwelling is always in cyclonic eddies and downwelling is always in anticyclonic eddies. This mechanism is more applicable in the period of formation and strengthening of eddies, whereas the case of eddy decay shows opposite patterns (Klein & Lapeyre, 2009). Furthermore, the vertical velocity patterns in eddies are not in general uniform. Instead, a set of upward and downward cells are formed extending from the center to the perimeter (Pilo et al., 2018). Besides, many other mechanisms including eddy propagation (McGillicuddy et al., 1995), eddy-eddy interactions (Pidcock et al., 2013) and submesoscale processes (Brannigan, 2016) may also contribute to the vertical velocity structure within the eddy. The complexity of mechanisms implies that a detailed analysis of individual eddies (e.g., eddy age and status, particle location) is required to link particle export with specific features.

4. Discussion and Conclusions

In this study, we backtracked virtual particles from locations of deep-moored sediment traps to the export depth using a realistic eddy-resolving simulation. We applied a set of dispersion metrics to characterize particle trajectories and link them with mesoscale dynamical features. Here we summarize the main conclusions and discuss the simplifications in our work and implications for future study.

Journal of Geophysical Research: Oceans 10.1029/2022JC018799

4.1. On the Simplifications

4.1.1. Export Depth

We found that mesoscale dynamics in the twilight zone (200–1,000 m) play a dominant role in shaping the statistical funnels based on several simplifications. We choose the base of the epipelagic layer (200 m) as the end depth of particle backtracking. The reason is that we are focusing on the fate of particles once they are formed and exported below the productive surface layer. However, the uniform end depth in our study is not precisely an export depth. The export depth, in reality, varies with time and space and differs for particles with different sinking velocities.

4.1.2. Particle Sinking Velocity

Another simplification is that we use constant sinking velocities ranging between 20 and 200 m d^{-1}. Most of our choices fall into the common range of sinking velocities from 50 to 200 m d^{-1} adopted in previous studies (Siegel & Deuser, 1997; Siegel et al., 2008; Waniek et al., 2000). It is noteworthy that 20 m d^{-1} has also been used in a few recent studies of sediment trap catchment area (Liu et al., 2018; Wekerle et al., 2018). However, particle sinking velocity is highly likely to vary with depth. Remineralization leads to a decrease in the size of particles and possibly in their sinking velocity. Dever et al. (2021) suggests remineralization processes promote the contribution of slow-sinking particles (0.025–5 m day^{-1}) to the POC export. For the fast-sinking particles in our study, we assume the impact of remineralization is modest due to the short travel time. This consideration is supported by observations at the PAP site that demonstrate that fast-sinking particles were sufficient to supply deep POC flux. In contrast, slow-sinking particles were likely to be entirely remineralized in the twilight zone (Riley et al., 2012).

Furthermore, processes including aggregation, fragmentation, and zooplankton grazing also change particle size, density, and hence sinking velocity during particle descent (Boyd & Trull, 2007; Guidi et al., 2007; Riley et al., 2012; Trull et al., 2008). Considering the sinking velocity varying with depth, the statistical funnel of particles reaching the trap will be a mixture of source regions for a wide range of sinking classes. Nevertheless, this study deals with the impact of mesoscale dynamics on the dispersion and travel time of particles assumed to be conservative in the mesopelagic layer. Future research is required to include processes behind the changes in particle size and sinking rate (which are beyond the scope of this study).

4.1.3. The Heterogeneity of Particle Sources

This study analyzes statistical funnels sampled by deep sediment traps without considering the heterogeneity of particle sources. We identify the distribution of potential particle sources but do not address the temporal and spatial variability of carbon fluxes at depth. Both satellite observations (Zhang et al., 2019) and modeling investigations (Lévy et al., 2014) have shown undoubtedly that the dynamics at medium and small scales strongly control the intensity of the primary production. The intensity of primary production largely constrains particle size spectra: higher production is generally associated with larger sizes (Kostadinov et al., 2009). Although simple relationships between particle size and sinking velocity are not straightforward (Iversen & Lampitt, 2020), to a first approximation, these two parameters can be related by Stokes' law (Lerman et al., 1974; Laurenceau-Cornec et al., 2020). Therefore, the next step will be to examine the impact of sinking velocity variability by weighting the particle size distribution correlated with the PP intensity at the time and location of particle formation. The primary production distributions could be estimated by coupling the dynamic model with a simple NPZD model. From a model perspective, this exercise will give us the first information on the eddy-scale variability of carbon fluxes in the deep ocean with a daily resolution. Also, it will allow a first analysis of the (de)coupling between export production below the mixed layer and deep fluxes at mesoscales (with nevertheless, the conservation of particles as a strong hypothesis at the first stage). In addition, by using "realistic" simulations from operational models, these backward simulations can provide relevant information about sources and time lags of particles collected in sediment traps during process study cruises.

4.2. Implications for Studying the POC Flux

4.2.1. Submesoscale Motions Below the Mixed Layer

From a physical perspective, the end depth of 200 m is close to the typical deep winter mixed layer depth in our study region. As such, submesoscale processes, which are more intense within the winter mixed layer, appear to

Journal of Geophysical Research: Oceans 10.1029/2022JC018799

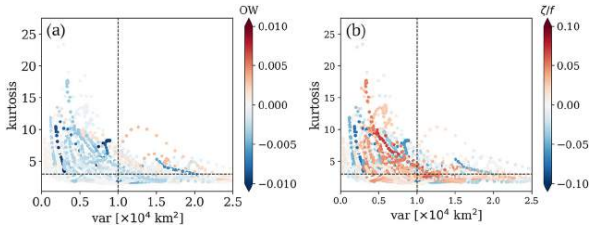

Figure 10. Relation between kurtosis and variance from 30-day moving average time series for 50 m d^{-1}, trap 1,000 m, colored by (a) Okubo-Weiss parameter and (b) relative vorticity. The dashed lines mark variance = 1×10^4 km^2 and kurtosis = 3.

play a minor role in particle transport below 200 m. Previous studies have found that submesoscale dynamics can enhance particle export through advecting slow-sinking particles (Dever et al., 2021) or restratifying the mixed layer to reduce the impact of vertical mixing on gravitational settling (Taylor et al., 2020). The rapid accumulation of particles has also been observed in the surface convergence zones associated with large vertical velocities (D'Asaro et al., 2018; Poje et al., 2014), such areas also have the potential to be hot spots of particle export to the deep ocean. However, how much submesoscale motions come into play below the mixed layer remains unclear.

Although highlighting the importance of mesoscale dynamics, this study points to an emergence of submesoscale motions below the mixed layer. There is a skewness in the vorticity-strain JPDF of the Eulerian field, extending along $\sigma = \zeta$ toward the cyclonic side of the frontal region. In addition, the asymmetry in the travel time anomaly reflects a skewed distribution of w toward downward velocity. The two findings unveil the manifestation of submesoscale motions characterized by positive skewness of relative vorticity (Buckingham et al., 2016; Rudnick, 2001) and an enhancement of downwelling (Dever et al., 2021; Thomas et al., 2008). Thus, higher resolution modeling is in demand to disentangle the impact of smaller scales in the mesopelagic layer, which may not be negligible. Yet we should keep in mind that the influence of submesoscale motions to export in this region is limited due to the constricted overlap of strong submesoscale instabilities in winter and large particle export in spring and summer (Erickson & Thompson, 2018).

4.2.2. The Sampling Design of a Regional Survey

This study underlines the impact of mesoscale dynamics in the twilight zone on the 3D transport of particles at a temperate open-ocean site. The presence of coherent mesoscale eddies can effectively "trap" particles within a local area (<100 km) over a monthly time scale. Given the smaller statistical funnel confined by eddies, the export flux measured by the deep-ocean sediment traps is easier to be correlated to the surface production when a coherent structure persists right above the trap. This finding has implications for the sampling design in a regional survey, for example, the cruise scheduled in 2023 for the APERO project. As is often done during field surveys, the location of process study stations can be identified by focusing on these coherent mesoscale patterns, highlighted by satellite observations and modeling outputs. However, these structures only cover about 20% of the ocean, and particles are not always completely moving with these eddies. The eight eddy-dominated months in our analysis are based on the PDF of horizontal particle displacements. In general, high kurtosis correspond to low variance, associated with a negative Okubo-Weiss parameter and high relative vorticity (Figure 10). It indicates that coherent structures lead to hot spots of particle sources. Nevertheless, the continuum between coherent structures and turbulent flows (high variance, small kurtosis close to 3) represents a large portion of the ocean and should also be sampled. Thus sampling the remaining more turbulent and chaotic ocean is fundamental and challenging.

4.2.3. Generalization to Other Regions

While we expect our results to qualitatively hold in other regions of the ocean, the size of the statistical funnel and amplitude of the travel time anomalies will be a function of the local hydrodynamical properties, in particular of the mesoscale turbulence. A first attempt to generalize our results can be made by casting them in terms of non-dimensional parameters. We use the containment radii ($R_{95\%}$) and normalized root-mean-square travel time

Journal of Geophysical Research: Oceans 10.1029/2022JC018799

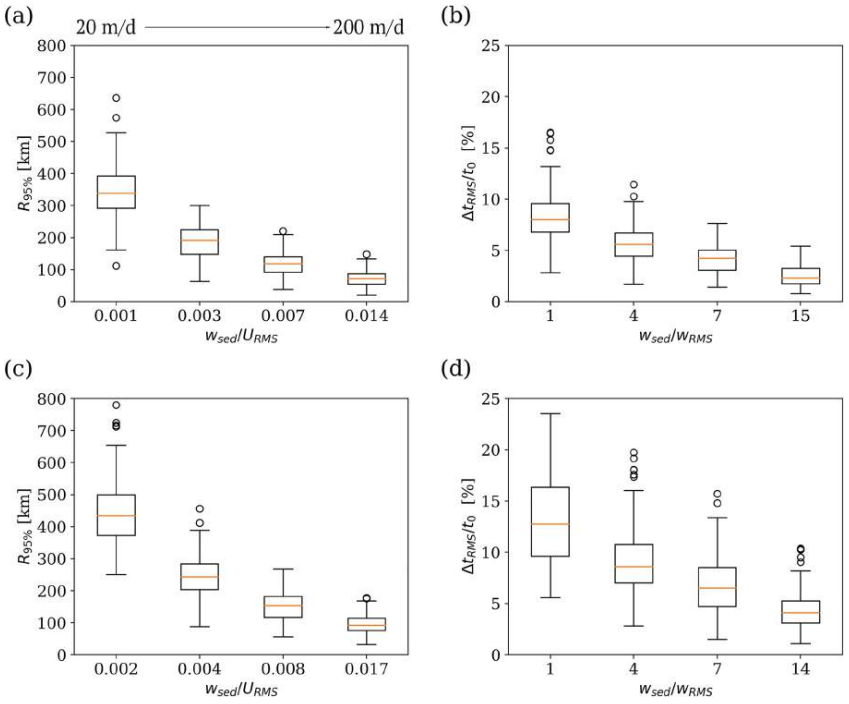

Figure 11. Full-period monthly horizontal and vertical dispersion metrics as a function of the ratio of sinking speed (from left to right: 20, 50, 100, 200 m day^{-1}) to the flow velocity. Top panel for particles backtracked from 1,000 m: (a) The radial distance containing 95% of the source region ($R_{95\%}$), corresponding to the ratio of particle sinking velocity (w_{sed}) to the root-mean-squared (RMS) horizontal current velocity (U_{RMS}). (b) RMS travel time anomaly (Δt_{RMS}) normalized by standard travel time t_0, corresponding to the ratio of particle sinking velocity to the RMS vertical flow velocity (w_{RMS}). Bottom panel (c and d): same as a and b, for particles backtracked from 2,000 m.

anomaly ($\Delta t_{RMS}/t_0$) to describe horizontal and vertical dispersion of particles, respectively, and relate them with the ratio of particle sinking velocity to the flow velocity (Figure 11). The size of particle source regions for the trap at 1,000 m has $R_{95\%}$ mainly in the range of 300–400 km for w_{sed}/U_{RMS} at 0.001. It decreases by half when w_{sed}/U_{RMS} increases to 0.003. For a much higher speed ratio like 0.007 and 0.014, the containment radii remain at around 100 km or less. The vertical dispersion is most significant when w_{sed}/w_{RMS} is 1, with the percentage of travel time anomaly close to 15% (~5 days). The deviation matters for the short-term deployment of sediment traps during the bloom/post-bloom period. Note that the relationship between dispersion metrics and speed ratio depends on the trap depth. For the trap at 2,000 m, the source region expands only by a few tens of kilometers compared to 1,000 m. The travel time anomaly increases more obviously. The 75th percentile for 20 m day^{-1} is more than 15%, which is equivalent to 15 days. Even for 50 m day^{-1}, it is around 10% (4 days). If such relationships hold for other dynamical regimes, these numbers could be a reference for estimating the source region and time lags of particle sinking, given by the current velocity data at other locations.

Moreover, we proposed a three-layer structure of dynamical regimes, as reflected by flow properties and horizontal dispersion in 2D experiments. In particular, the PAP site is characterized by a moderate mesoscale activity compared to other regions like the Gulf of Mexico (Liu et al., 2018) and the Arctic Ocean (Wekerle et al., 2018). The vertical structuring of particle dispersion associated with small-scale dynamics (200–500 m: high EKE and

Journal of Geophysical Research: Oceans 10.1029/2022JC018799

w, 500–1,000 m: still relatively high EKE, but small *w*; below 1,000 m: quiet, smooth flows) must be confronted with different situations. It is necessary to verify the generalization of this finding in other regions. Future work could be first at a regional scale to check the homogeneity of dispersion statistics in the inter gyre region of the North Atlantic, near the PAP station. Second, a similar analysis could be conducted at other long-term observatory stations (e.g., BATS, HOT) and in situ experiments in Eastern Boundary Upwelling Systems, where many dedicated cruises have been conducted. Lastly, different turbulent and dynamical regimes such as Western Boundary Currents and the Southern Ocean, where the correlation between strong turbulent regimes and horizontal velocities remains a big issue, are also hotspots worth studying.

Data Availability Statement

Coastal and Regional Ocean COmmunity ocean model is available at https://www.croco-ocean.org. The Lagrangian particle tracking software Pyticles is available at https://github.com/Mesharou/Pyticles and has been published on Zenodo at https://doi.org/10.5281/zenodo.4973786.

Acknowledgments
This work was supported by the ISblue project, an Interdisciplinary graduate school for the blue planet (ANR-17-EURE-0015), and co-funded by a grant from the French government under the program "Investissements d'Avenir." This manuscript contributes to the APERO project funded by the National Research Agency under the grant APERO [Grant No. ANR-21-CE01-0027] and by the French LEFE-Cyber program. Simulations were performed using HPC resources from GENCI-TGCC (grant 2018-A0050107638) and from DATARMOR of "Pôle de Calcul Intensif pour la Mer" at Ifremer, Brest, France. The authors thank Mathieu Le Corre for providing CROCO simulation outputs. The authors appreciate the reviewers for their constructive comments and insightful suggestions that significantly helped improve this manuscript.

References

Armstrong, R., Lee, C., Hedges, J., Honjo, S., & Wakeham, S. (2001). A new, mechanistic model for organic carbon fluxes in the ocean based on the quantitative association of POC with ballast minerals. *Deep Sea Research Part II: Topical Studies in Oceanography*, *49*(1–3), 219–236. https://doi.org/10.1016/s0967-0645(01)00101-1

Asper, V., Deuser, W., Knauer, G., & Lohrenz, S. (1992). Rapid coupling of sinking particle fluxes between surface and deep ocean waters. *Nature*, *357*(6380), 670–672. https://doi.org/10.1038/357670a0

Balwada, D., Xiao, Q., Smith, S., Abernathey, R., & Gray, A. (2021). Vertical fluxes conditioned on vorticity and strain reveal submesoscale ventilation. *Journal of Physical Oceanography*, *51*(9), 2883–2901. https://doi.org/10.1175/jpo-d-21-0016.1

Berti, S., & Lapeyre, G. (2021). Lagrangian pair dispersion in upper-ocean turbulence in the presence of mixed-layer instabilities. *Physics of Fluids*, *33*(3), 036603. https://doi.org/10.1063/5.0041036

Boyd, P., Claustre, H., Levy, M., Siegel, D., & Weber, T. (2019). Multi-faceted particle pumps drive carbon sequestration in the ocean. *Nature*, *568*(7752), 327–335. https://doi.org/10.1038/s41586-019-1098-2

Boyd, P., & Trull, T. (2007). Understanding the export of biogenic particles in oceanic waters: Is there consensus? *Progress in Oceanography*, *72*(4), 276–312. https://doi.org/10.1016/j.pocean.2006.10.007

Brannigan, L. (2016). Intense submesoscale upwelling in anticyclonic eddies. *Geophysical Research Letters*, *43*(7), 3360–3369. https://doi.org/10.1002/2016gl067926

Buckingham, C., Naveira Garabato, A., Thompson, A., Brannigan, L., Lazar, A., Marshall, D., et al. (2016). Seasonality of submesoscale flows in the ocean surface boundary layer. *Geophysical Research Letters*, *43*(5), 2118–2126. https://doi.org/10.1002/2016gl068009

Buesseler, K., Lamborg, C., Boyd, P., Lam, P., Trull, T., Bidigare, R., et al. (2007). Revisiting carbon flux through the ocean's twilight zone. *Science*, *316*(5824), 567–570. https://doi.org/10.1126/science.1137959

Burd, A., Hansell, D., Steinberg, D., Anderson, T., Arístegui, J., Baltar, F., et al. (2010). Assessing the apparent imbalance between geochemical and biochemical indicators of meso- and bathypelagic biological activity: What the @$#! is wrong with present calculations of carbon budgets? *Deep Sea Research Part II: Topical Studies in Oceanography*, *57*(16), 1557–1571. https://doi.org/10.1016/j.dsr2.2010.02.022

Chelton, D., Deszoeke, R., Schlax, M., Naggar, K., & Siwertz, N. (1998). Geographical variability of the first baroclinic rossby radius of deformation. *Journal of Physical Oceanography*, *28*(3), 28–460. https://doi.org/10.1175/1520-0485(1998)028<0433:gvotfb>2.0.co;2

Coatanoan, C. (2021). *Mixed layer depth in the North Atlantic Ocean*. Product Information Document (PIDoc). https://doi.org/10.13155/79588

D'Asaro, E., Shcherbina, A., Klymak, J., Molemaker, J., Novelli, G., Guigand, C., et al. (2018). Ocean convergence and the dispersion of flotsam. *Proceedings of the National Academy of Sciences*, *115*(6), 1162–1167. https://doi.org/10.1073/pnas.1718453115

Deuser, W., Muller-Karger, F., Evans, R., Brown, O., Esaias, W., & Feldman, G. (1990). Surface-ocean color and deep-ocean carbon flux: How close a connection? Deep sea research Part A. *Oceanographic Research Papers*, *37*(8), 1331–1343.

Deuser, W., Muller-Karger, F., & Hemleben, C. (1988). Temporal variations of particle fluxes in the deep subtropical and tropical north Atlantic: Eulerian versus Lagrangian effects. *Journal of Geophysical Research*, *93*(C6), 6857. https://doi.org/10.1029/jc093ic06p06857

Deuser, W., & Ross, E. (1980). Seasonal change in the flux of organic carbon to the deep Sargasso Sea. *Nature*, *283*(5745), 364–365. https://doi.org/10.1038/283364a0

Dever, M., Nicholson, D., Omand, M., & Mahadevan, A. (2021). Size-differentiated export flux in different dynamical regimes in the ocean. *Global Biogeochemical Cycles*, *35*(3). https://doi.org/10.1029/2020gb006764

Erickson, Z., & Thompson, A. (2018). The seasonality of physically driven export at submesoscales in the northeast Atlantic Ocean. *Global Biogeochemical Cycles*. https://doi.org/10.1029/2018gb005927

Falkowski, P., Barber, R., & Smetacek, V. (1998). Biogeochemical controls and feedbacks on ocean primary production. *Science*, *281*(5374), 200–206. https://doi.org/10.1126/science.281.5374.200

Guidi, L., Calil, P., Duhamel, S., Björkman, K., Doney, S., Jackson, G., et al. (2012). Does eddy-eddy interaction control surface phytoplankton distribution and carbon export in the north Pacific subtropical gyre? *Journal of Geophysical Research*, *117*(G2). https://doi.org/10.1029/2012jg001984

Guidi, L., Stemmann, L., Legendre, L., Picheral, M., Prieur, L., & Gorsky, G. (2007). Vertical distribution of aggregates (.110 mm) and mesoscale activity in the northeastern Atlantic: Effects on the deep vertical export of surface carbon. *Liminology and Oceanography*, *52*(1), 7–18. https://doi.org/10.4319/lo.2007.52.1.0007

Gula, J., & Collin, J. (2021). *Pyticles: A Python/Fortran hybrid parallelized code for 3D Lagrangian particles advection using ROMS/CROCO model data*. Zenodo. https://doi.org/10.5281/zenodo.4973786

Hartman, S., Larkin, K., Lampitt, R., Lankhorst, M., & Hydes, D. (2010). Seasonal and inter-annual biogeochemical variations in the porcupine abyssal plain 2003–2005 associated with winter mixing and surface circulation. *Deep Sea Research Part II: Topical Studies in Oceanography*, *57*(15), 1303–1312. https://doi.org/10.1016/j.dsr2.2010.01.007

Henson, S., Yool, A., & Sanders, R. (2015). Variability in efficiency of particulate organic carbon export: A model study: Variability in export ratio. *Global Biogeochemical Cycles*, *29*(1), 33–45. https://doi.org/10.1002/2014gb004965

Iversen, M., & Lampitt, R. (2020). Size does not matter after all: No evidence for a size-sinking relationship for marine snow. *Progress in Oceanography*, *189*, 102445. https://doi.org/10.1016/j.pocean.2020.102445

Klein, P., & Lapeyre, G. (2009). The oceanic vertical pump induced by mesoscale and submesoscale turbulence. *Annual Review of Marine Science*, *1*(1), 351–375. https://doi.org/10.1146/annurev.marine.010908.163704

Kostadinov, T., Siegel, D., & Maritorena, S. (2009). Retrieval of the particle size distribution from satellite ocean color observations. *Journal of Geophysical Research*, *114*(C9), C09015. https://doi.org/10.1029/2009jc005303

LaCasce, J. (2008). Statistics from Lagrangian observations. *Progress in Oceanography*, *77*(1), 1–29. https://doi.org/10.1016/j.pocean.2008.02.002

Lampitt, R., & Antia, A. (1997). Particle flux in deep seas: Regional characteristics and temporal variability. *Deep Sea Research Part I: Oceanographic Research Papers*, *44*(8), 1377–1403. https://doi.org/10.1016/s0967-0637(97)00020-4

Lampitt, R., Salter, I., de Cuevas, B., Hartman, S., Larkin, K., & Pebody, C. (2010). Long-term variability of downward particle flux in the deep northeast atlantic: Causes and trends. *Deep Sea Research Part II: Topical Studies in Oceanography*, *57*(15), 1346–1361. https://doi.org/10.1016/j.dsr2.2010.01.011

Laurenceau-Cornec, E., Le Moigne, F. C., Gallinari, M., Moriceau, B., Toullec, J., Iversen, M., et al. (2020). New guidelines for the application of Stokes' models to the sinking velocity of marine aggregates. *Limnology & Oceanography*, *65*(6), 1264–1285. https://doi.org/10.1002/lno.11388

Le Cann, B. (2005). Observed mean and mesoscale upper ocean circulation in the midlatitude northeast atlantic. *Journal of Geophysical Research*, *110*(C7), C07S05. https://doi.org/10.1029/2004jc002768

Le Corre, M., Gula, J., & Tréguier, A.-M. (2020). Barotropic vorticity balance of the north atlantic subpolar gyre in an eddy-resolving model. *Ocean Science*, *16*(2), 451–468. https://doi.org/10.5194/os-16-451-2020

Le Moigne, F. A. C., Henson, S. A., Sanders, R. J., & Madsen, E. (2013). Global database of surface ocean particulate organic carbon export fluxes diagnosed from the 234th technique. *Earth System Science Data*, *5*(2), 295–304. https://doi.org/10.5194/essd-5-295-2013

Lerman, A., Lal, D., & Dacey, M.F. (1974). Stokes' settling and chemical reactivity of suspended particles in natural waters. In R.J. Gibbs, (Ed.), *Suspended solids in water* (Vol. *4*). Springer.

Lévy, M., Ferrari, R., Franks, P., Martin, A., & Rivière, P. (2012). Bringing physics to life at the submesoscale. *Geophysical Research Letters*, *39*(14), L14602. https://doi.org/10.1029/2012gl052756

Lévy, M., Franks, P., & Smith, K. (2018). The role of submesoscale currents in structuring marine ecosystems. *Nature Communications*, *9*(1), 4758. https://doi.org/10.1038/s41467-018-07059-3

Lévy, M., Jahn, O., Dutkiewicz, S., & Follows, M. (2014). Phytoplankton diversity and community structure affected by oceanic dispersal and mesoscale turbulence: Dispersal impact on plankton diversity. *Limnology and Oceanography: Fluids and Environments*, *4*(1), 67–84. https://doi.org/10.1215/21573689-2768549

Liu, G., Bracco, A., & Passow, U. (2018). The influence of mesoscale and submesoscale circulation on sinkingparticles in the northern gulf of Mexico. *Elementa: Science of the Anthropocene*, *6*(1), 36. https://doi.org/10.1525/elementa.292

Mahadevan, A. (2016). The impact of submesoscale physics on primary productivity of plankton. *Annual Review of Marine Science*, *8*(1), 161–184. https://doi.org/10.1146/annurev-marine-010814-015912

Mahadevan, A., & Tandon, A. (2006). An analysis of mechanisms for submesoscale vertical motion at ocean fronts. *Ocean Modelling*, *14*(3–4), 241–256. https://doi.org/10.1016/j.ocemod.2006.05.006

Martin, A., Boyd, P., Buesseler, K., Cetinic, I., Claustre, H., Giering, S., et al. (2020). Study the twilight zone before it is too late. *Nature*, *580*(7801), 26–28. https://doi.org/10.1038/d41586-020-00915-7

McGillicuddy, D. (2016). Mechanisms of physical-biological-biogeochemical interaction at the oceanic mesoscale. *Annual Review of Marine Science*, *8*(1), 125–159. https://doi.org/10.1146/annurev-marine-010814-015606

McGillicuddy, D., Robinson, A., & McCarthy, J. (1995). Coupled physical and biological modelling of the spring bloom in the North Atlantic (ii): Three dimensional bloom and post-bloom processes. *Deep Sea Research Part I: Oceanographic Research Papers*, *42*(8), 1359–1398. https://doi.org/10.1016/0967-0637(95)00035-5

McWilliams, J. (2008). The nature and consequences of oceanic eddies. In M. Hecht & H. Hasumi (Eds.) *Geophysical monograph series* (Vol. 177, pp. 5–15). American Geophysical Union.

Olson, D. (1991). Rings in the ocean. *Annual Review of Earth and Planetary Sciences*, *19*(1), 283–311. https://doi.org/10.1146/annurev.ea.19.050191.001435

Pidcock, R., Martin, A., Allen, J., Painter, S., & Smeed, D. (2013). The spatial variability of vertical velocity in an Iceland basin eddy dipole. *Deep Sea Research Part I: Oceanographic Research Papers*, *72*, 121–140. https://doi.org/10.1016/j.dsr.2012.10.008

Pietri, A., Capet, X., d'Ovidio, F., Levy, M., Le Sommer, J., Molines, J.-M., & Giordani, H. (2021). Skills and limitations of the adiabatic omega equation: How effective is it to retrieve oceanic vertical circulation at mesoscale and submesoscale? *Journal of Physical Oceanography*, *51*(3), 931–954. https://doi.org/10.1175/jpo-d-20-0052.1

Pilo, G., Oke, P., Coleman, R., Rykova, T., & Ridgway, K. (2018). Patterns of vertical velocity induced by eddy distortion in an ocean model: Vertical velocity and eddy distortion. *Journal of Geophysical Research: Oceans*, *123*(3), 2274–2292. https://doi.org/10.1002/2017jc013298

Poje, A., Haza, A., Özgökmen, T., Magaldi, M., & Garraffo, Z. (2010). Resolution dependent relative dispersion statistics in a hierarchy of ocean models. *Ocean Modelling*, *31*(1–2), 36–50. https://doi.org/10.1016/j.ocemod.2009.09.002

Poje, A., Ozgokmen, T., Lipphardt, B., Haus, B., Ryan, E., Haza, A., et al. (2014). Submesoscale dispersion in the vicinity of the deepwater horizon spill. *Proceedings of the National Academy of Sciences*, *111*(35), 12693–12698. https://doi.org/10.1073/pnas.1402452111

Qiu, Z., Doglioli, A., & Carlotti, F. (2014). Using a Lagrangian model to estimate source regions of particles in sediment traps. *Science China Earth Sciences*, *57*(10), 2447–2456. https://doi.org/10.1007/s11430-014-4880-x

Riley, J., Sanders, R., Marsay, C., Le Moigne, F., Achterberg, E., & Poulton, A. (2012). The relative contribution of fast and slow sinking particles to ocean carbon export: Export of fast and slow sinking POC. *Global Biogeochemical Cycles*, *26*(1). https://doi.org/10.1029/2011gb004085

Rudnick, D. L. (2001). On the skewness of vorticity in the upper ocean. *Geophysical Research Letters*, *28*(10), 2045–2048. https://doi.org/10.1029/2000gl012265

Sanders, R., Henson, S., Koski, M., De La Rocha, C., Painter, S., Poulton, A., et al. (2014). The biological carbon pump in the north atlantic. *Progress in Oceanography*, *129*, 200–218. https://doi.org/10.1016/j.pocean.2014.05.005

Journal of Geophysical Research: Oceans 10.1029/2022JC018799

Shchepetkin, A., & McWilliams, J. (2005). The regional oceanic modeling system (roms): A split-explicit, free-surface, topography-following-coordinate oceanic model. *Ocean Modelling*, *9*(4), 347–404. https://doi.org/10.1016/j.ocemod.2004.08.002

Siegel, D., Buesseler, K., Behrenfeld, M., Benitez-Nelson, C., Boss, E., Brzezinski, M., et al. (2016). Prediction of the export and fate of global ocean net primary production: The exports science plan. *Frontiers in Marine Science*, *3*. https://doi.org/10.3389/fmars.2016.00022

Siegel, D., & Deuser, W. (1997). Trajectories of sinking particles in the sargasso sea: Modeling of statistical funnels above deep-ocean sediment traps. *Deep Sea Research Part I: Oceanographic Research Papers*, *44*(9–10), 1519–1541. https://doi.org/10.1016/s0967-0637(97)00028-9

Siegel, D., Fields, E., & Buesseler, K. (2008). A bottom-up view of the biological pump: Modeling source funnels above ocean sediment traps. *Deep Sea Research Part I: Oceanographic Research Papers*, *55*(1), 108–127. https://doi.org/10.1016/j.dsr.2007.10.006

Siegel, D., Granata, T., Michaels, A., & Dickey, T. (1990). Mesoscale eddy diffusion, particle sinking, and the interpretation of sediment trap data. *Journal of Geophysical Research*, *95*(C4), 5305. https://doi.org/10.1029/jc095ic04p05305

Siegelman, L., Klein, P., Rivière, P., Thompson, A., Torres, H., Flexas, M., & Menemenlis, D. (2020). Enhanced upward heat transport at deep submesoscale ocean fronts. *Nature Geoscience*, *13*(1), 50–55. https://doi.org/10.1038/s41561-019-0489-1

Stukel, M., Aluwihare, L., Barbeau, K., Chekalyuk, A., Goericke, R., Miller, A., et al. (2017). Mesoscale ocean fronts enhance carbon export due to gravitational sinking and subduction. *Proceedings of the National Academy of Sciences*, *114*(6), 1252–1257. https://doi.org/10.1073/pnas.1609435114

Taylor, J. R., Smith, K. M., & Vreugdenhil, C. A. (2020). The influence of submesoscales and vertical mixing on the export of sinking tracers in large-eddy simulations. *Journal of Physical Oceanography*, *50*(5), 1319–1339. https://doi.org/10.1175/jpo-d-19-0267.1

Thomas, L. N., Tandon, A., & Mahadevan, A. (2008). Submesoscale processes and dynamics. In M. W. Hecht & H. Hasumi (Eds.), *Geophysical Monograph Series* (Vol. 177, pp. 17–38). American Geophysical Union.

Trull, T., Bray, S., Buesseler, K., Lamborg, C., Manganini, S., Moy, C., & Valdes, J. (2008). In situ measurement of mesopelagic particle sinking rates and the control of carbon transfer to the ocean interior during the vertical flux in the global ocean (vertigo) voyages in the north Pacific. *Deep Sea Research Part II: Topical Studies in Oceanography*, *55*(14–15), 1684–1695. https://doi.org/10.1016/j.dsr2.2008.04.021

Turner, J. (2002). Zooplankton fecal pellets, marine snow and sinking phytoplankton blooms. *Aquatic Microbial Ecology*, *27*, 57–102. https://doi.org/10.3354/ame027057

Turner, J. (2015). Zooplankton fecal pellets, marine snow, phytodetritus and the ocean's biological pump. *Progress in Oceanography*, *130*, 205–248. https://doi.org/10.1016/j.pocean.2014.08.005

Vic, C., Gula, J., Roullet, G., & Pradillon, F. (2018). Dispersion of deep-sea hydrothermal vent effluents and larvae by submesoscale and tidal currents. *Deep Sea Research Part I: Oceanographic Research Papers*, *133*, 1–18. https://doi.org/10.1016/j.dsr.2018.01.001

Vic, C., Hascoët, S., Gula, J., Huck, T., & Maes, C. (2022). Oceanic mesoscale cyclones cluster surface Lagrangian material. *Geophysical Research Letters*, *49*(4), e2021GL097488. https://doi.org/10.1029/2021gl097488

Villa-Alfageme, M., de Soto, F., Le Moigne, F. A. C., Giering, S. L. C., Sanders, R., & García-Tenorio, R. (2014). Observations and modeling of slow-sinking particles in the twilight zone. *Global Biogeochemical Cycles*, *28*(11), 1327–1342. https://doi.org/10.1002/2014gb004981

Waite, A., Stemmann, L., Guidi, L., Calil, P., Hogg, A., Feng, M., et al. (2016). The wineglass effect shapes particle export to the deep ocean in mesoscale eddies: The wineglass effect. *Geophysical Research Letters*, *43*(18), 9791–9800. https://doi.org/10.1002/2015gl066463

Waniek, J., Koeve, W., & Prien, R. (2000). Trajectories of sinking particles and the catchment areas above sediment traps in the northeast Atlantic. *Journal of Marine Research*, *58*(6), 983–1006. https://doi.org/10.1357/002224000763485773

Wekerle, C., Krumpen, T., Dinter, T., von Appen, W.-J., Iversen, M., & Salter, I. (2018). Properties of sediment trap catchment areas in fram strait: Results from Lagrangian modeling and remote sensing. *Frontiers in Marine Science*, *5*, 407. https://doi.org/10.3389/fmars.2018.00407

Yu, X., Naveira Garabato, A., Martin, A., Buckingham, C., Brannigan, L., & Su, Z. (2019). An annual cycle of submesoscale vertical flow and restratification in the upper ocean. *Journal of Physical Oceanography*, *49*(6), 1439–1461. https://doi.org/10.1175/jpo-d-18-0253.1

Zhang, Z., Qiu, B., Klein, P., & Travis, S. (2019). The influence of geostrophic strain on oceanic ageostrophic motion and surface chlorophyll. *Nature Communications*, *10*(1), 2838. https://doi.org/10.1038/s41467-019-10883-w

3.3 Supplementary Information

JOURNAL OF GEOPHYSICAL RESEARCH

Effects of mesoscale dynamics on the path of sinking particles to the deep ocean: A modelling study

Lu Wang[1], Jonathan Gula[2,3], Jérémy Collin[1], Laurent Mémery[1]

[1]Univ Brest, CNRS, IRD, Ifremer, Laboratoire des Sciences de l'Environnement Marin (LEMAR), IUEM, Plouzané, France

[2]Univ Brest, CNRS, IRD, Ifremer, Laboratoire d'Océanographie Physique et Spatiale (LOPS), IUEM, Plouzané, France

[3]Institut Universitaire de France (IUF), Paris, France

Contents of this file

1. Figures S1 to S4

May 11, 2022, 7:20pm

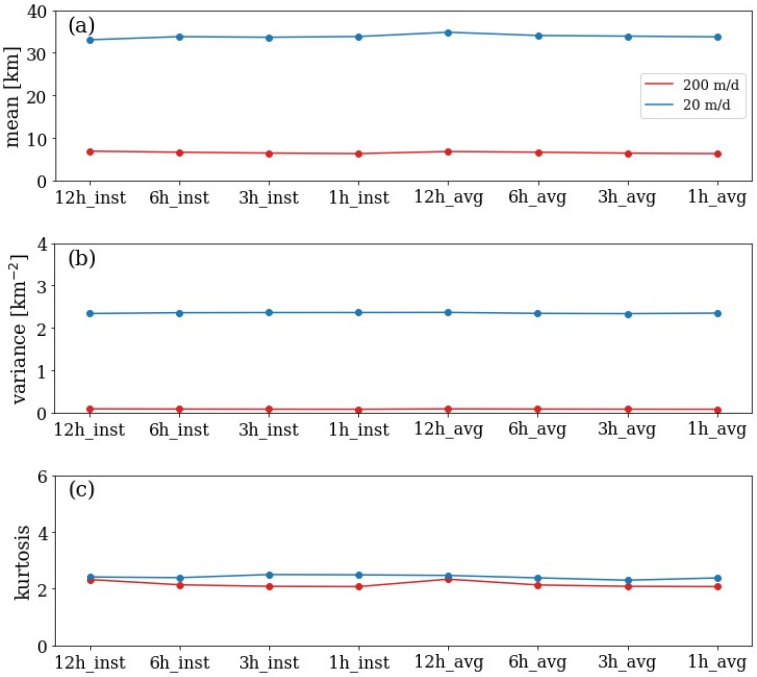

Figure S1. Horizontal dispersion in the sensitivity test runs, assessed by metrics derived from the PDF of horizontal displacements: (a) mean; (b) variance; (c) kurtosis. The x-axis is labeled by the types of outputs used for test runs: instantaneous ('inst') or average ('avg') at 12/6/3/1 hour intervals. All three metrics show minor changes with output types.

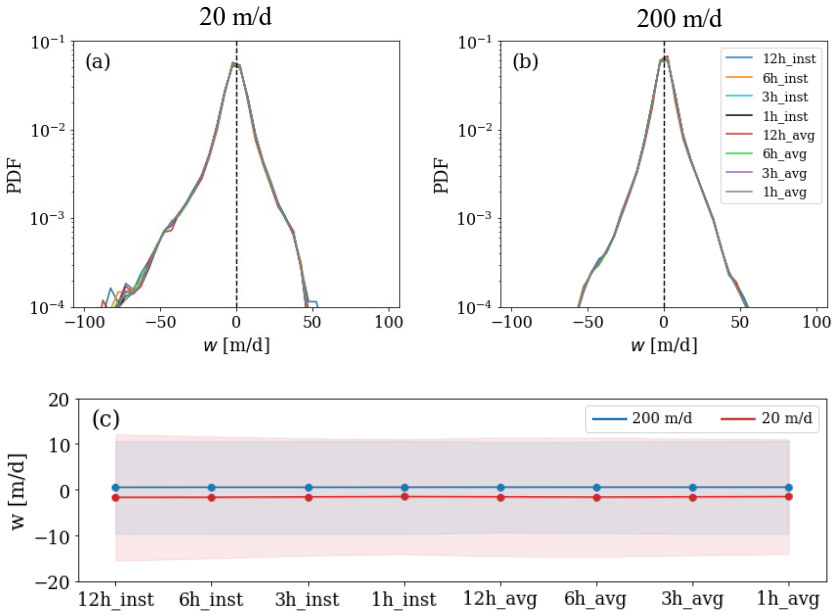

Figure S2. Vertical velocity w recorded by particles in the sensitivity test runs: (a) PDF of w for 20 m/d; (b) for 200 m/d; (c) mean w with standard deviations. Again, similar to the horizontal dispersion, the types of outputs do not affect particle dynamics in the vertical.

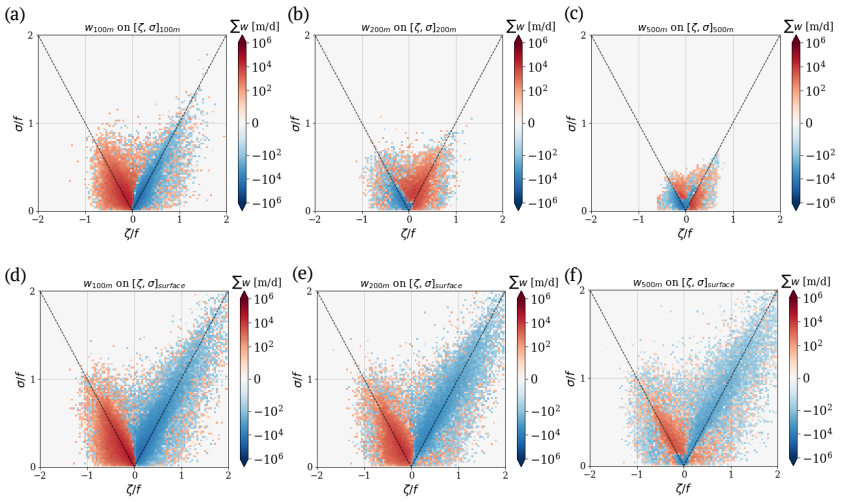

Figure S3. Vertical velocity at a specific depth (100 m, 200 m, and 500 m, from left to right), shown as the sum of w in each bin: (a-c) conditioned on the vorticity-strain space at corresponding depth; (d-e) on the vorticity-strain space at the surface (10 m). The top and bottom panel comparison shows that the w pattern changes dramatically when conditioned on different vorticity-strain spaces. Also, the comparison between the three columns indicates the patterns differ for depths within and below the mixed layer.

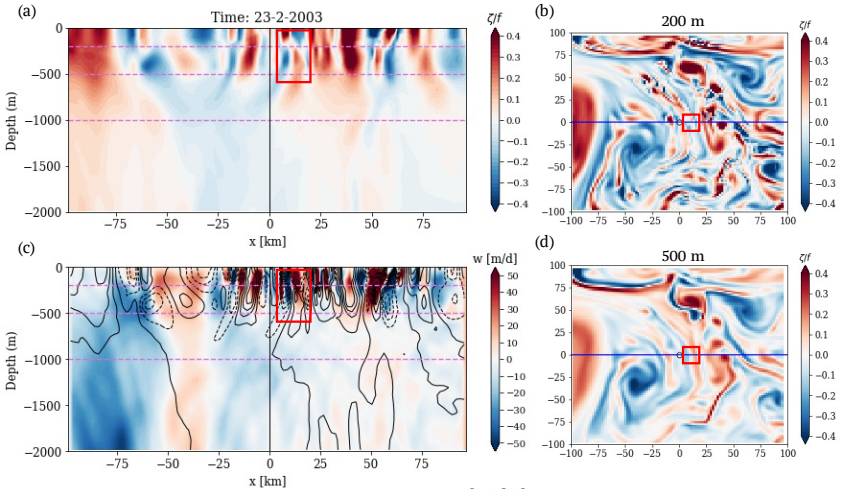

Figure S4. Snapshots of the flow field on 23 Feb 2003: (a) A section of relative vorticity; (c) A section of vertical velocity with relative vorticity contours (solid: cyclonic, dashed: anticyclonic). The location of the section is marked as the blue line in horizontal maps of relative vorticity at (b) 200 m and (d) 500 m. The example of structures showing changed signs of relative vorticity with depth is marked in the red box. Relative vorticity shows an opposite sign for the upper 200 m and below 200 m, associated with a homogeneous vertical velocity cell. Such structures are common in our time series.

Chapter 4

Connecting the deep collection of particles with surface ocean signatures

This chapter investigates how mesoscale dynamics impact the heterogeneity of particle collection in the deep ocean. The distribution of particles at depth is linked to surface ocean structures through forward simulations of particle trajectories. To describe the patterns found at depth and relate them to the small- and medium-scale circulation, a popular unsupervised machine learning algorithm (K-Means) is applied to identify clusters of particles seeded from the surface ocean that reach a target area in the deep ocean. Lastly, we investigate the seasonality of particle clusters and relate the forward simulation results to particle sampling in the deep ocean.

4.1 Abstract

A major pathway in the biological carbon pump is the gravitational sinking of organic particles from the sunlit ocean (0-200 m) to the deep ocean. The downward particle flux that reaches the base of the twilight zone (1000 m) or below is typically assessed using sediment traps moored at depth. The trap-based particle flux observations have shown seasonality which is often attributed to the seasonal variability of the primary production in the surface ocean. Nevertheless, the particle flux is also affected by physical processes such as mesoscale eddies and fronts. Here the impacts of upper-ocean dynamical structures on the variability of particle collection in the deep ocean are studied by clustering trajectories of 51.9 million particles that are initially distributed homogeneously in space at 200 m depth and reach a 200 × 200 km target area at 1000 m in the North East Atlantic basin. We identify and characterize nine particle clusters, among which six clusters are related to eddy and frontal structures. The results show that the seasonality of particle collection at depth can be induced by the seasonal variations of upper-ocean flow structures. The eddy/frontal structures predominantly contribute to particle export (>50%) in winter and spring, with smaller second peaks in summer months. The local background flow cluster with up to 70% particles takes over in autumn. We also found that despite a homogeneous source of particles without biological impacts, the ocean dynamics can still induce a spatial gradient of particle collection over 200 km at depths. Finally, this study suggests the position of sediment traps makes a large difference in weekly to seasonal particle collections in the deep ocean.

4.2 Introduction

Among the several distinct pathways of carbon transfer from the surface ocean to the deep ocean, the gravitational settling of organic particles is estimated to account for 70% of the total global carbon export (Nowicki et al., 2022). The delivery of particulate organic carbon (POC) to the deep ocean has been investigated using deep-moored sediment traps since the late 1970s. A key finding of moored sediment trap studies was the seasonality in the particle flux to the deep ocean. The seasonality has been generally attributed to the seasonal change of the primary production in the surface ocean with peaks in early spring and lows in late autumn (Deuser and Ross, 1980; Deuser et al., 1981; Honjo, 1982), despite interannual variability in the timing, duration and magnitude of the seasonal peak flux (Conte et al., 2001). The particle flux recorded at a given site and depth depends on a combination of biological, biogeochemical and physical processes varying temporally and spatially.

Previous studies suggest that the spatial heterogeneity of carbon export is driven by the biogeochemical differences (e.g. phytoplankton biomass, nutrient supply) between different flow structures at fronts, eddy cores and edges. The spatial heterogeneity of biological distributions in the ocean is obvious from the remote sensing of ocean color (Mahadevan, 2016). The biological patchiness mostly results from patterned circulation like frontal systems, mesoscale variability, and coastal upwelling. Mesoscale eddies are known to have a fundamental impact on the transport of material and dynamic quantities in the global oceans. Horizontal stirring associated with eddies and filaments is found to structure the spatiotemporal organizations of the phytoplankton community into (sub-)mesoscale patches (10-100 km) of dominant types (d'Ovidio et al., 2010). A set of direct observations has shown particle flux events associated with eddy-eddy fronts (Guidi et al., 2012), the edges of a cyclonic mesoscale eddy (Estapa et al., 2019), and cyclonic eddies at different evolutionary stages (Zhou et al., 2020). The carbon export within a cyclonic eddy was found 2 to 3 times higher than that measured in adjacent ambient waters in the Lee of Hawaii (Bidigare et al., 2003). Despite low upper-ocean carbon export observed in eddies in the oligotrophic North Atlantic Ocean, low oxygen concentrations in deep waters (1000 m) suggested higher POC flux events prior to the sampling (Buesseler et al., 2008). As such, the carbon export in an energetic eddy field is sensitive to the spatial variability of the mesoscale activity.

From a physical perspective, the sinking particles are prone to hydrodynamic effects. Sediment traps sample particles originating from as far as hundreds of kilometers away, continuously over a long period. A collection of studies on statistical funnels of sediment traps illustrate the variability of particle source area due to horizontal advection (Siegel et al., 1990; Siegel and Deuser, 1997; Waniek et al., 2000; Siegel et al., 2008; Wang et al., 2022). The local presence of eddies is episodic and can impact the high-frequency variability of the carbon fluxes induced by hydrodynamical processes. This mesoscale activity may also be responsible for regional differences between particle trapping zones throughout the long-term observations. Advective processes modify the spatial pattern of the transmission of surface signals to the deep ocean most of the time. Hence the lateral transport of particles from productive areas may dominate over the local surface production signals. In this case, seasonal and interannual variability of particle flux is partly controlled by physical processes rather than local signatures of primary production in the overlying euphotic zone (Waniek et al., 2005).

The temporal variations of particle flux are directly related to the temporal variability of primary production. It has been suggested that predictions of particle export flux can be derived from phytoplankton biomass and net primary production estimated based on satellite observations combined with food-web models (Siegel et al., 2014). However, the export flux was found to be decoupled from net primary production at the mesoscale due to the displacement of export in time and space, particularly in spring when the dynamics of fronts and eddies are more active (Mcgillicuddy et al., 2019). Guidi et al. (2007) suggests the importance of temporal changes for the export of surface production to the mesopelagic layer. The indicator of mesoscale activity, eddy kinetic energy, is highly variable in time, possibly resulting from the wind work (Wunsch, 1998), baroclinic instability affected by local heating/cooling (Qiu et al., 2008), and the seasonal changes in the energy cascade from the submesoscale to the mesoscale (Schubert et al., 2020, 2023). As an important mediator of mesoscale kinetic energy transfer, submesoscale motions are well recognized, with stronger intensity in winter and weaker intensity in summer (Shcherbina et al., 2013; Callies et al., 2015; Rocha et al., 2016), leading to a maximum of mesoscale EKE in late spring and early summer.

The goal of this study is to explore how the temporal and spatial variability of mesoscale dynamics affects the particle distribution at depths, with potential implications for carbon fluxes in the deep ocean. By focusing on physics as a first

step, biological production is not explicitly considered, nor are the interactions between biological and physical processes. In Wang et al. (2022) we used back-tracking particle trajectories to characterize the sources of particles collected by a fixed-position sediment trap and presented the impact of local mesoscale eddies on the particle export. Here, with a different objective focusing on the seasonality and spatial variability of the deep ocean particle collection, we analyze the forward-tracking trajectories of particles initialized homogeneously over a large area in the surface ocean. We use key features of particle trajectories and metrics of along-trajectory flow structures to relate particle collections in the deep ocean to upper-ocean dynamics. Since the heterogeneous dispersion of oceanic materials in space and time is associated with specific flow features, we apply clustering analysis to the particle trajectory data in order to link the main scales of the deep particle distribution to the hydrodynamic properties.

The rest of this chapter is arranged as follows. Section 3 describes the data and the clustering method. The identification of clusters in section 4.1 and typical cluster examples in section 4.2 characterize particle clusters, followed by the seasonality of clusters in section 5. Section 6 provides insights into the spatial and temporal heterogeneity of deep-ocean particle observations. Finally, a summary with conclusions and perspectives for future work is presented in section 7.

4.3 Data and Methods

4.3.1 Preliminary experiments

The implementation of clustering analysis on particle trajectories from 7-year forward simulations is motivated by the patterns shown in two preliminary experiments. In a single release experiment in the winter of 2006, about 250 thousand particles sinking at 50 m d^{-1} were seeded at 2 km horizontal spacing from 1000 $\times$ 1000 km patch at 200 m depth centered on the location of Porcupine Abyssal Plain Sustained Observatory (PAP-SO, 49°N, 16.5°W), a long-term time series site in the Northeast Atlantic Ocean. It is located in a region with weak mean flow and moderate eddy kinetic energy, representative of a substantial fraction of the global ocean (Allen et al., 2013). Yet the mesoscale eddy activity in this region is still considerable, with the frequent formation or propagation of coherent mesoscale vortices. In addition to the consistent monitoring system at the PAP site, several international programs have conducted observations near the site in recent years,

such as the OSMOSIS project (Naveira Garabato et al., 2013) on the role of submesoscale processes in determining upper-ocean dynamics, the EXPORTS project (Siegel et al., 2016) and the APERO project towards a mechanistic understanding of the biological carbon pump.

In the first experiment, the distributions of particle depth spread around the expected depth (based on a 50 m d^{-1} sinking velocity) with a wider PDF for deeper expected depth (Figure 4.1a). The initial situation of particles may have a profound impact on the particle collection in the deep ocean. The depth deviation of particles mapped on particle initial positions (Figure 4.1c-f) shows mesoscale eddy patterns and embedded smaller-scale signatures on the full patch, corresponding to the relative vorticity field at the initial depth (Figure 4.1b) with a stream of eddies crossing from west to east and an intensified frontal area on the northwest. The impact of initial positions is also found in a 3-month continuous seeding experiment during the winter of 2006 (Figure 4.2). The horizontal displacement and travel time anomaly on particle final positions show high spatial heterogeneity. This can be linked to the flow structures where particles were initialized. Particles with shorter travel time (negative Δt around -2) are related to the elongated area far from the PAP site. Distinct travel time anomalies are associated with the presence of eddies within the range of the collection zone, showing variable signs and locations depending on the eddy types.

Based on the preliminary experiments, we hypothesize that the collection of particles in the deep ocean is related to the upper-ocean flow structures where particles are produced. To verify this hypothesis, a large data set of particle trajectories covering a broad flow field and a long period is required to perform clustering analysis.

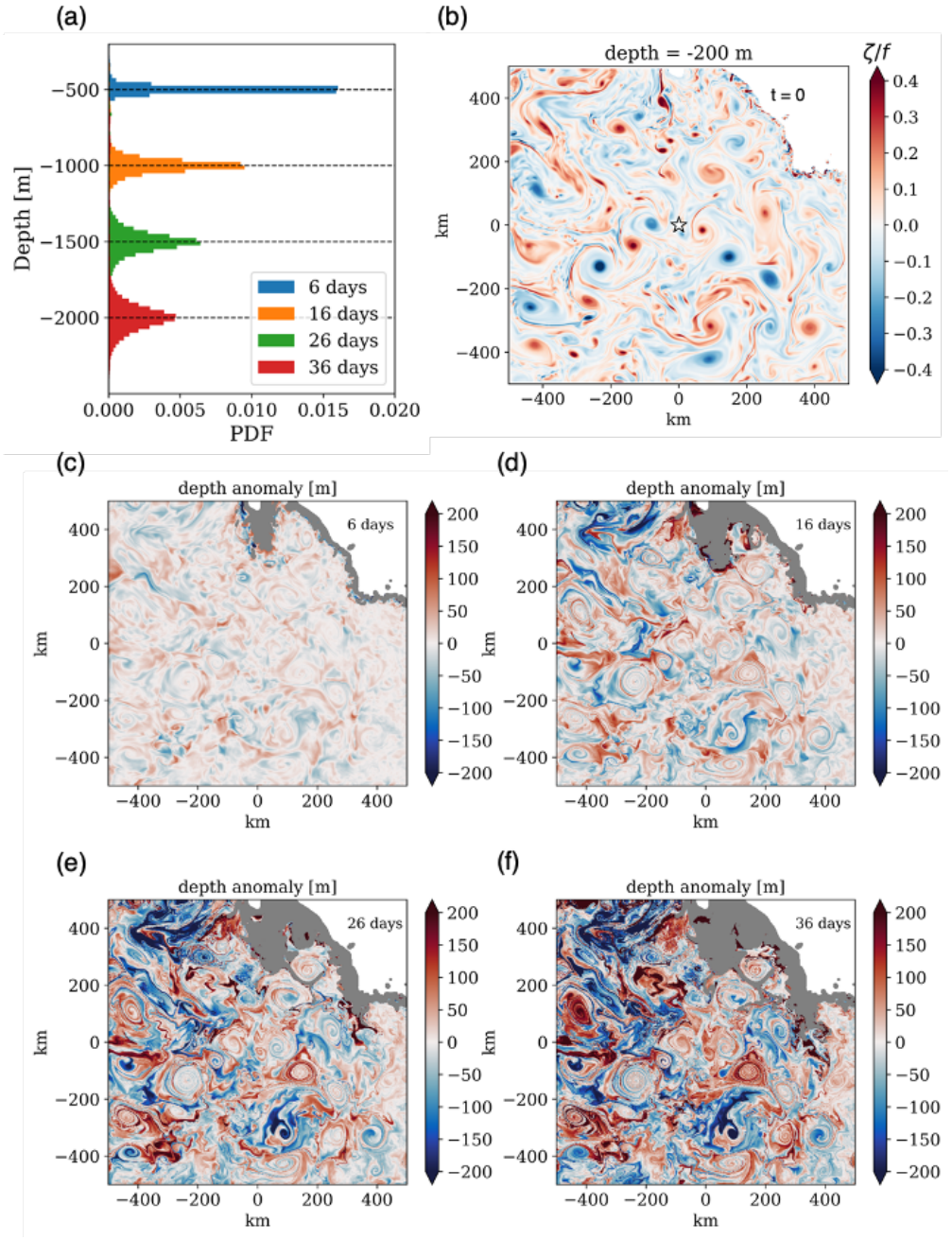

FIGURE 4.1: Distribution of particle depth and depth anomaly in the single release experiment. (a) Probability density function (PDF) of particles as a function of depth after release, corresponding to the expected sinking depth at 500, 1000, 1500 and 2000 m (sinking velocity = 50 m d^{-1}). (b) The relative vorticity field at 200 m depth at the released time (t=0). The star shows the position of the PAP station. (c-f) Particle depth anomaly mapped on the initial position. The depth anomaly is the depth deviation of a particle with respect to its expected sinking depth (= sinking speed × time since release, here 6, 16, 26, 36 days), with positive anomalies in red (i.e., particles are shallower than expected) and negative anomalies in blue (i.e., particles are deeper than expected). The grey shadings mask particles residing in the shallow region due to the topography in the Northeast.

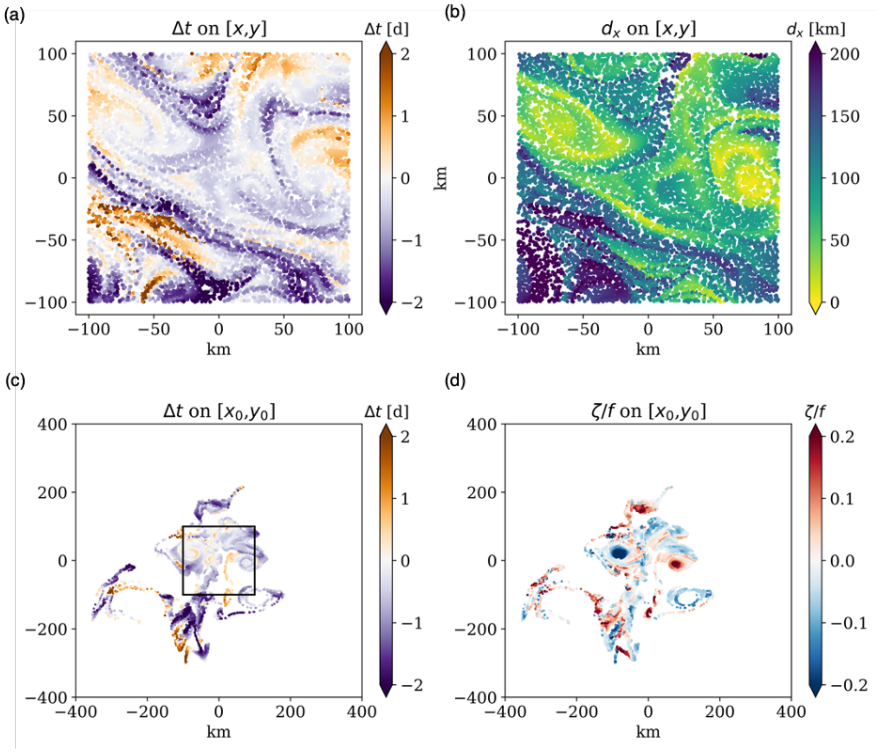

FIGURE 4.2: Particles reaching the 200 × 200 km collection zone at 1000 m, 50 days after a continuous seeding every 12 h from 1000 × 1000 km patch at 200 m depth (sinking velocity = 50 m d^{-1}). (a-b) Travel time anomaly and horizontal displacement mapped on particle final positions. (c-d) Travel time anomaly and relative vorticity mapped on particle initial positions. The black box in (c) marks the area shown in (a) and (b).

4.3.2 Particle trajectory data

Here we use particle trajectories from forward simulations introduced in section 2.2 of Chapter 2. The total number of particle trajectories for clustering analysis is 51,900,650. Particles were initialized at the grid points (horizontal spacing 2 km) on a 1200 × 1200 km seeding patch at 200 m depth centered on the southwest of the PAP site and continuously injected every 12 h for 7 years (2002 - 2008). The size of the seeding patch and its center are determined by the source area of particles backtracked from the border and center of the 200 × 200 km target zone at 2000 m (more details are available in section 2.2.3 of Chapter 2). We focus on particles reaching the 200 × 200 km target zone at 1000 m during the 7 years at the PAP station. Figure 4.3a shows the distribution of particle source locations binned into 10 km × 10 km grids at 200 m depth, with the magnitude of particle number in a grid up to 10^6. The target zone mostly collects particles seeded within

a radius of 500 km of the PAP site, among which most particles originate no more than 200 km from the site, as indicated by the orange area ($> 10^4$ particles in each bin) on the map.

The original trajectory data consists of particle coordinates in three directions, including depth, and velocities. We compute three basic quantities from particle trajectories: the horizontal displacement d_x, the length of particle trajectory $\sum \Delta x$ and the travel time anomaly Δt. The horizontal displacement refers to the horizontal distance between the initial position of particles in the seeding patch at 200 m and the final position of particles in the target zone at 1000 m. The length of trajectory is the integration of the horizontal distance of particle positions over each time step. The travel time anomaly refers to the difference between the particle's travel time and the standard sinking time without the impact of ocean vertical flows. To relate the particle distribution to different flow structures, we also interpolate physical parameters of the Eulerian flow field along particle trajectories. The four physical quantities are the Okubo-Weiss parameter ($OW = \sigma^2 - \zeta^2$), relative vorticity ($\zeta = v_x - u_y$), strain ($\sigma = \sqrt{(u_x - v_y)^2 + (v_x + u_y)^2}$) and divergence ($\delta = u_x + v_y$).

4.3.3 Clustering analysis

4.3.3.1 K-means clustering

Machine learning methods like K-means have been used to map marine ecosystems (Sayre et al., 2017) and assess hydrographic regimes (Hisaki, 2013; Sun et al., 2021; Bernard et al., 2022), based on environmental metrics and ocean current data from in situ observations, satellite data and ocean model outputs. As one of the most commonly used algorithms for clustering, K-means is fast and simple. It is a distance-based unsupervised machine learning algorithm where data points close to each other are grouped into a given number (k) of clusters. K-means scales well to large numbers of samples. It randomly selects one point as the starting cluster center (centroids), and then continuously moves the centroids to the centers of the samples until it reaches the maximum number of iterations. Whenever the centroids move, the algorithm will compute the squared Euclidean distance to measure the similarity between the samples and centroids. However, Euclidean distances tend to become inflated in very high-dimensional spaces. As such, running a dimensionality reduction algorithm such as Principal Component

Analysis (PCA) before K-means clustering can alleviate this problem and speed up the computation.

The input data for K-means clustering includes 11 variables: the three basic parameters of particle trajectory (horizontal displacement, length of particle trajectory and travel time anomaly), and the four physical quantities (Okubo-Weiss parameter, relative vorticity, strain and divergence) at two different depths. For the two depths, we choose the seeding depth (200 m) where the initial condition of particles is determined, and the depth of 500 m, which is a transition depth for different dynamical regimes as illustrated in Wang et al. (2022), so that particle clusters with similar source regions and paths can be identified.

4.3.3.2 Data preprocessing

We applied two data preprocessing techniques to the input data for K-means clustering. The first one is data scaling. The attributes must have the same scale for the machine learning algorithm to consider them all as equal. Here we used a standard scaler by removing the mean and scaling to unit variance to transform all the input variables within the range [-1,1].

PCA was then applied to the scaled input data for dimension reduction and correlation exclusion. Since PCA is sensitive to the numerical scale of data, its performance can be improved by data standardization before PCA. Principle components in PCA are the linear transformations of the original variables. We examined 11 PCs (Figure 4.3b), the same number as the input variables. Only the PCs that explain most of the variance in the data can be retained. According to Kaiser's criterion that all components with eigenvalues greater than 1 should be kept, we retained 6 PCs explaining more variance than a single variable. For a higher total variance to be explained, we finally choose to retain 8 PCs for the following clustering analysis as there is a steep jump from the 8th to the 9th PC in terms of explained variance. In total, they explain approximately 85% of the variance, with each PC accounting for more than 5% of the variance.

4.3.3.3 Choice of the cluster number

The number of clusters k is user-defined. The idea of defining k is to minimize the total variation (or error) within clusters. K-means seeks to iteratively minimize the within-cluster Sum of Squared Errors (SSE) which is often called cluster inertia,

defined as follows:

$$\mathrm{SSE} = \sum_{i=1}^{\mathrm{k}} \sum_{x_j \in \mathbb{C}_i} \left\| \mathbf{y}_\mathrm{j} - \mathbf{c}_\mathrm{i} \right\|^2 \tag{4.1}$$

where y_j is the jth object in cluster C_i, and c_i is the center of cluster C_i. Inertia measures how internally coherent clusters are, hence lower values are better. The Elbow Method calculates the SSE for runs of KMS clustering on the dataset using a range of values of k. The optimal value is chosen when SSE first starts to bend or level off, visible as an "elbow" in the plot of SSE-versus-k. However, this elbow cannot always be unambiguously identified.

The silhouette coefficient is a very useful method to find the number of k when the Elbow point is not shown. It is a measure of how similar a data point is within-cluster (cohesion) compared to other clusters (separation). The silhouette coefficient is calculated using the mean intra-cluster distance and the mean nearest-cluster distance. For a particular data point

$$\mathbf{S}(i) = \frac{b(i) - a(i)}{max\{a(i), b(i)\}} \tag{4.2}$$

where $\mathbf{S}(i)$ is the silhouette coefficient for a particular data point i, $a(i)$ is the average distance between i and all the other data points in the cluster to which i belongs, and $b(i)$ is the average distance between i and all other data points belonging to outside/neighboring clusters. The value of the silhouette coefficient is between [-1,1]. The average silhouette coefficient (SIL) of all data points in the data set is used to assess the quality of clustering. A high value is desirable in the graph of average $\mathbf{S}(i)$ versus k. Ideally, the optimal k value is picked when $\mathbf{S}(i)$ reaches its global maximum. However, the "optimal" cluster number is not always reasonable, which may cause the data structure not fully discovered. Instead, the reasonable cluster number is chosen at a knee point where a smaller peak is located. Here we use the Silhouette Method in combination with the Elbow Method to assess an appropriate value of k for K-means. Figure 4.3c shows the curves of SSE and SIL versus k. We start with $k = 5$ to include basic groups of particles associated with specific components of the flow field: anticyclonic eddy, cyclonic eddy, fronts on the two sides, and the background flow. Unfortunately, there is no obvious elbow for SSE. The highest SIL is at $k = 2$ but with a very large SSE. At $k = 10$, the SSE is much lower colocating with a local peak of SIL. We suppose the optimal cluster number is around 10.

The selection of k value is based not only on the metric assessment but also on the interpretation of the clusters as representative of underlying physical processes that transport particles. Thus, we performed sensitivity tests to validate the choice of k. The number of meaningful clusters started at $k = 5$ and increased up to $k = 9$. K-means clustering with one more cluster at $k = 10$ only generates a subdivision of a frontal cluster compared to the test with 9 clusters. Therefore, the optimal number of clusters is 9 for our data. Figure 4.3d shows the percentage of particles in each cluster. Next, we will characterize these clusters based on the input variables for K-means clustering, and showcase each cluster with examples.

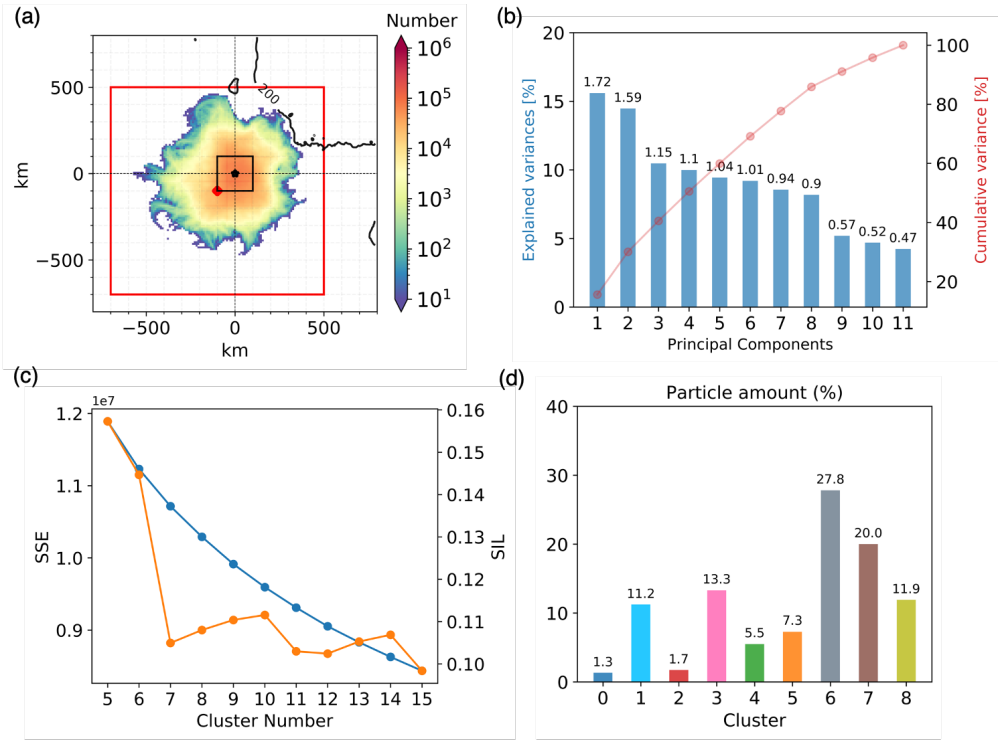

FIGURE 4.3: (a) Source locations of 51.9 million particles in the 7-year simulation, selected for clustering analysis. Particle positions at 200 m depth are binned into 10 km × 10 km grids, the black square is the 200 × 200 km target zone at 1000 m with the PAP site in the center shown as the black star. The red square is the 1200 × 200 km initial patch, the patch center southwest of the PAP site is marked in red. (b) Principle Component Analysis (PCA): variance explained by each PC (blue: individual, red: cumulative), the number on top of the bars are eigenvalues. (c) Two metrics, within-cluster The sum of Squared Errors (SSE) and the average silhouette coefficient (SIL), against the number of clusters k. (d) The percentage of particle amount in each cluster ($k = 9$).

4.4 Characterization of particle clusters

4.4.1 Identify the clusters

The distribution of input variables in each particle cluster shows different features in terms of trajectory and physical quantities (Figure 4.4), which are further used to define particle cluster types and names (summarized in Table 4.1). We identify the first 6 clusters based on the physical quantities at 200 m and 500 m, which reflect the flow structures with which the particle clusters were associated (Figure 4.4e-h). Clusters 0 and 2 have distinctive negative OW at both depths. According to their relative vorticity, they are categorized as anticyclonic vortices (V_{AV}) and cyclonic vortices (V_{CV}), respectively. The structure of anticyclonic vortices may be more stable when extending to deeper depths, as the change of OW and relative vorticity from 200 m to 500 m is smaller for cluster 0 than cluster 2. Cluster 1 and 3 also show large relative vorticity but the OW values are slightly negative only. These two clusters are related to the spiral structure of the anticyclonic (V_{AS}) and cyclonic eddy (V_{CS}), shown by the distribution lying around $\sigma = |\zeta|$ lines in the Joint Probability Density Function (JPDF) of the vorticity-strain (Figures A3 - A4, a brief explanation of the JPDF method is available in Figure A2). Both clusters 4 and 5 show outstanding distribution of the four physical quantities at a certain depth. They are characterized by positive OW, very large strain and large negative divergence at 200 m and 500 m, respectively. From the distribution concentrated in the SD region of JPDFs in Figures A3 - A4, we inferred that particles in the two clusters are associated with frontal structures developing at the surface ocean (F_{200}) and deeper depths (F_{500}). Particles in the last three clusters occupy over 50% of the total particles in clustering analysis (Figure 4.3d). These clusters display common distributions of physical quantities with smaller ranges than the former six clusters, irrelevant to mesoscale structures. As such, these clusters are likely linked to the background flow accounting for a large portion of the ocean. Using the physical parameters only is not adequate to differentiate the three clusters, hence the trajectory parameters (Figure 4.4 a-d) are used to distinguish these three clusters and to further characterize all clusters.

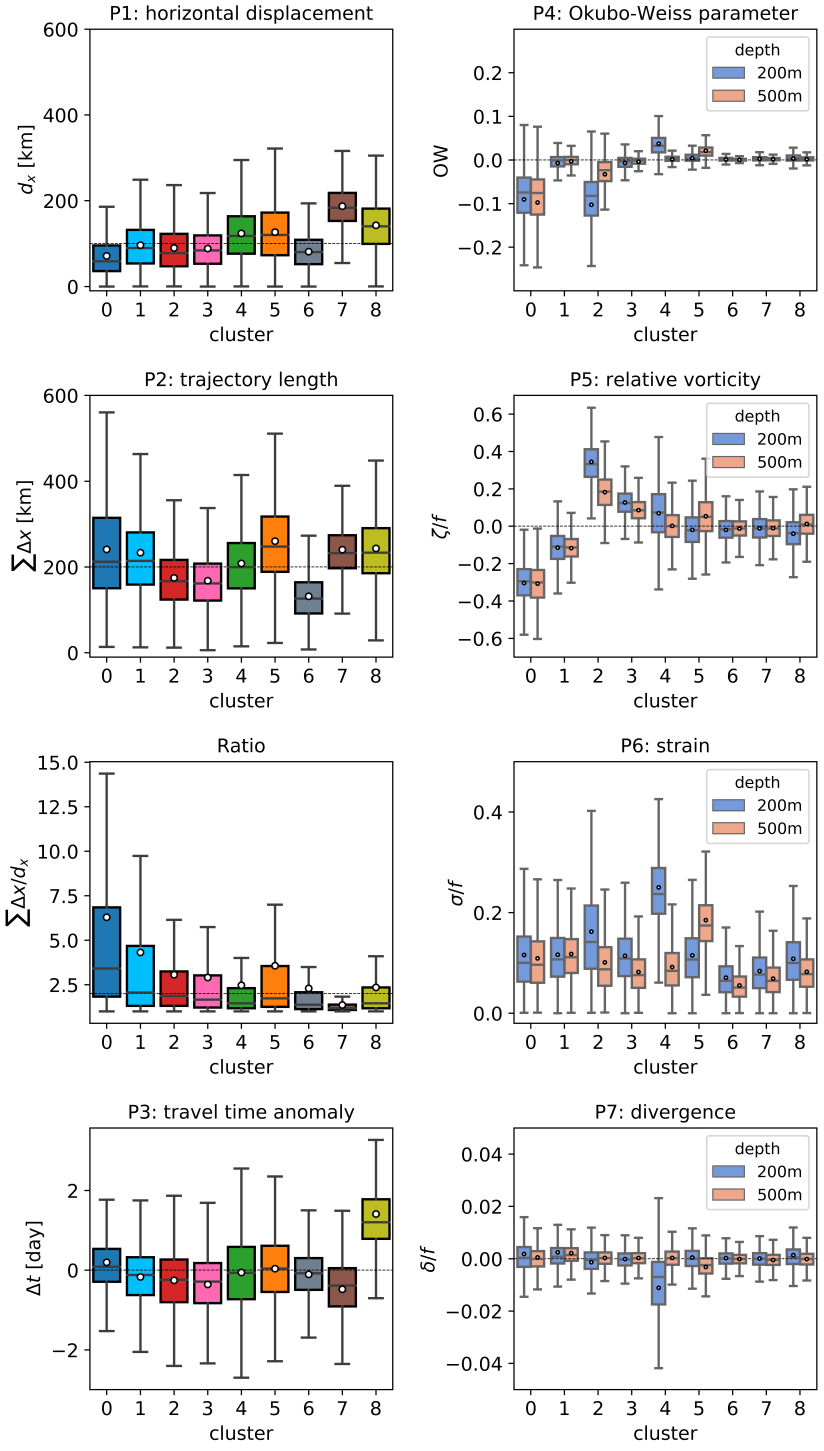

FIGURE 4.4: The distribution of variables (P1-P7 are input variables for K-means clustering except the Ratio $\sum \Delta x/d_x$) for each cluster, showing the mean (white dots), 25%-75% interquartile range (box), minimum and maximum (horizontal bars). (a-d) Particle trajectory quantities. (e-h) Physical quantities at 200 m and 500 m depth.

The four clusters associated with eddy structures have small horizontal displacements with a median and mean of less than 100 km, especially cluster 0 associated with anticyclonic vortices showing approximately 75% particle origins close to the collection point. As expected, the trajectory length of particles in these vortical clusters is much larger than the horizontal displacement (mean Ratio above 3), which means particles swirl in these structures. Interestingly, the anticyclonic vortical structures seem to have stronger trapping effects on sinking particles than their cyclonic counterparts, as indicated by the maps of particle trajectory length showing larger values for clusters 0 and 1 than clusters 2 and 3 (Figure A1). In particular, particles with anticyclonic vortices show the trajectory length is on average 6 times the horizontal displacement. The travel time anomaly of this cluster is also larger with more positive values than the other three clusters (Figure 4.4d), which means the collection of particles at depth is often delayed by the vertical flows. On the contrary, anticyclonic spirals and cyclonic vortices/spirals tend to enhance the vertical sinking of particles. One of the results of backward simulations in Chapter 3 is that anticyclonic eddies accelerate particle sinking in a few cases (most of them are anticyclonic spirals) (Wang et al., 2022). In a broad view supported by the large trajectory data set, our results in these forward simulations here suggest different impacts of anticyclonic eddy structures on sinking particles.

The two clusters related to frontal regions show larger horizontal displacements than the vortical clusters. Particles in the two frontal clusters also have large trajectory lengths comparable to the horizontal displacements (moderate Ratio). Namely, the frontal structures transport particles distant from the collection point compared to more local mesoscale eddies. The last three clusters do not seem to be linked with the mesoscale dynamics as they show common physical parameters without outstanding features. Cluster 6 is the largest cluster with 27.8% particles (Figure 4.3d). Also, its source area where particles are initialized is the smallest (Figure A1), with the smallest horizontal displacement and trajectory length among all clusters. It is much less affected by horizontal advection and as such mostly controlled by the 1D vertical processes, named as "$L_{Vertical}$". This cluster should be in regions where dynamics are very weak, as the range of travel time anomaly of this cluster is the smallest among all clusters. Namely, it is associated with the local background flow meaning that the ocean is "at rest" in this cluster. Clusters 7 and 8 have the first and second largest displacement but with contrasting distributions of travel time anomaly (most negative versus most positive), hereby defined as clusters with fast-moving and slow-moving particles from

remote source regions (R_{Fast} and R_{Slow}). The fast movement of particles in R_{Fast} could be driven by strong horizontal velocities in the veins and filaments of the flow field. The inverse distribution of travel time anomaly in the last two clusters is attributed to the different vertical flows they encountered during the sinking process, but this needs to be further investigated.

Cluster	Characteristics	Type	Name
0	Strongly negative OW, large negative vorticity. Very small horizontal displacement, very large ratio of trajectory length to displacement.	Vortical (Antiyclonic Vortices)	V_{AV}
1	Slightly negative OW, negative vorticity. Large ratio of trajectory length to displacement.	Vortical (Anticyclonic Sprials)	V_{AS}
2	Strongly negative OW, positive vorticity. Small horizontal displacement, trajectory length several times of displacement.	Vortical (Cyclonic Vortices)	V_{CV}
3	Slightly negative OW, positive vorticity. Small horizontal displacement, trajectory length several times of displacement.	Vortical (Cyclonic Sprials)	V_{CS}
4	Positive OW, large strain and large negative divergence at 200 m. Large horizontal displacement, trajectory length several times of displacement.	Frontal (intensified at 200 m)	F_{200}
5	Positive OW, large strain and large negative divergence at 500 m. Large horizontal displacement, large ratio of trajectory length to displacement.	Frontal (intensified at 500 m)	F_{500}
6	Common physical parameters (small OW). Very small horizontal displacement, trajectory length several times of displacement.	Local sources, almost 1D vertical	$L_{Vertical}$
7	Common physical parameters (small OW). Very large horizontal displacement, trajectory length comparable to displacement, strongly negative travel time anomaly.	Remote sources, fast-moving	R_{Fast}
8	Common physical parameters (small OW). Large horizontal displacement, trajectory length several times of displacement, distinct positive travel time anomaly.	Remote sources, slow-moving	R_{Slow}

TABLE 4.1: Descriptive summary of the nine clusters with their distinguishing characteristics shown in the boxplots of variables. Cluster type and name are defined based on the distribution of variables in Figure 4.4 and Figure A1, A3-4.

Lastly, the nine clusters are assessed vertically by the distribution of along-trajectory relative vorticity, Okubo-Weiss parameter (OW), instantaneous horizontal displacement and vertical displacement anomaly in different depth ranges from 200 m to 1000 m. Figure 4.5 shows the median of the four parameters at each depth level, the whole distributions are available in Figures A5-A8). Overall, the vertical features of clusters (Figure 4.5a-b) are consistent with their characteristics shown by the physical parameters at 200 m and 500 m (Figure 4.4e-f). As indicated by the asymmetry towards negative Okubo-Weiss parameter and negative/positive relative vorticity, particles in cluster V_{AV} and V_{CV} are mostly associated with the mesoscale anticyclonic and cyclonic vortices throughout the water column. And

the anticyclonic vortices are more coherent than cyclonic vortices at each depth level, particularly below 600 m where signals of cyclonic vortices weaken. Although the spiral clusters (V_{AS} and V_{CS}) are different from the vortical clusters (V_{AV} and V_{CV}) in terms of physical parameters, they have similar performance in the horizontal transport of particles (Figures A7-A8). On average, the anticyclones move faster than cyclones, whereas the vertical transport of particles in the vortical and spiral clusters is more complicated. In general, particles in clusters V_{AV}, V_{AS} and V_{CV} tend to sink faster than those in cluster V_{AV}, despite depth-dependent variations. The frontal cluster F_{200} shows an asymmetry towards positive OW and positive relative vorticity from 200 m to 400 m (intensified at 200 m), while F_{500} has such a feature from 400 m to 800 m (intensified at 500 m). The instantaneous horizontal displacement of particles in cluster R_{Fast} and R_{Slow} show similar profiles of medians with peaks at around 500 m depth. Their difference in vertical instantaneous displacement is far more distinct than in the horizontal. Particles in the cluster R_{Fast} experience upward vertical velocities below 300 m, strengthening until 700-800 m. Meanwhile, particles in cluster R_{Slow} are largely decelerated at the beginning. The deceleration mitigates until 500 m but intensifies back to the peak at 800-900 m. The profiles suggest that currents below 500 m play an important role in controlling the vertical sinking of particles in these two clusters.

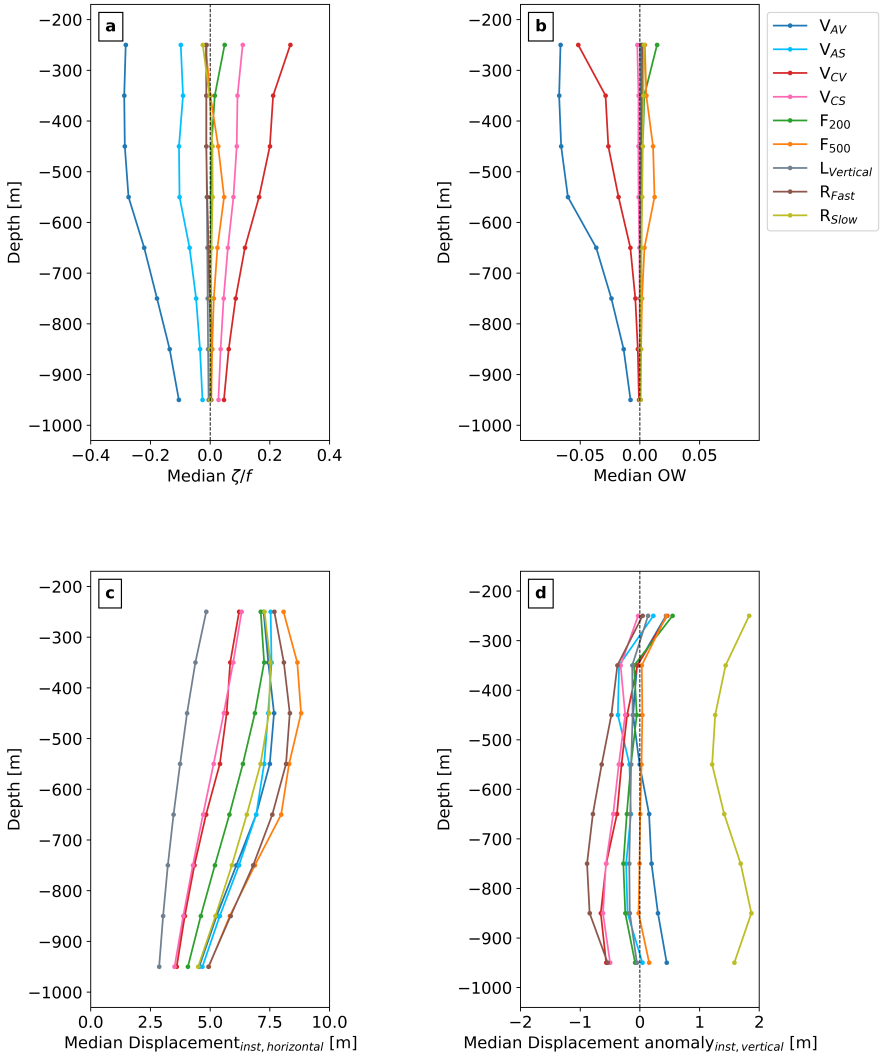

FIGURE 4.5: Medians of (a) relative vorticity, (b) Okubo-Weiss parameter, (c-d) instantaneous horizontal and vertical displacement (anomaly) along particle trajectory in different depth ranges. The vertical displacement anomaly is the difference between particle depth and its expected depth without impacts of vertical flows, with negative (positive) values corresponding to faster (slower) sinking.

4.4.2 Examples of typical clusters

Here we show clustering results for particles released on two different days to visualize the identified clusters. In the first case, taken in winter 2003, the domain is rich in small-scale structures with submesoscale vortices embedded especially northeast of the PAP site (Figure 4.6a). The dominant pattern is a mesoscale cyclonic eddy accompanied by two smaller anticyclonic eddies on its southwest and east sides. Figure 4.6c shows K-means clustering successfully identifies the

cores of the three mesoscale eddies and a suite of small-scale vortices (cluster V_{AV} and V_{CV}). The spirals of anticyclones V_{AS} accounting for 16.9% are also evident, whereas V_{CS} is less obvious with only 5.5% particles in this case. About 30% particles are clustered in the two frontal clusters F_{200} and F_{500} (each $>$ 10%), associated with the main eddies and the area in-between the eddies. Most of these particles are associated with the soup of small-scale structures to the northeast and southwest of the mesoscale eddy pair. It is noticeable that for both clusters, a chain of particles originates from the frontal region between eddies in the middle-west of the domain. As expected, cluster $L_{Vertical}$ has most local particle sources concentrating within the surface ocean upright the target zone or near its edge. The two remaining clusters show similar distributions, while cluster R_{Fast} has a branch of particles originating near the filamentary vorticity streaks in the middle-west.

The second case is in the autumn of 2005 when the flow field has much fewer small-scale structures than the winter case and numerous mesoscale eddies (Figure 4.7a). Although large mesoscale eddies with diameters reaching 100 km are abundant in the flow field, only a limited number of small vortices supply particles as V_{AV} and V_{CV} (1% or less). While particles from the eddy cores show scarce distribution, more particles in the eddy clusters are associated with the spiral structures (8% in V_{AS} and 16.2% in V_{CS}). The frontal structures are also inactive compared to the winter case, with less than 5% particles for each cluster. Since the surface-intensified fronts are mostly generated in winter-spring time (Taylor and Ferrari, 2011; Yu et al., 2019b), cluster F_{200} shows a spotty pattern with 2.3% particles in this autumn case. Cluster F_{500} holds 4% particles predominantly initialized on the periphery of the pair of cyclonic and anticyclonic eddies around the PAP site. The last three clusters contribute nearly 70% particles originating from the areas between eddies, among which R_{Fast} with 41% particles is the dominant cluster and cluster $L_{Vertical}$ with 19.8% particles is another main contributor.

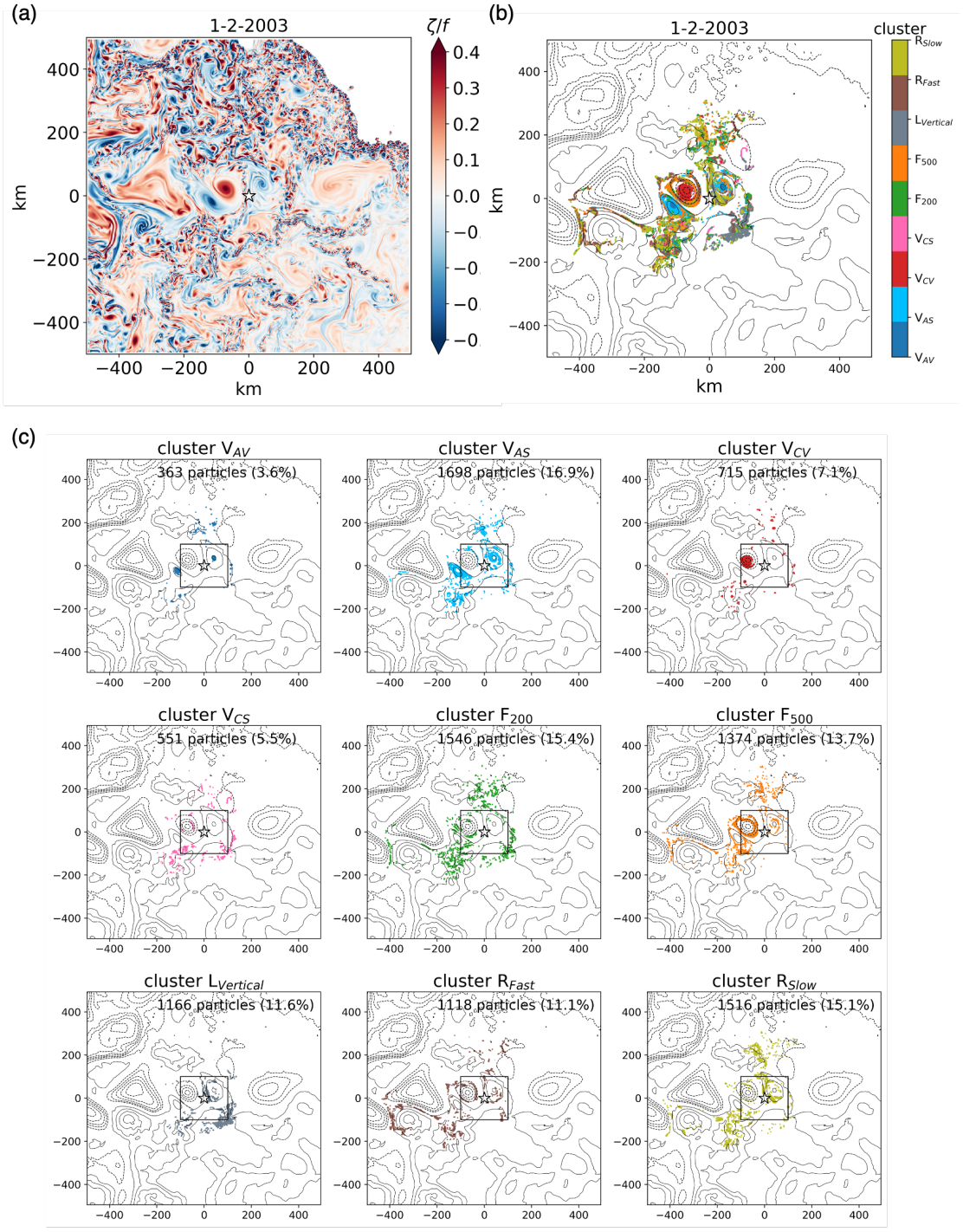

FIGURE 4.6: Clusters identified for particles released on 1 February 2003 reaching the 200 × 200 km target zone. (a) The relative vorticity field at 200 m. (b) The initial positions of particles at 200 m are colored by the clustering results, with Sea Surface Height contours flow structures (solid lines for anticyclones and dashed lines for cyclones). (c) Separate distribution of clusters, with PAP site location (star marker) and the 200 × 200 km target zone (black square). The amount of particles in each cluster and its percentage are shown on top of each map.

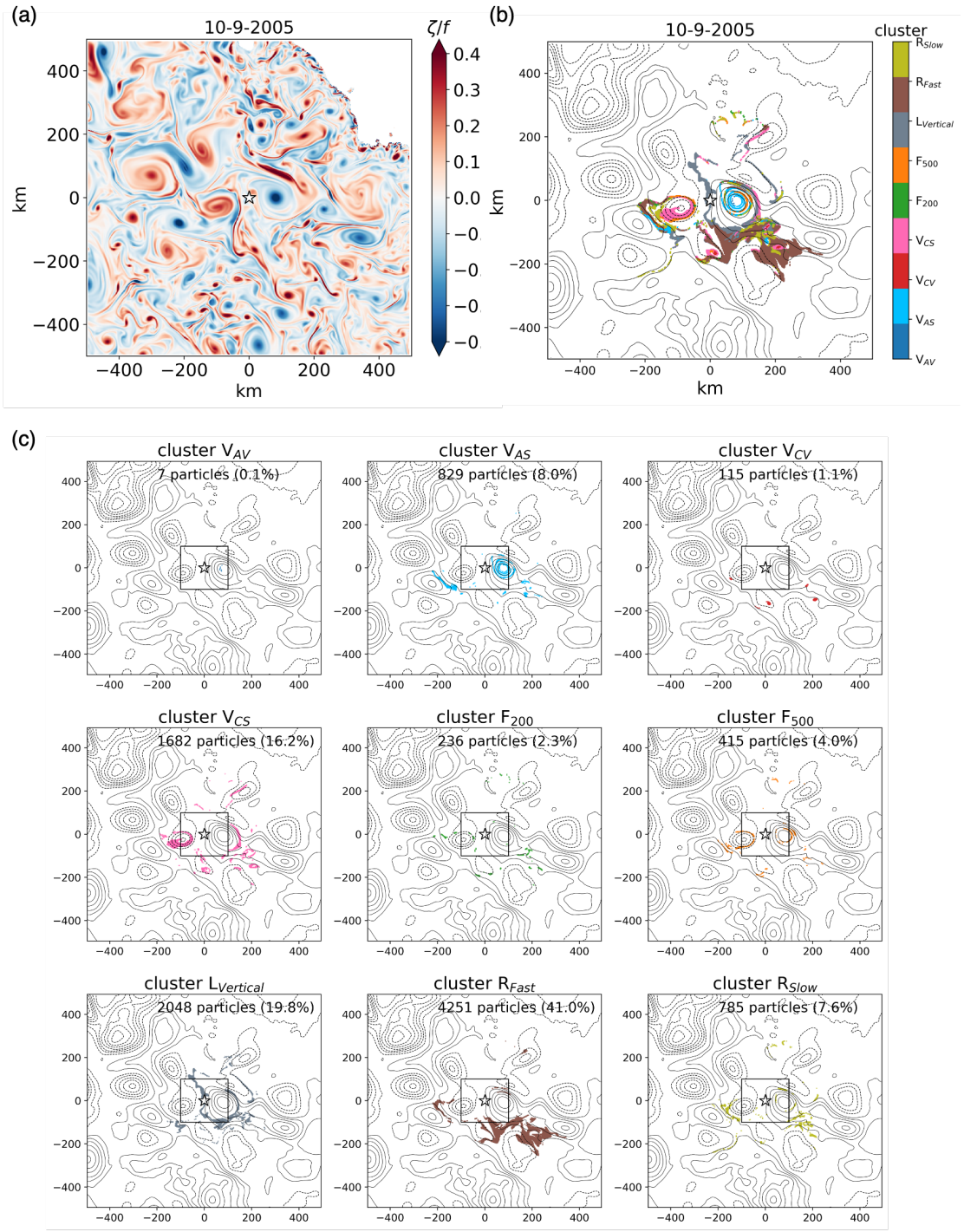

FIGURE 4.7: Similar to Figure 4.6, but for particles released on 10 September 2005 reaching the target zone.

4.5 Seasonality of clusters

To verify the seasonal variability of particle clustering shown by the comparison of two cases in section 4.4.2, the seasonality of clusters is systematically investigated

based on the 7-year simulations. Although the total amount of particles reaching the target zone at each time step remains around 10 thousand with slight fluctuations, particles in different clusters display seasonal variability over the seven years despite interannual differences (Figure 4.8a). As shown in Figure 4.3d, $L_{Vertical}$ and R_{Fast}, which account for almost 50% of the total particles, dominate most of the time, with peaks in autumn or early winter. More particles are identified in other clusters from late winter until the end of summer. The clusters are further divided into four groups for better visualization of their temporal variations.

For the full period, only 3% particles belong to the vortical clusters V_{AV} and V_{CV} (Figure 4.3d). The two comparable eddy-core-related clusters have similar seasonal variations of particle amount in both timing and magnitude (Figure 4.8b). The maximums often occur in late winter or early spring, followed by gradual decreases until reaching second peaks in late summer of some years. After summer peaks, the two clusters remain at low levels for subsequent months when the last three clusters take over ($L_{Vertical}$, R_{Fast}, R_{Slow}). Less than 4% particles are associated with coherent vortices most of the time in spite of some episodic spikes up to 8%.

The timing of peaks and lows of vortical clusters V_{AS} and V_{CS} seems to parallel with the variability of V_{AV} and V_{CV}. However, the spiral clusters V_{AS} and V_{CS} are rather stable, fluctuating around 1000-2000 particles per time step (12h) reaching the target zone. With more than 20% particles contributing considerably to the particle collection in the target zone, the magnitude of their particle numbers is 3-5 times that of the former two clusters. It implies the hydrodynamical characteristics of the spiral structures of mesoscale eddies in this region persistently favor the export of particles throughout the year, whereas the eddy centers only come into play in winter-spring time and episodically in mid-summer. This suggests that the spiral structures in eddies are more important than the eddy cores for particle export. Therefore, sampling the whole eddy structure is necessary rather than the eddy center only. Interestingly, V_{CS} and V_{CV} tend to have more particles than their anticyclonic counterparts, which may be because there is an asymmetry between the areas covered by cyclones versus anticyclones at the time of particle seeding. This is different from the findings that particles preferentially cluster in cyclonic regions due to surface convergence in cyclonic fronts and filaments (Vic et al., 2022).

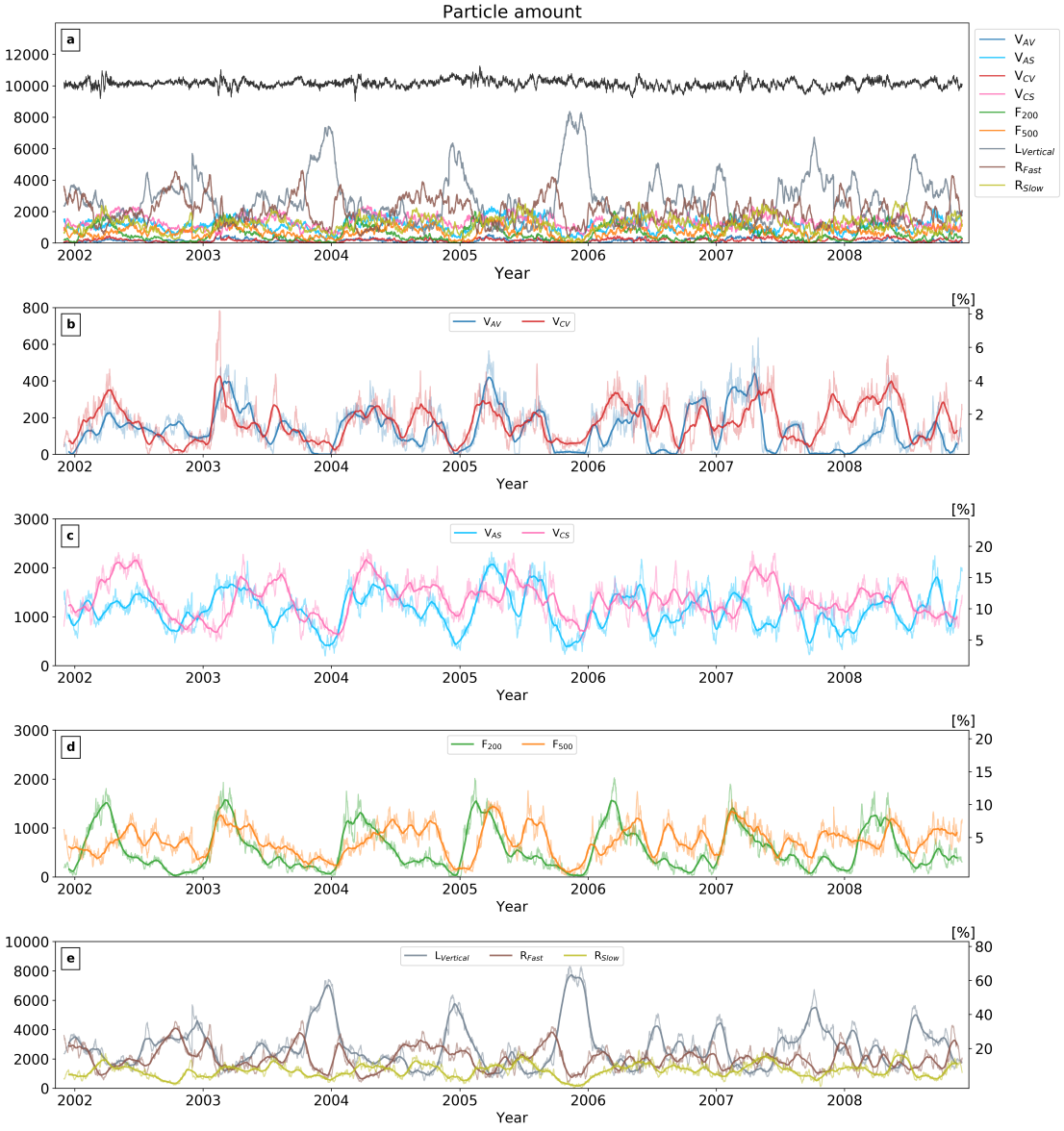

FIGURE 4.8: Time series of particle amount in clusters. (a) At 12h intervals for all clusters, the total amount of particles reaching the target zone is shown as the black thin line on the top. (b-e) Four groups of clusters with adjusted y-axis range, the numbers on the left and the percentages on the right. The thin curves in light colors are the same as in (a) at 12h frequency, and the thick lines are 30-day moving averages based on the thin curves.

The frontal cluster F_{200} shows the most obvious seasonality, with peaks reaching up to 15% in springtime. The timing of peaks varies between years and the two clusters. The apexes of F_{200} come up with similar magnitude in February-April every year, corresponding to the active frontogenesis processes in the upper ocean

(Yu et al., 2019a). The frontal regions are also characterized by enhanced vertical velocities from the sea surface down to hundreds of meters below the mixed layer (Klein and Lapeyre, 2009; Lévy et al., 2012; Mahadevan and Tandon, 2006), as shown in Figure 4.9b with large variations developed from January and intensified until March. F_{200} is larger than F_{500} in winter-spring time but gets much smaller in summer and autumn. The high levels of F_{500} occurring in spring synchronize with F_{200} peaks or show a delay of one or two months. Peaks of F_{500} are also seen in summer-autumn months, which seem to have a potential link to eddy activity indicated by the EKE time series (Figure 4.9a). For instance, the peaks of F_{500} seen in the summer-autumn time from 2004 to 2008 correspond to the deep penetrating large EKE during these months. The cluster maps in Figure 4.6c and Figure 4.7c show particles clustered in F_{500} are initialized at the frontal region at the edge of eddies. Therefore, small-scale and mesoscale eddies as well as fronts are effective hot spots for particle export in winter and spring, while only the mesoscale eddy perimeters are still considerable source regions in summer and autumn.

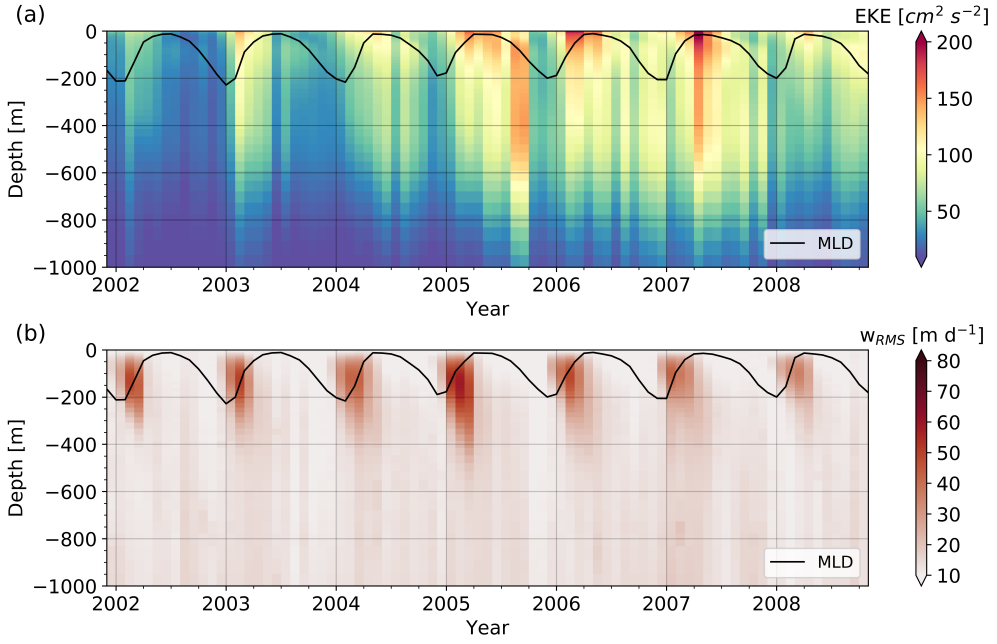

FIGURE 4.9: Time series of (a) Eddy kinetic energy (EKE) and (b) the root-mean-square vertical velocity w_{RMS}, spatially averaged over 200 × 200 km domain. The black curve indicates the MLD.

Overall the last three clusters hold 59.7% particles. It is interesting to note that cluster $L_{Vertical}$ with negligible impacts of dynamics in both horizontal and vertical directions is the largest one among the nine clusters we identified. Particle clustering in $L_{Vertical}$ can account for 40-70% in November-January, which suggests

that most of the particles collected in the deep ocean are locally exported over tens of kilometers by the background flow. The transport of particles from remote sources represented by R_{Fast} and R_{Slow} does not show clear seasonality. Each of them can contribute up to 20-30% for several months every year, which could be further examined in terms of mesoscale activity and large-scale dynamics.

4.6 Spatial and temporal variability of deep-ocean particle collections

This section focuses on the spatial and temporal variability of particle collections in the deep ocean, which may provide insights into deep-ocean observations of particulate organic carbon. The integrated 7-year particle collection in the 200 × 200 km target zone shows large-scale heterogeneity of particle amount (Figure 4.10a-b). There is a north-south gradient on the particle distribution map at 1000 m, although in total the south region collects 1% particles more than the north part (Table A1). The pattern suggests the ocean dynamics by itself can induce a 10% meridional gradient of particles collected at depths over 200 km, despite a homogeneous source of particles without consideration of biological sources. The southern part of the target zone receives more particles than the northern half, and the PAP site is located near the edge of the higher concentration region. The positive South-North gradient is mainly dominated by cluster R_{Fast}, while most of the vortical and frontal clusters (apart from V_{CS}) as well as $L_{Vertical}$ contribute a bit more to the northern region. In the winter case, shown in Figure 4.6a, the northern half of the domain is rich in eddies and small-scale structures compared to the south half. Nevertheless, the north and south regions have no significant difference in the flow field at 200 m in autumn (Figure 4.7a). Such seasonal variability could induce short-term negative gradient and long-term positive gradient from the South to the North.

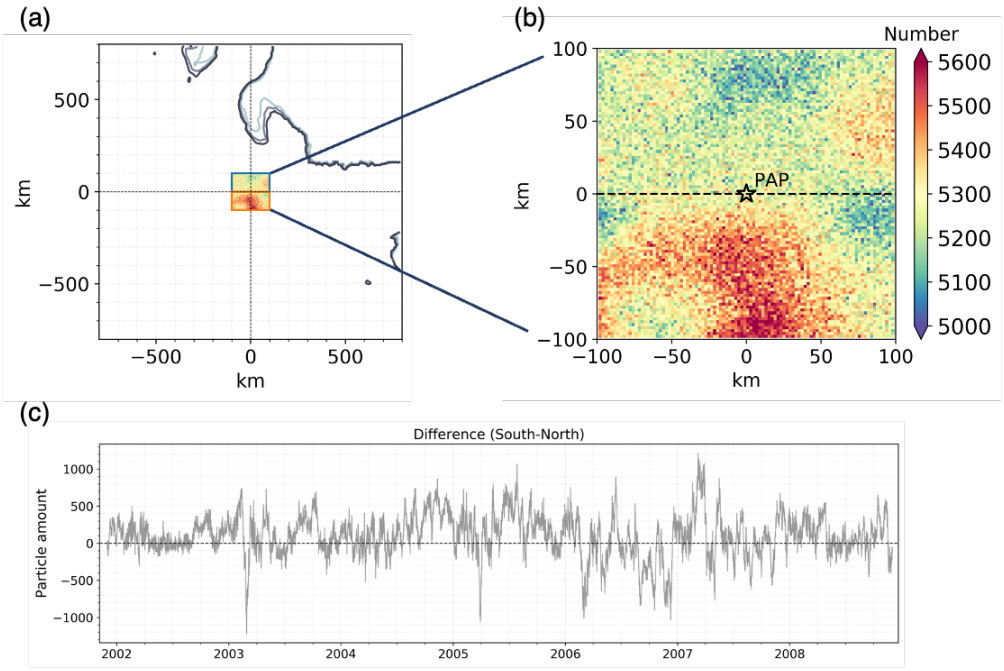

FIGURE 4.10: (a) Distribution of particle collection in the target zone at 1000 m, binned into 2 km × 2 km grids. The blue and orange boxes separate the target zone into the north and south parts. (b) A zoom-in map. The star in the center marks the PAP site location.

In the 7-year time series, the South-North difference of the total particle amount shows large peaks of positive differences most of the time, and negative differences for some periods (Figure 4.10c). The variation of signals is likely due to large-scale circulation or time integration of eddy patterns in this region, which could be associated with the South-North differences in specific clusters. In Figure 4.11, the time series of total particle amounts in the two regions reveals interannual variations but no seasonal signals. The spatiotemporal difference in mesoscale activity of the two regions is reflected by intermittent peaks of the four eddy-induced clusters for the two regions, yet these peaks cannot balance the negative South-North difference caused by the two large clusters $L_{Vertical}$ and R_{Fast}. The frontal cluster F_{200} displays negligible regional difference, while the discrepancy in F_{500} on occasion suggests this cluster is also affected by the eddy activities.

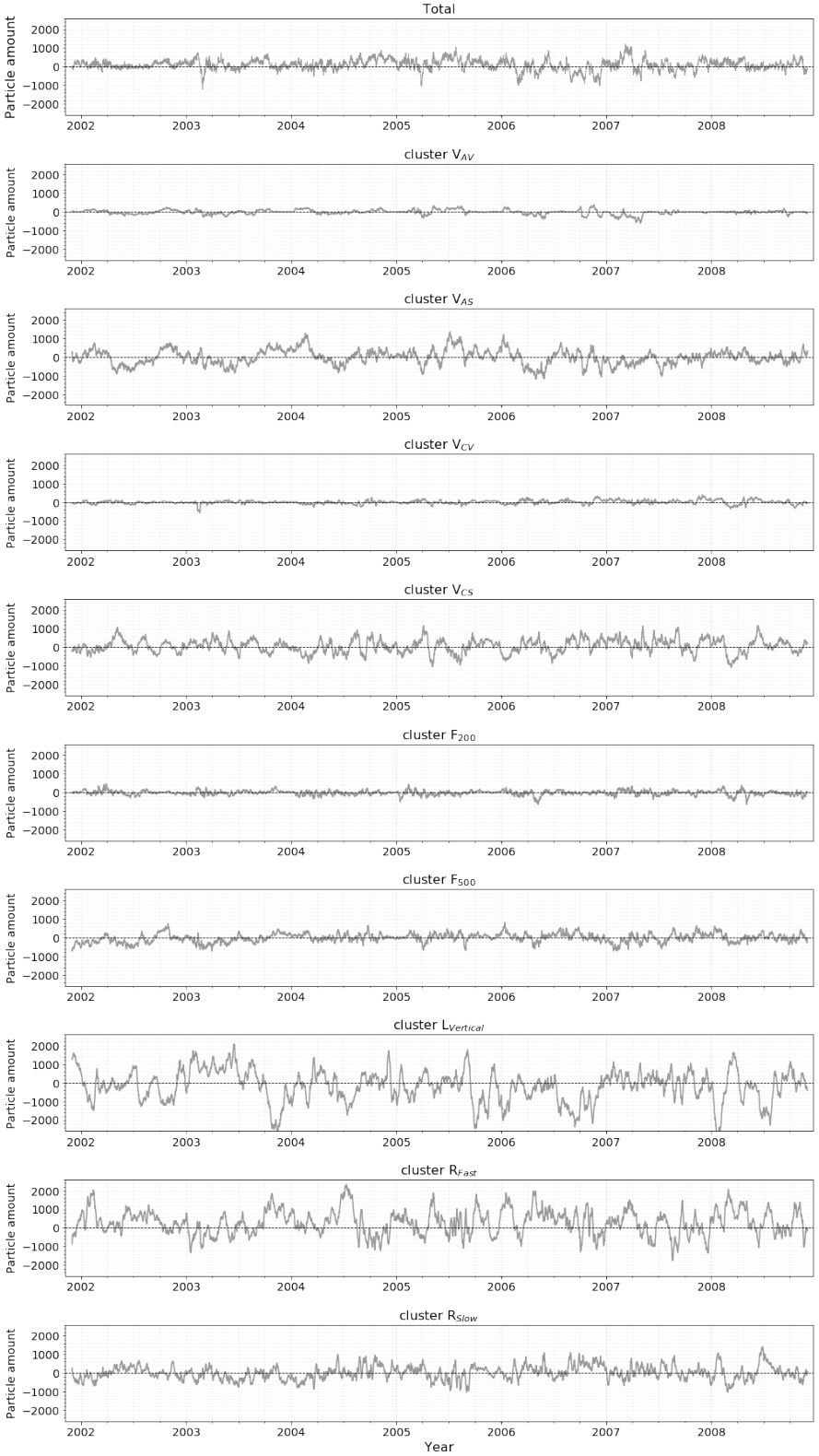

FIGURE 4.11: The difference of particle amounts in the south and north region for the total and each cluster (the positive value means more particles in the south).

When using particle fluxes measured by sediment traps in the deep ocean to assess the biological carbon pump, flux analysis is often performed over a longer time scale like several months or one year. However, the sampling time scale of sediment traps is about one week to one month. The limited size of sediment traps makes it impossible to cover the sampling of particles reaching a large area in the deep ocean. Therefore, it is necessary to know if the location of a sediment trap and the sampling time affect the measurements. As a first attempt, we compare patterns of the particle collection in the target zone over different periods (Figure 4.12). The annual map of particle distribution, travel time, and travel distance are more homogeneous. Hot spots of particle collection and stronger gradients of particle parameters increase towards a shorter time scale. For the annual analysis, the spatial variability of particles induced by trap locations can amount to 10%. Over the shorter period, even in a seasonal analysis, the measurements of particle flux may be biased by the trap locations and sampling time. Local mesoscale eddies lasting for months in the upper ocean can significantly shape the spatial pattern of particles reaching the deep ocean. The eddy imprints shown by the horizontal displacement and trajectory length in the weekly and monthly create largely different sampling areas in the collection zone. In this case, it is possible to sample particles from two distinct source areas within a small spatial range where gradients of these parameters are large. Therefore, the use of an array of sediment traps or moving sediment traps may be necessary for more accurate sampling of particle collection in the deep ocean.

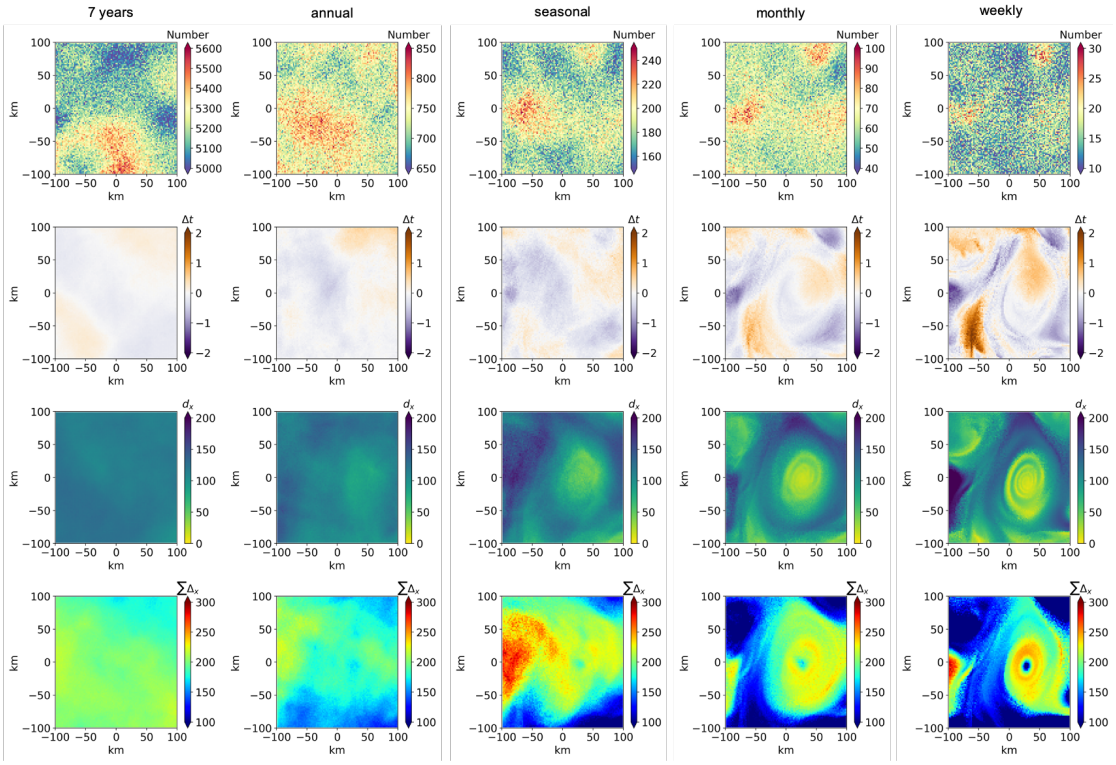

FIGURE 4.12: Particle collection in the target zone over different lengths of periods. From top to bottom: particle distribution, travel time anomaly, horizontal displacement, and trajectory length binned in 2 × 2 km grids on the final location of particles in the target zone for different time scales (from left to right). The annual, seasonal, monthly and weekly plots are for a specific year, season, month and week.

4.7 Conclusions

The deep-ocean collection of sinking particles is connected with signatures of surface ocean dynamics through the forward simulation of particle trajectories over 7 years in an open-ocean region centered on the PAP site in the Northeast Atlantic Ocean. The use of K-means clustering on particle trajectory data successfully identifies 9 clusters of particles seeded from the surface ocean finally reaching a 200 * 200 km target area at 1000 m depth. These particle clusters are related to different dynamical structures, including eddies, fronts and background flows.

The clustering results and characteristics of different particle clusters reveal the role different flow structures play in particle distribution at depth. Although cyclonic eddies contribute a bit more particles to the deep-ocean target area (2.5% of the total amount), anticyclonic eddies are found to be more coherent than

cyclonic ones, with stronger trapping effects on sinking particles. Also, the eddy cores (referred to as "vortices") and eddy perimeters (referred to as "spirals") have different impacts on particle export in terms of particle amount and vertical sinking. More particles are associated with spiral structures than vortices, which means the spirals are more important than the eddy cores for particle export. In the vertical, anticyclonic spirals and cyclonic vortices/spirals tend to accelerate particle sinking, while anticyclonic vortices tend to slow down particles. The frontal structures come into play at the initial seeding depth of 200 m but also at 500 m, close to the permanent thermocline in this region (Callies et al., 2020) where the deep fronts or filaments develop due to baroclinic instability. A key finding is that the particle clusters display distinct seasonality related to the mesoscale eddy activities and the development of fronts. All the eddy and frontal clusters are active in winter-spring time, and the spirals and deep fronts can also considerably contribute in summer. In autumn, the dominant clusters are those irrelevant to mesoscale dynamics, among which the local background flow is in the leading order.

Using a machine learning method on a large data set of forward particle trajectories enables us to statistically characterize the eddy field to specify the contribution of different circulation features to particle exports. The impacts of different eddy structures on particle sinking in part agree with the findings in Chapter 3, as in the backward simulations we can only identify a few typical cases of eddy presence which may not represent more general conditions. The analysis of particle distribution in the deep ocean is also different from the spot-like particle collection in backward simulations with limited particle trajectories. In this way, we investigate the spatial and temporal variability of deep-ocean particle collections. The spatiotemporal difference in mesoscale activity affects the short-term particle collection in different regions at depth, though over long-term (several years) the regional difference is negligible despite a 10% meridional gradient of particle amount in our target zone. Lastly, a comparison of particle collection over different periods suggests that for particle flux measurements lasting from a week to several months, the sampling differs a lot depending on the location of sediment traps. This finding points to the need for mooring arrays of sediment traps or autonomous moving traps in the deep ocean and raises the comparison of Lagrangian versus Eulerian sampling strategy.

This study shows that ocean dynamics can induce distinct spatial variability and

seasonal changes in deep-ocean particle collection without the heterogeneity of biological sources. This first approach has several limitations and could be improved. For instance, testing other clustering algorithms and increasing input parameters may make the clustering results more precise. Also, the availability of particle trajectory data obtained from higher-resolution circulation simulations will better simulate and take into account scales associated with submesoscale eddies and fronts (Balwada et al., 2021) and therefore assess more accurately their impact on the variability of particle distributions at depth. Furthermore, our study considers the variability of physical dynamics only. As this exercise can be done with different sinking velocities to represent a range of particle sizes, the initial seeding of particles can be weighted by using satellite data (ocean color) or physical-biological modeling outputs which provide information about the intensity of the Primary Production (PP) or chlorophyll content in the surface ocean. In this case, part of the variability of the biological activity can be added to assess the variability of the export flux at depths. Nevertheless, this approach does not address particle size spectra due to particle transformation in the water column, for which more complex biological processes need to be considered. It still gives information about the impact of initial conditions (position of variable particle sources) in terms of physics and intensity of PP on the particle distribution at depths.

4.8 Appendix

A. Supplementary figures

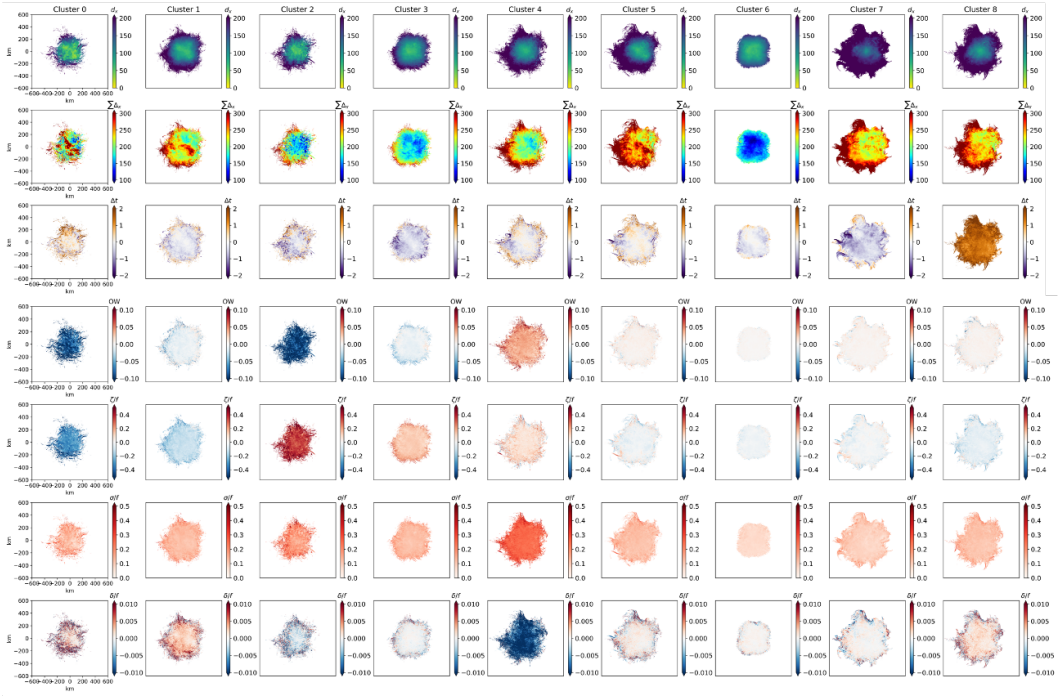

FIGURE A1: Maps of variables on particle initial positions for the 9 clusters (from top to bottom). The variables (from left to right) are horizontal displacement, trajectory length, travel time anomaly, and Okubo-Weiss parameter, relative vorticity, strain and divergence at 200 m.

To link the pattern of particle properties with specific structures, we need to characterize the flow field. Inspired by Balwada et al 2021, we use the vorticity-strain joint PDF to decompose the flow field into regions with different dynamical features. By computing the vertical component of vorticity ($\zeta = v_x - u_y$) and the magnitude of strain ($\sigma = \sqrt{(u_x - v_y)^2 + (v_x + u_y)^2}$), the joint PDF identify three regions separated by the lines of $\sigma = |\zeta|$:

SD – strain dominated $\sigma > |\zeta|$
AVD – anticyclonic vorticity dominated $\sigma < |\zeta|$ and $\zeta < 0$
CVD – cyclonic vorticity dominated $\sigma < |\zeta|$ and $\zeta > 0$

In the middle is the strain-dominated region, and on both sides the vorticity-dominated regions (Figure A2a).

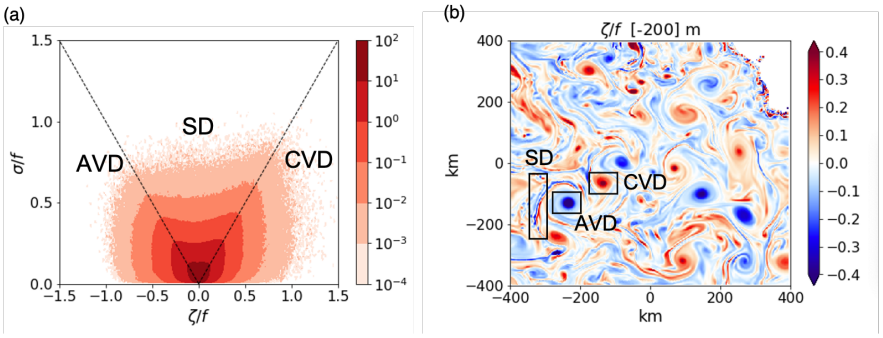

FIGURE A2: Joint Probability Density Function (JPDF) of vorticity and strain. (a) JPDF shows different components of the flow field. (b) The relative vorticity field at 200 m shows the flow field represented by the JPDF in (a). Three types of flow structures are highlighted in the black box.

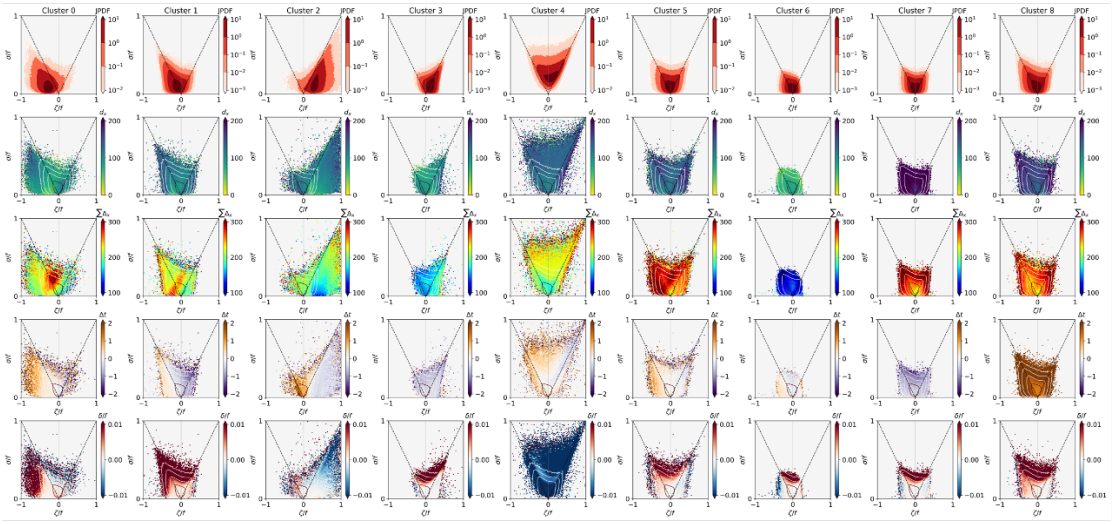

FIGURE A3: Vorticity-strain JPDF at 200 m for the 9 clusters (the top panel, left to right: cluster 0 - 8). The second to the final panel are horizontal displacement, trajectory length, travel time anomaly, and divergence conditioned on the vorticity-strain JPDF.

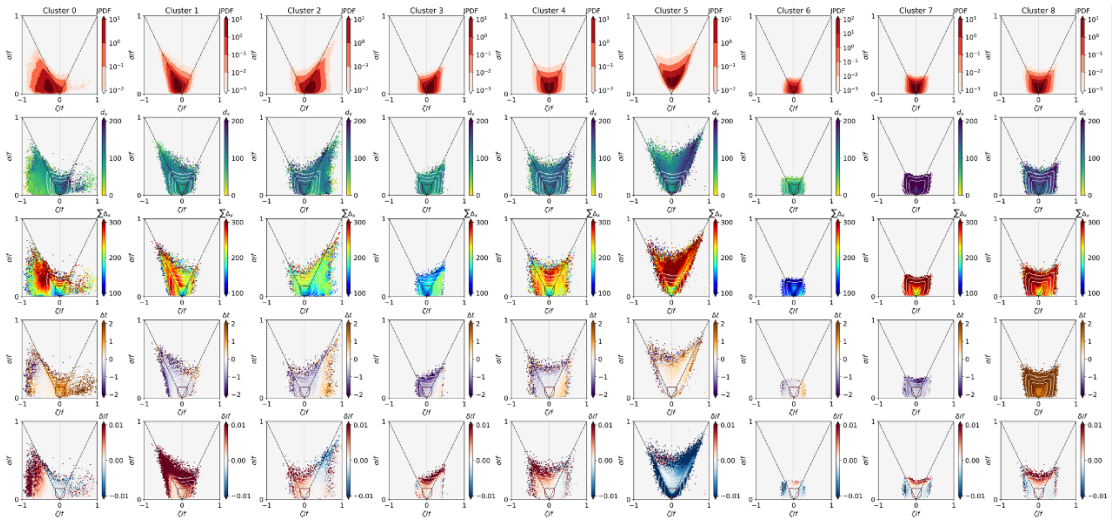

FIGURE A4: Similar to Figure A3, but the vorticity-strain space is at 500 m.

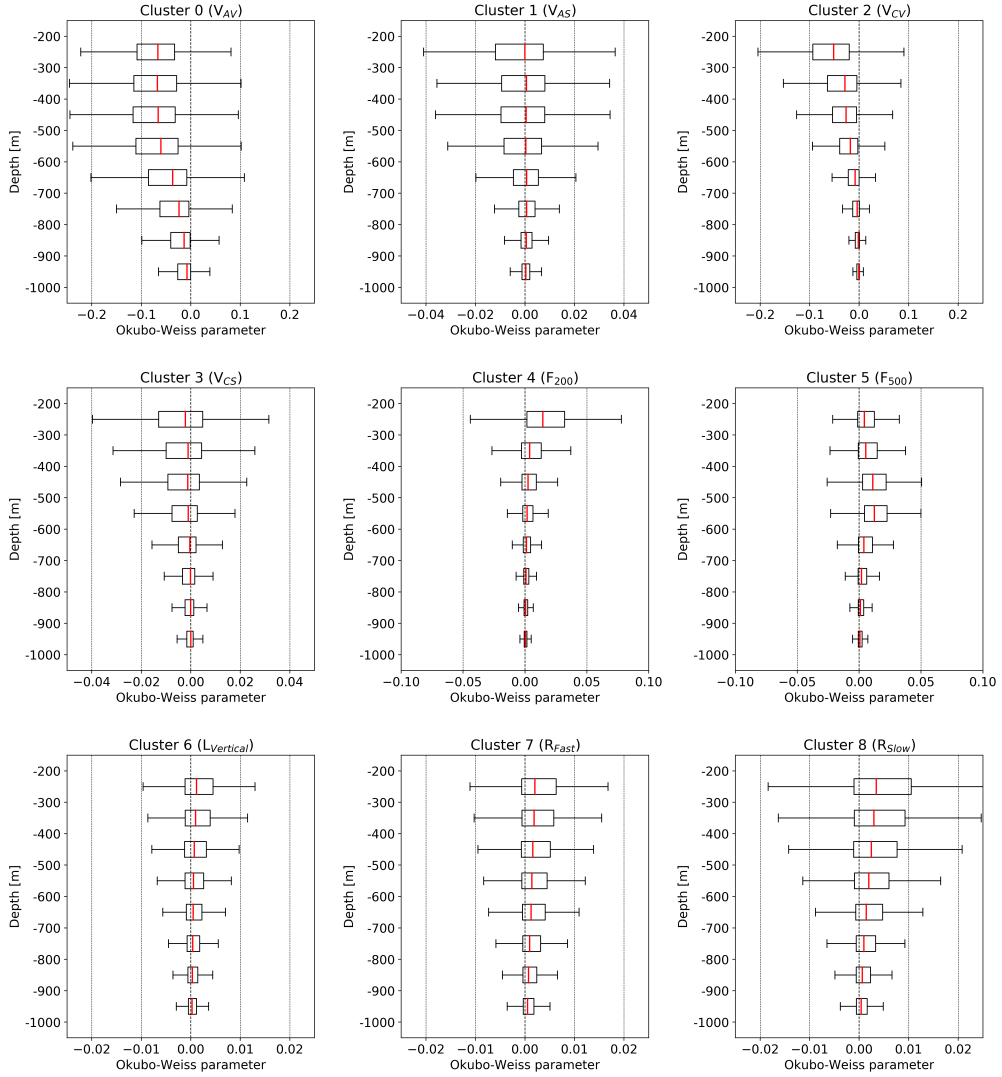

FIGURE A5: Full-period (7 years) Okubo-Weiss parameter along particle trajectory in different depth ranges.

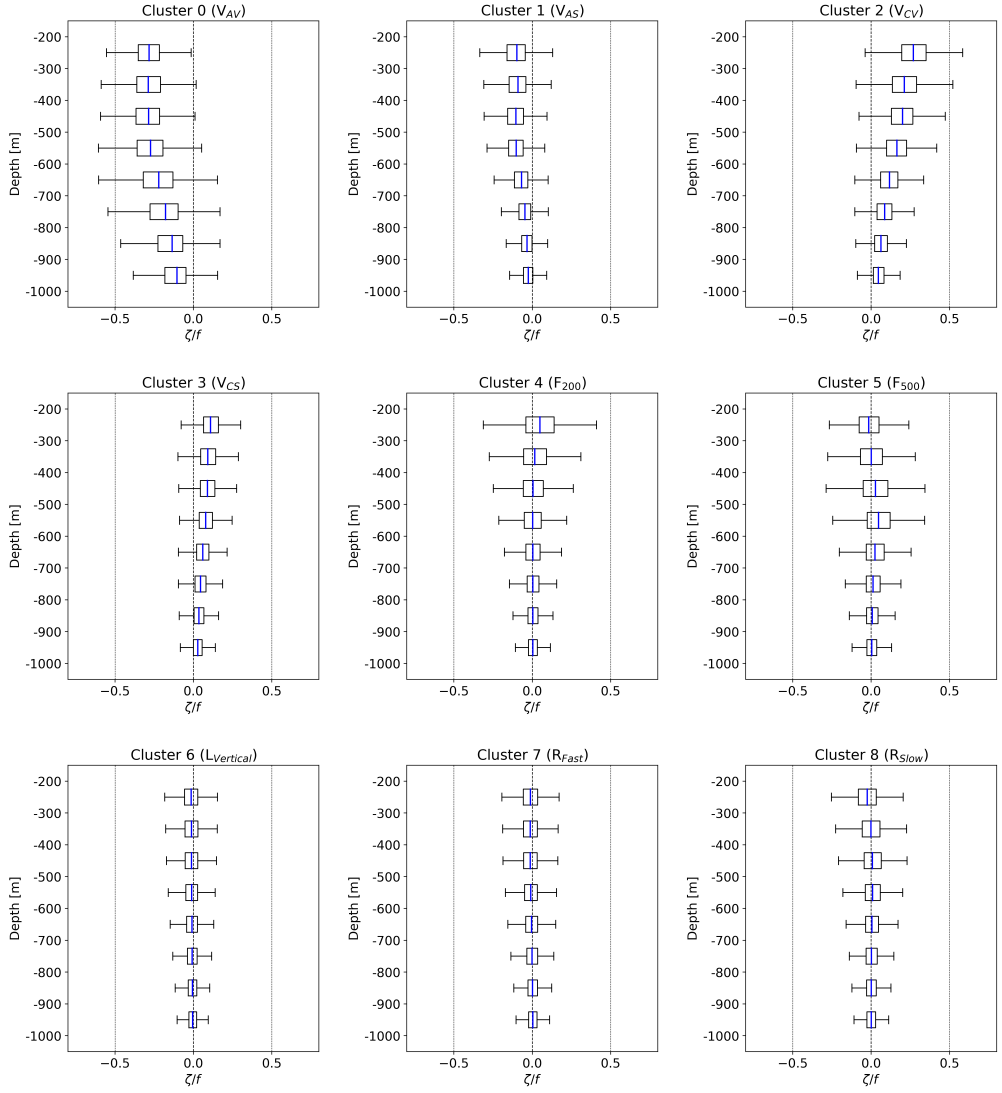

FIGURE A6: Full-period Relative vorticity along particle trajectory in different depth ranges.

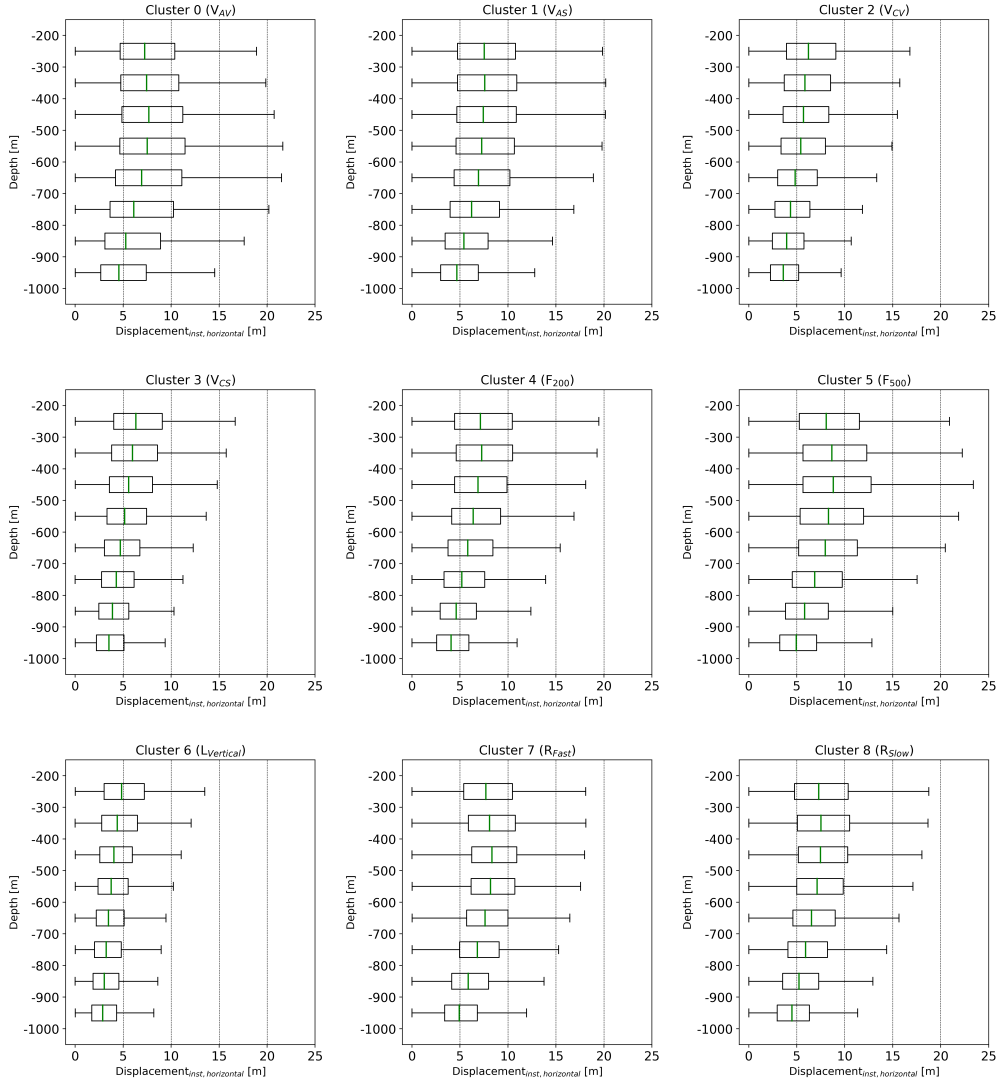

FIGURE A7: Full-period instantaneous horizontal displacement along particle trajectory in different depth ranges.

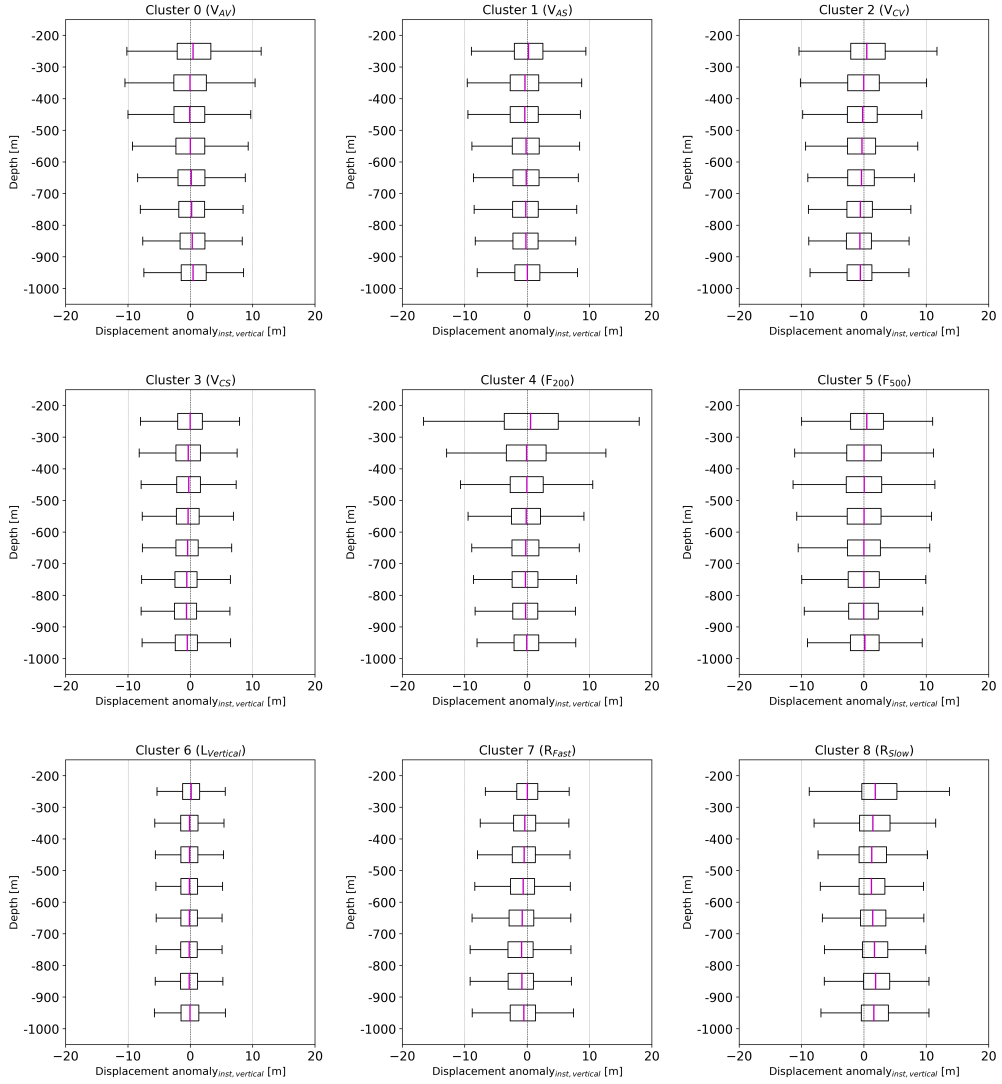

FIGURE A8: Full-period instantaneous vertical displacement anomaly along particle trajectory in different depth ranges.

B. Supplementary table

Cluster	North region	South region
All	25,694,986 (49.5%)	26,205,664 (50.5%)
V_{AV}	385,938 (0.7%)	300,596 (0.6%)
V_{AS}	2,963,691 (5.7%)	2,868,925 (5.5%)
V_{CV}	450,619 (0.9%)	437,549 (0.8%)
V_{CS}	3,273,985 (6.3%)	3,619,941 (7.0%)
F_{200}	1,480,926 (2.9%)	1,360,876 (2.6%)
F_{500}	1,944,688 (3.7%)	1,828,839 (3.5%)
$L_{Vertical}$	7,692,875 (14.8%)	6,730,481 (13.0%)
R_{Fast}	4,450,723 (8.6%)	5,930,655 (11.4%)
R_{Slow}	3,051,541 (5.9%)	3,127,802 (6.0%)

TABLE A1: The number of particles in the North and South region of the target zone: total number and the number in clusters (with percentage).

Chapter 5

Conclusions and Perspectives

This chapter summarizes the key findings of this PhD project by conducting backward and forward particle tracking simulations, which answer the outstanding questions proposed at the beginning of this thesis. Also, the present PhD work offers several perspectives that deserve further investigation in future work.

5.1 Conclusions

The biological carbon pump is an effective route for the ocean to sequester carbon from the atmosphere. Although there are multiple pathways of carbon export from the surface ocean, the carbon storage in the deep ocean (below the mesopelagic layer) is mainly driven by the gravitational settling of particles (Riley et al., 2012). The ocean has a very energetic eddy field that can be seen from space (Mahadevan, 2016), hence the sinking of particles is not only vertical but also partly horizontal. Our study area is in the northeast Atlantic Ocean, centered on the Porcupine Abyssal Plain sustained observatory (PAP-SO) where the deep-sea particulate organic carbon flux has been measured over decades using a sediment trap mooring. This region is characterized by weak mean flow and moderate kinetic energy, but with considerable mesoscale eddy activity dominating the circulation. Also, it has been chosen by a series of observational programs such as OSMOSIS, EXPORTS and APERO, thus the findings of this thesis may have connections with observations and provide suggestions for scientific cruises in the future.

The general framework of this thesis is to estimate the representativeness of observations from the sediment trap mooring at the PAP site and sampling of cruises in this region. At the beginning of this thesis, we proposed three questions targeting: i) the source region of fast-sinking particles collected by deep-ocean sediment traps; ii) the impact of mesoscale dynamics on the transport of particles; iii) the link between the deep collection and surface production of particles through physical dynamics. The main approach is Lagrangian particle tracking in the flow field generated by model outputs. For different objectives, particles were seeded and tracked in two ways, backward and forward in space and time, from the trap and the surface, with completely different experimental designs. The first two questions are answered by backward simulations in Chapter 3, in which particles are backtracked from a fixed location representing a sediment trap. In Chapter 4, which addresses the last question, we constructed a big data set of particle trajectories from the upper ocean to the deep ocean and explored whether the pattern of particle collection in the deep ocean can be related to the dynamics in the surface ocean. In this section, we present the summary of Chapter 3 and Chapter 4, followed by some final remarks regarding the connection of this work with observations and implications for the study of the POC flux.

5.1.1 Summary of Chapter 3

Chapter 3 investigates the impact of mesoscale dynamics on the particles sinking to a deep-moored sediment trap at the PAP site, in terms of the shape of statistical funnels and vertical sinking time, with a focus on the mesopelagic zone (200-1000 m). The statistical funnel describes a dynamical source region consisting of all the likely origins of particles sinking into a sediment trap. We characterize the long-term (7-year) and short-term (monthly) statistical funnels of deep-moored sediment traps for the first time, which differs from previous studies on statistical funnels (Siegel and Deuser, 1997; Waniek et al., 2000; Siegel et al., 2008; Qiu et al., 2014). A diffuse cloud of particle sources formed at the export depth of 200 m is driven by mesoscale eddies which transport particles from distant regions to the PAP site. We found the long-term statistical funnel of particles is far larger, with sampling scales of O(100) km. The size increases with trap depth and decreases with particle sinking velocity, the latter makes a larger difference.

Moreover, the vertical profile of 7-year integrated particle trajectories corresponding to changes in EKE and vertical flows highlights the importance of mesoscale dynamics in the mesopelagic zone in determining the statistical funnels. As such, the water column in this region is divided into three layers with different dynamical regimes, where 500 m and 1000 m are boundaries for the upper energetic layer, the active layer in the middle, and the quiescent layer at the bottom. The division of layers is confirmed by 2D experiments with particles released on the horizontal plane from 200 m down to 4000 m. Note that the structure of the water column may differ in other regions with different dynamical characteristics (e.g., the Gulf Stream).

As a novel approach, we quantified the variability of monthly particle source regions using statistical metrics from LaCasce (2008). In this way, the source distribution of particles is linked to the local mesoscale eddy activity. We identified several typical cases and they suggest that a locally dominant eddy at the site can significantly trap particles within a small region. In the vertical, not only do the vertical velocities in the upper 200 m intensify particle export (Liu et al., 2018), but our results show that the vertical flow below 200 m also tends to accelerate particle sinking to the trap depth, despite large variations seen in spring. We then tried to link the particle export with specific dynamical features using the joint probability distribution function (JPDF) of vorticity and strain. Our selected eddy cases illustrate that particles associated with the anticyclonic eddy are

mostly accelerated by downward velocities in strain-dominated structures, while in the cyclonic eddy, particles are decelerated by upward velocities in the vortex. However, we also pointed out the complexity of vertical velocity patterns in mesoscale eddies driven by various mechanisms. More statistical analysis and deep exploration of the physical mechanisms are required for a comprehensive study of the role of anticyclonic and cyclonic eddies on particle export.

5.1.2 Summary of Chapter 4

Chapter 4 investigates how mesoscale dynamics impact the heterogeneity of particle collection in the deep ocean. The deep collection of particles is connected with surface ocean signatures through the forward simulation of particle trajectories. With a homogeneous initialization of particle sources without considering biological variability, we show the ocean dynamics itself can lead to the seasonal changes and spatial variability of particle collections in the deep ocean.

The use of K-means clustering on particle trajectory data successfully identifies 9 clusters of particles seeded from the surface ocean finally reaching a 200 $\times$ 200 km target area in the deep ocean. The particle clusters occupy quite different proportions in the whole data set. One key finding in this work is the distinct seasonality of particle clusters in terms of particle amounts over the 7-year time series. The seasonal pattern is related to the mesoscale eddy activities and the development of fronts, which are active in winter-spring time and quiet in autumn. More particles are identified in the eddy-related clusters and frontal clusters from late winter until the end of summertime. Among the eddy-related clusters, the vortical clusters are much smaller than the spiral clusters, which suggests that the spiral structures in eddies are more important than the coherent vortices for particle transport. The most obvious seasonality is seen in the frontal clusters, especially the one intensified at 200 m with peaks in springtime, corresponding to the active frontogenesis processes in the surface layer. Interestingly, we found the cluster related to the background flow with negligible impacts of dynamics is the largest cluster, accounting for 40-70% in autumn and early winter when the clusters associated with eddies and fronts are inactive.

There is large-scale heterogeneity of particle amount found in our target zone over the 7 years, induced by the physical dynamics only. The time series variations of particles in each cluster show the spatiotemporal difference in mesoscale activity affects the short-term dynamics of particle collection in different regions. Yet

the local cluster and the cluster being rapidly transported from remote sources dominate over the long term. Additionally, the patterns of particle collection in the target zone over different periods from 1 week to 7 years show hot spots of particle collection and strong spatial gradients of particle properties that increase with shorter sampling scales. An annual integration of particle sampling shows no mesoscale heterogeneity. The heterogeneous spatial pattern of particle properties suggests sampling a broader area using an array of sediment traps, or quasi-Lagrangian drifting sediment traps and autonomous platforms such as BGC Argo floats would be helpful for more accurate measurements of particle collection in the deep ocean. The quasi-Lagrangian drifting instruments can follow the same hydrodynamic patterns as the more stable, "stationary" vortex structures that have so far been the target of biogeochemical studies of the mesoscale carbon cycle.

5.1.3 Final remarks

In this thesis, one of our focuses is on mesoscale eddies, which are ubiquitous in the global ocean (Chelton et al., 2011). The mesoscale eddy field consists of coherent vortices, as well as a rich cascade of other structures such as filaments, squirts and spirals. However, the transient nature of eddies makes them difficult to study. The local patterns may be opposite due to the sampling at different locations during a particular stage of an eddy lifespan (Zhou et al., 2020). The size of the particle data set for analysis in Chapter 4 is enormous compared to the limited number of particles seeded from a tiny patch in Chapter 3. By continuously seeding particles over a large initial patch, we can cover a wide area with various flow structures. Particles finally reaching a confined target zone at depth are subject to further analysis. We statistically characterize the eddy field to specify the contribution of different circulation features to particle exports. Furthermore, the forward simulations allow an analysis of particle distribution in the deep ocean, which is different from the spot-like particle distribution at depth in backward simulations. Interestingly, we found the imprints of local mesoscale eddies on the deep-ocean particle collection in both studies (Figure 5 in Chapter 3 and Figure 12 in Chapter 4). The presence of coherent vortices strongly constrains particles that reach the deep ocean over weeks to months.

As mentioned at the start of this chapter, the study region was selected by the APERO and EXPORTS projects for carrying observations. The outputs of this

thesis underline the presence of coherent mesoscale eddies in effectively "trapping" particles within a local area over a monthly time scale. In this case, the export flux measured in the deep ocean is more correlated to the surface production, which leads to an easier interpretation of *in situ* data during cruises. This finding has implications for the sampling design in a regional survey in this temperate open-ocean region. The location of process study stations can also be identified by focusing on these coherent patterns with the help of satellite observations and modelling outputs. Nevertheless, our study also reveals that these coherent structures are not dominant in the ocean, especially in autumn. Therefore, sampling the continuum between coherent structures and turbulent flows which represent a large portion of the ocean is fundamental and remains challenging.

The dynamical characteristics of our study region make it possible to be representative of the open ocean in a mid-latitude, mid-gyre region. However, our results remain open to be tested in other regions with different situations. It is necessary to verify the generalization of our findings (e.g. the three-layer structure). It could be interesting to extend to the sub-polar or sub-tropical gyre which is in different dynamical and stratification regimes, without too large horizontal advection. Similar analyses could be conducted at other time-series sites, and the region with completely different dynamical features like Western Boundary Currents, Eastern Boundary Upwelling Systems, and the Southern Ocean. In these areas with strong horizontal advection and high energy, the exercise will be more difficult with the impact of strong horizontal currents perhaps being an issue. This modeling approach could be a good way of estimating particle sources in regions with high mean currents, where the export fluxes are not 1D anymore.

5.2 Perspectives

Several simplifications in this thesis lead to some limitations, but also a list of perspectives for further work after the PhD.

5.2.1 Particle dynamics

The constituents of passively sinking particles are complex, mainly including single phytoplankton cells, large and rapidly settling forms after transformation in the water column such as aggregates, and zooplankton fecal pellets. These sinking particles are prone to a variety of processes like remineralization, disaggregation

and repackaging by zooplankton, which changes the composition and amount of particles, and also the particle size, density and settling velocity (Waniek et al., 2005; Boyd and Trull, 2007; Guidi et al., 2007; Riley et al., 2012; Trull et al., 2008).

The variable sinking speed is one of the key factors that potentially affect the spatial pattern of particle transmission from the surface to the deep ocean. The North Atlantic Ocean is a region dominated by large phytoplankton populations (Nowicki et al., 2022). The higher proportion of fast-sinking large POC particles leads to more efficient aggregate formation and export, hence higher export ratios. The range of sinking speeds in this thesis is chosen as representative of common ranges in observations. However, there are still a considerable amount of small particles with much less sinking velocities in the ocean. In our study, the minimum sinking velocity is 20 m day^{-1} which is above the upper limit of the slow-sinking particle class (Riley et al., 2012). We expect a modest impact of remineralization on the fast-sinking classes. But for an analysis of slow-sinking particles, remineralization should be considered even with idealization, like in Dever et al. (2021). So for more complexity, particle sinking velocities could be inconstant. Particle interactions will be considered to affect particle dispersion and size spectra during their sinking. The main purpose is to compare particle distributions at depth to surface patterns, taking into account particle size spectra, behaviors, and interactions. The evolution of individual particles during their sinking, aggregation, disaggregation, and alteration by chemical and biological processes can be tracked by a stochastic Lagrangian model (Jokulsdottir and Archer, 2016).

When moving from fast sinking particles to slow/small sinking particles, the dominant mechanism of BCP will be particle injection pumps mainly driven by advective processes such as physical mixing. This work points to a future study looking into sinking particles affected by remineralization and other processes in the BCP that modify particle sinking velocity. As the small particles are mostly exported below the mixed layer depth rather than much deeper depth, the consideration of the mixed layer dynamics is also necessary (see next subsection).

5.2.2 Impacts of submesoscale dynamics

As an interface between the well-studied epipelagic layer (sunlit zone) and the dark deep ocean, the mesopelagic zone (200-1000 m, or "twilight zone") plays a major role in removing atmospheric CO_2 and storing it in the ocean interior for centuries or longer (Martin et al., 2020). However, the understanding of the

role of this ocean layer in carbon export remains to be improved from physical, biogeochemical, and ecological perspectives. This thesis probes into the role of mid-ocean dynamics in the particle collections by deep-ocean sediment traps. Mesoscale dynamics dominate in the horizontal direction by shaping the statistical funnel of particles. Although we mainly focus on the effects of mesoscale dynamics, we do not leave out associated submesoscale impacts. The model resolution is submesoscale-permitting, and our results suggest there might be submesoscale motions in the upper layer of the twilight zone. In the vertical, we found a skewed travel time of particles, indicating a skewness in the vertical velocity field. There could be a manifestation of finer scales in the model and the potential contribution of submesoscale dynamics, even though there is not much below the mixed layer in our submesoscale-permitting model.

The most important and intensive submesoscale dynamics are in the surface layer, associated with instabilities in the mixed layer. Previous studies have demonstrated the impact of submesoscale dynamics on particle export, including accumulating particles in the surface convergence zones with large vertical velocities (Poje et al., 2014; D'Asaro et al., 2018), restratifying the mixed layer to reduce vertical mixing that inhibits gravitational settling (Taylor et al., 2020), and enhancing the advection of slow-sinking particles (Dever et al., 2021). The impact of submesoscale dynamics in the mixed layer may play a role when its signatures reach below the mixed layer depth. For instance, the vertical transport of nutrients from the subsurface to the ocean surface by submesoscale currents favors primary production (Lévy et al., 2012), which may further enhance the export of large particles.

As such, our future work could be placed in the framework of a higher-resolution model (hundreds of meters), to look more into the impact of submesoscale dynamics (mostly within the mixed layer), and to connect the ocean surface signatures with deep collections of particles in and below the mesopelagic layer.

5.2.3 Physical-biological coupling

The last future direction is a quantitative analysis of the regional surface-deep (de)coupling of particle fluxes taking into account biological variability. Both satellite observations (Zhang et al., 2019) and modelling study (Lévy et al., 2014) have shown the (sub)mesoscale dynamics strongly control the intensity of primary production, which largely constrains particle size spectra: higher production is

generally associated with larger sizes (Kostadinov et al., 2009). Hence this part of work could also incorporate the use of ocean color data from satellite observations, to take into account the heterogeneity of particle sources. The chlorophyll concentration at the ocean surface is an indicator of particle production. We can then perform inhomogeneous particle seeding experiments. By relating the particle size and sinking velocity using Stokes' law as a first approximation, the particle sinking velocity will be weighted by particle size distribution correlated with the primary production intensity at the initialization of particles. This is the first step toward a more realistic and complex representation of the variability of particle sources and of the spatio-temporal heterogeneity of their characteristics in terms of sinking velocity.

The primary production distributions could also be estimated using a physical-biological coupled model system. We will choose a biogeochemical model of appropriate complexity to couple with the circulation model, to quantify the transmission of the downward particulate flux in the (sub)mesoscale field. The biogeochemical model could be a nitrate-phytoplankton-zooplankton-detritus (NPZD) pelagic-ecosystem model. The NPZD model can better constrain the export flux, which could be an improvement over satellites that only measure chlorophyll at the surface and not the export flux below the mixed layer. Such a model has been used to understand the interannual variability of particle flux at 200 m in the northeast Atlantic Ocean (Waniek et al., 2005). This exercise will provide the first information on the eddy-scale variability of carbon fluxes in the deep ocean at a daily resolution.

Bibliography

Allen, J., Naveira-Garabato, A., et al. (2013). Rrs discovery cruise 381, 28 aug-03 oct 2012. ocean surface mixing, ocean submesoscale interaction study (osmosis).

Baker, C. A., Henson, S. A., Cavan, E. L., Giering, S. L., Yool, A., Gehlen, M., Belcher, A., Riley, J. S., Smith, H. E., and Sanders, R. (2017). Slow-sinking particulate organic carbon in the atlantic ocean: Magnitude, flux, and potential controls. *Global Biogeochemical Cycles*, 31(7):1051–1065.

Baker, C. A., Martin, A. P., Yool, A., and Popova, E. (2022). Biological carbon pump sequestration efficiency in the north atlantic: a leaky or a long-term sink? *Global Biogeochemical Cycles*, 36(6):e2021GB007286.

Balwada, D., Xiao, Q., Smith, S., Abernathey, R., and Gray, A. (2021). Vertical fluxes conditioned on vorticity and strain reveal submesoscale ventilation. *Journal of Physical Oceanography*, 51(9):2883–2901.

Bernard, D., Biabiany, E., Cécé, R., Chery, R., and Sekkat, N. (2022). Clustering analysis of the sargassum transport process: application to beaching prediction in the lesser antilles. *Ocean Science*, 18(4):915–935.

Bianchi, D., Stock, C., Galbraith, E. D., and Sarmiento, J. L. (2013). Diel vertical migration: Ecological controls and impacts on the biological pump in a one-dimensional ocean model. *Global Biogeochemical Cycles*, 27(2):478–491.

Bidigare, R. R., Benitez-Nelson, C., Leonard, C. L., Quay, P. D., Parsons, M. L., Foley, D. G., and Seki, M. P. (2003). Influence of a cyclonic eddy on microheterotroph biomass and carbon export in the lee of hawaii. *Geophysical Research Letters*, 30(6).

Boccaletti, G., Ferrari, R., and Fox-Kemper, B. (2007). Mixed Layer Instabilities and Restratification. *Journal of Physical Oceanography*, 37(9):2228–2250.

Boyd, P. and Newton, P. (1995). Evidence of the potential influence of planktonic community structure on the interannual variability of particulate organic carbon flux. *Deep Sea Research Part I: Oceanographic Research Papers*, 42(5):619–639.

Boyd, P. and Trull, T. (2007). Understanding the export of biogenic particles in oceanic waters: Is there consensus? *Progress in Oceanography*, 72(4):276–312.

Boyd, P. W., Claustre, H., Levy, M., Siegel, D. A., and Weber, T. (2019). Multi-faceted particle pumps drive carbon sequestration in the ocean. *Nature*, 568(7752):327–335.

Buckingham, C. E., Naveira Garabato, A. C., Thompson, A. F., Brannigan, L., Lazar, A., Marshall, D. P., George Nurser, A., Damerell, G., Heywood, K. J., and Belcher, S. E. (2016). Seasonality of submesoscale flows in the ocean surface boundary layer. *Geophysical Research Letters*, 43(5):2118–2126.

Buesseler, K. O. and Boyd, P. W. (2009). Shedding light on processes that control particle export and flux attenuation in the twilight zone of the open ocean. *Limnology and Oceanography*, 54(4):1210–1232.

Buesseler, K. O., Lamborg, C., Cai, P., Escoube, R., Johnson, R., Pike, S., Masque, P., McGillicuddy, D., and Verdeny, E. (2008). Particle fluxes associated with mesoscale eddies in the sargasso sea. *Deep Sea Research Part II: Topical Studies in Oceanography*, 55(10-13):1426–1444.

Callies, J., Barkan, R., and Garabato, A. N. (2020). Time scales of submesoscale flow inferred from a mooring array. *Journal of Physical Oceanography*, 50(4):1065–1086.

Callies, J., Ferrari, R., Klymak, J. M., and Gula, J. (2015). Seasonality in submesoscale turbulence. *Nature communications*, 6(1):6862.

Capet, X., McWilliams, J. C., Molemaker, M. J., and Shchepetkin, A. (2008). Mesoscale to submesoscale transition in the california current system. part ii: Frontal processes. *Journal of Physical Oceanography*, 38(1):44–64.

Carton, J. A. and Giese, B. S. (2008). A reanalysis of ocean climate using simple ocean data assimilation (soda). *Monthly weather review*, 136(8):2999–3017.

Chelton, D. B., DeSzoeke, R. A., Schlax, M. G., El Naggar, K., and Siwertz, N. (1998). Geographical variability of the first baroclinic rossby radius of deformation. *Journal of Physical Oceanography*, 28(3):433–460.

Chelton, D. B., Schlax, M. G., and Samelson, R. M. (2011). Global observations of nonlinear mesoscale eddies. *Progress in oceanography*, 91(2):167–216.

Chelton, D. B., Schlax, M. G., Samelson, R. M., and de Szoeke, R. A. (2007). Global observations of large oceanic eddies. *Geophysical Research Letters*, 34(15).

Coatanoan, C. (2021). Mixed layer depth in the north atlantic ocean. product information document (pidoc). https://doi.org/10.13155/79588.

Conte, M. H., Ralph, N., and Ross, E. H. (2001). Seasonal and interannual variability in deep ocean particle fluxes at the oceanic flux program (ofp)/bermuda atlantic time series (bats) site in the western sargasso sea near bermuda. *Deep Sea Research Part II: Topical Studies in Oceanography*, 48(8-9):1471–1505.

Courant, R., Friedrichs, K., and Lewy, H. (1967). On the partial difference equations of mathematical physics. *IBM journal of Research and Development*, 11(2):215–234.

Damerell, G. M., Heywood, K. J., Thompson, A. F., Binetti, U., and Kaiser, J. (2016). The vertical structure of upper ocean variability at the porcupine abyssal plain during 2012–2013. *Journal of Geophysical Research: Oceans*, 121(5):3075–3089.

de Boyer Montégut, C., Madec, G., Fischer, A. S., Lazar, A., and Iudicone, D. (2004). Mixed layer depth over the global ocean: An examination of profile data and a profile-based climatology. *Journal of Geophysical Research: Oceans*, 109(C12).

De La Fuente, R., Drótos, G., Hernández-García, E., López, C., and Van Sebille, E. (2021). Sinking microplastics in the water column: simulations in the mediterranean sea. *Ocean Science*, 17(2):431–453.

Deuser, W., Muller-Karger, F. E., and Hemleben, C. (1988). Temporal variations of particle fluxes in the deep subtropical and tropical north atlantic: Eulerian versus lagrangian effects. *Journal of Geophysical Research: Oceans*, 93(C6):6857–6862.

Deuser, W. and Ross, E. (1980). Seasonal change in the flux of organic carbon to the deep sargasso sea. *Nature*, 283:364–365.

Deuser, W., Ross, E., and Anderson, R. (1981). Seasonality in the supply of sediment to the deep sargasso sea and implications for the rapid transfer of matter to the deep ocean. *Deep Sea Research Part A. Oceanographic Research Papers*, 28(5):495–505.

Dever, M., Nicholson, D., Omand, M., and Mahadevan, A. (2021). Size-differentiated export flux in different dynamical regimes in the ocean. *Global Biogeochemical Cycles*, 35(3).

Döös, K., Rupolo, V., and Brodeau, L. (2011). Dispersion of surface drifters and model-simulated trajectories. *Ocean Modelling*, 39(3-4):301–310.

Ducet, N., Le Traon, P.-Y., and Reverdin, G. (2000). Global high-resolution mapping of ocean circulation from topex/poseidon and ers-1 and-2. *Journal of Geophysical Research: Oceans*, 105(C8):19477–19498.

D'Asaro, E., Shcherbina, A., Klymak, J., Molemaker, J., Novelli, G., Guigand, C., Haza, A., Haus, B., Ryan, E., Jacobs, G., Huntley, H., Laxague, N., Chen, S., Judt, F., McWilliams, J., Barkan, R., Kirwan, A., Poje, A., and Özgökmen, T. (2018). Ocean convergence and the dispersion of flotsam. *Proceedings of the National Academy of Sciences*, 115(6):1162–1167.

d'Ovidio, F., De Monte, S., Alvain, S., Dandonneau, Y., and Lévy, M. (2010). Fluid dynamical niches of phytoplankton types. *Proceedings of the National Academy of Sciences*, 107(43):18366–18370.

Eppley, R. W. and Peterson, B. J. (1979). Particulate organic matter flux and planktonic new production in the deep ocean. *Nature*, 282(5740):677–680.

Erickson, Z. K. and Thompson, A. F. (2018). The Seasonality of Physically Driven Export at Submesoscales in the Northeast Atlantic Ocean. *Global Biogeochemical Cycles*.

Estapa, M., Feen, M., and Breves, E. (2019). Direct observations of biological carbon export from profiling floats in the subtropical north atlantic. *Global Biogeochemical Cycles*, 33(3):282–300.

Estapa, M., Siegel, D., Buesseler, K., Stanley, R., Lomas, M., and Nelson, N. (2015). Decoupling of net community and export production on submesoscales in the sargasso sea. *Global Biogeochemical Cycles*, 29(8):1266–1282.

Ferrari, R. and Wunsch, C. (2009). Ocean circulation kinetic energy: Reservoirs, sources, and sinks. *Annual Review of Fluid Mechanics*, 41:253–282.

Francois, R., Honjo, S., Krishfield, R., and Manganini, S. (2002). Factors controlling the flux of organic carbon to the bathypelagic zone of the ocean. *Global Biogeochemical Cycles*, 16(4):34–1.

Freilich, M. and Mahadevan, A. (2021). Coherent pathways for subduction from the surface mixed layer at ocean fronts. *Journal of Geophysical Research: Oceans*, 126(5):e2020JC017042.

Frigstad, H., Henson, S., Hartman, S., Omar, A., Jeansson, E., Cole, H., Pebody, C., and Lampitt, R. (2015). Links between surface productivity and deep ocean particle flux at the porcupine abyssal plain sustained observatory. *Biogeosciences*, 12(19):5885–5897.

Gaillard, F., Reynaud, T., Thierry, V., Kolodziejczyk, N., and von Schuckmann, K. (2016). In situ–based reanalysis of the global ocean temperature and salinity with isas: Variability of the heat content and steric height. *Journal of Climate*, 29(4):1305–1323.

Garçon, V. C., Oschlies, A., Doney, S. C., McGillicuddy, D., and Waniek, J. (2001). The role of mesoscale variability on plankton dynamics in the north atlantic. *Deep Sea Research Part II: Topical Studies in Oceanography*, 48(10):2199–2226.

Gaube, P., McGillicuddy Jr, D. J., Chelton, D. B., Behrenfeld, M. J., and Strutton, P. G. (2014). Regional variations in the influence of mesoscale eddies on near-surface chlorophyll. *Journal of Geophysical Research: Oceans*, 119(12):8195–8220.

Guidi, L., Calil, P., Duhamel, S., Björkman, K., Doney, S., Jackson, G., Li, B., Church, M., Tozzi, S.and Kolber, Z., Richards, K., Fong, A., Letelier, R., Gorsky, G., Stemmann, L., and Karl, D. (2012). Does eddy-eddy interaction control surface phytoplankton distribution and carbon export in the north pacific subtropical gyre? *Journal of Geophysical Research: Biogeosciences*, 117(G2).

Guidi, L., Stemmann, L., Legendre, L., Picheral, M., Prieur, L., and Gorsky, G. (2007). Vertical distribution of aggregates (¿ 110 μm) and mesoscale activity in the northeastern atlantic: Effects on the deep vertical export of surface carbon. *Limnology and Oceanography*, 52(1):7–18.

Gula, J., Blacic, T. M., and Todd, R. E. (2019). Submesoscale coherent vortices in the gulf stream. *Geophysical Research Letters*, 46(5):2704–2714.

Gula, J. and Collin, J. (2021). Pyticles: a Python/Fortran hybrid parallelized code for 3D Lagrangian particles advection using ROMS/CROCO model data.

Gula, J., Molemaker, M. J., and McWilliams, J. C. (2014). Submesoscale cold filaments in the gulf stream. *Journal of Physical Oceanography*, 44(10):2617–2643.

Gula, J., Molemaker, M. J., and McWilliams, J. C. (2016). Submesoscale dynamics of a gulf stream frontal eddy in the south atlantic bight. *Journal of Physical Oceanography*, 46(1):305–325.

Hartman, S., Larkin, K., Lampitt, R., Lankhorst, M., and Hydes, D. (2010). Seasonal and inter-annual biogeochemical variations in the porcupine abyssal plain 2003–2005 associated with winter mixing and surface circulation. *Deep Sea Research Part II: Topical Studies in Oceanography*, 57(15):1303–1312.

Henson, S. A., Sanders, R., Madsen, E., Morris, P. J., Le Moigne, F., and Quartly, G. D. (2011). A reduced estimate of the strength of the ocean's biological carbon pump. *Geophysical Research Letters*, 38(4).

Henson, S. A., Yool, A., and Sanders, R. (2015). Variability in efficiency of particulate organic carbon export: A model study. *Global Biogeochemical Cycles*, 29(1):33–45.

Hisaki, Y. (2013). Classification of surface current maps. *Deep Sea Research Part I: Oceanographic Research Papers*, 73:117–126.

Honjo, S. (1982). Seasonality and interaction of biogenic and lithogenic particulate flux at the panama basin. *Science*, 218(4575):883–884.

Jokulsdottir, T. and Archer, D. (2016). A stochastic, lagrangian model of sinking biogenic aggregates in the ocean (slams 1.0): model formulation, validation and sensitivity. *Geoscientific Model Development*, 9(4):1455–1476.

Jónasdóttir, S. H., Visser, A. W., Richardson, K., and Heath, M. R. (2015). Seasonal copepod lipid pump promotes carbon sequestration in the deep north atlantic. *Proceedings of the National Academy of Sciences*, 112(39):12122–12126.

Klein, P. and Lapeyre, G. (2009). The oceanic vertical pump induced by mesoscale and submesoscale turbulence. *Annual review of marine science*, 1:351–375.

Klein, P., Lapeyre, G., Siegelman, L., Qiu, B., Fu, L.-L., Torres, H., Su, Z., Menemenlis, D., and Le Gentil, S. (2019). Ocean-scale interactions from space. *Earth and Space Science*, 6(5):795–817.

Klymak, J. M., Shearman, R. K., Gula, J., Lee, C. M., D'Asaro, E. A., Thomas, L. N., Harcourt, R. R., Shcherbina, A. Y., Sundermeyer, M. A., Molemaker, J., et al. (2016). Submesoscale streamers exchange water on the north wall of the gulf stream. *Geophysical Research Letters*, 43(3):1226–1233.

Kostadinov, T., Siegel, D., and Maritorena, S. (2009). Retrieval of the particle size distribution from satellite ocean color observations. *Journal of Geophysical Research*, 114(C9):C09015.

LaCasce, J. (2008). Statistics from lagrangian observations. *Progress in Oceanography*, 77(1):1–29.

Lampitt, R. and Antia, A. (1997). Particle flux in deep seas: regional characteristics and temporal variability. *Deep Sea Research Part I: Oceanographic Research Papers*, 44(8):1377–1403.

Lampitt, R., Billett, D., and Martin, A. (2010). The sustained observatory over the porcupine abyssal plain (pap): Insights from time series observations and process studies.

Le Cann, B. (2005). Observed mean and mesoscale upper ocean circulation in the midlatitude northeast atlantic. *Journal of Geophysical Research*, 110(C7):C07S05.

Le Corre, M., Gula, J., and Tréguier, A.-M. (2020). Barotropic vorticity balance of the north atlantic subpolar gyre in an eddy-resolving model. *Ocean Science*, 16(2):451–468.

Lehahn, Y., d'Ovidio, F., Lévy, M., Amitai, Y., and Heifetz, E. (2011). Long range transport of a quasi isolated chlorophyll patch by an agulhas ring. *Geophysical Research Letters*, 38(16).

Lévy, M. and Martin, A. P. (2013). The influence of mesoscale and submesoscale heterogeneity on ocean biogeochemical reactions. *Global Biogeochemical Cycles*, 27(4):1139–1150.

Liu, G., Bracco, A., and Passow, U. (2018). The influence of mesoscale and submesoscale circulation on sinking particles in the northern gulf of mexico. *Elemnta: Science of the Anthropocene*, 6(1):36.

Llort, J., Langlais, C., Matear, R., Moreau, S., Lenton, A., and Strutton, P. G. (2018). Evaluating southern ocean carbon eddy-pump from biogeochemical-argo floats. *Journal of Geophysical Research: Oceans*, 123(2):971–984.

Lüthi, D., Le Floch, M., Bereiter, B., Blunier, T., Barnola, J.-M., Siegenthaler, U., Raynaud, D., Jouzel, J., Fischer, H., Kawamura, K., et al. (2008). High-resolution carbon dioxide concentration record 650,000–800,000 years before present. *Nature*, 453(7193):379–382.

Lévy, M., Ferrari, R., Franks, P., Martin, A., and Rivière, P. (2012). Bringing physics to life at the submesoscale. *Geophysical Research Letters*, 39(14):L14602.

Lévy, M., Franks, P., and Smith, K. (2018). The role of submesoscale currents in structuring marine ecosystems. *Nature Communications*, 9(1):4758.

Lévy, M., Jahn, O., Dutkiewicz, S., and Follows, M. (2014). Phytoplankton diversity and community structure affected by oceanic dispersal and mesoscale turbulence: Dispersal impact on plankton diversity. *Limnology and Oceanography: Fluids and Environments*, 4(1):67–84.

Ma, W., Xiu, P., Chai, F., Ran, L., Wiesner, M. G., Xi, J., Yan, Y., and Fredj, E. (2021). Impact of mesoscale eddies on the source funnel of sediment trap measurements in the south china sea. *Progress in Oceanography*, 194:102566.

Mahadevan, A. (2016). The impact of submesoscale physics on primary productivity of plankton. *Annual Review of Marine Science*, 8(1):161–184.

Mahadevan, A. and Tandon, A. (2006). An analysis of mechanisms for submesoscale vertical motion at ocean fronts. *Ocean Modelling*, 14(3-4):241–256.

Mahadevan, A., Thomas, L. N., and Tandon, A. (2008). Comment on" eddy/wind interactions stimulate extraordinary mid-ocean plankton blooms". *science*, 320(5875):448–448.

Martin, A. (2003). Phytoplankton patchiness: the role of lateral stirring and mixing. *Progress in oceanography*, 57(2):125–174.

Martin, A., Boyd, P., Buesseler, K., Cetinic, I., Claustre, H., Giering, S., Henson, S., Irigoien, X., Kriest, I., Memery, L., Robinson, C., Saba, G., Sanders, R., Siegel, D., Villa, M., and Guidi, L. (2020). Study the twilight zone before it is too late. *Nature*, 580:26–28.

Martin, A. P. and Richards, K. J. (2001). Mechanisms for vertical nutrient transport within a north atlantic mesoscale eddy. *Deep Sea Research Part II: Topical Studies in Oceanography*, 48(4-5):757–773.

Martin, J. H., Knauer, G. A., Karl, D. M., and Broenkow, W. W. (1987). Vertex: carbon cycling in the northeast pacific. *Deep Sea Research Part A. Oceanographic Research Papers*, 34(2):267–285.

McGillicuddy, D. J. (2016). Mechanisms of physical-biological-biogeochemical interaction at the oceanic mesoscale. *Annual Review of Marine Science*, 8:125–159.

McGillicuddy, D. J., Anderson, L. A., Bates, N. R., Bibby, T., Buesseler, K. O., Carlson, C. A., Davis, C. S., Ewart, C., Falkowski, P. G., Goldthwait, S. A., et al. (2007). Eddy/wind interactions stimulate extraordinary mid-ocean plankton blooms. *Science*, 316(5827):1021–1026.

Mcgillicuddy, D. J., Resplandy, L., and Lévy, M. (2019). Estimating particle export flux from satellite observations: Challenges associated with spatial and temporal decoupling of production and export. *Journal of marine research*, 77(2):247–258.

McWilliams, J. C. (2016). Submesoscale currents in the ocean. *Proceedings of the Royal Society A: Mathematical, Physical and Engineering Sciences*, 472(2189):20160117.

Naveira Garabato, A. et al. (2013). Rrs james cook cruise 090, 30 aug-17 sep 2013. ocean surface mixing, ocean sub-mesoscale interaction study (osmosis).

Nowicki, M., DeVries, T., and Siegel, D. A. (2022). Quantifying the carbon export and sequestration pathways of the ocean's biological carbon pump. *Global Biogeochemical Cycles*, 36(3):e2021GB007083.

Olson, D. B. (1991). Rings in the ocean. *Annual Review of Earth and Planetary Sciences*, 19(1):283–311.

Omand, M. M., D'Asaro, E. A., Lee, C. M., Perry, M. J., Briggs, N., Cetinić, I., and Mahadevan, A. (2015). Eddy-driven subduction exports particulate organic carbon from the spring bloom. *Science*, 348(6231):222–225.

Painter, S. C., Pidcock, R. E., and Allen, J. T. (2010). A mesoscale eddy driving spatial and temporal heterogeneity in the productivity of the euphotic zone of the northeast atlantic. *Deep Sea Research Part II: Topical Studies in Oceanography*, 57(15):1281–1292.

Parekh, P., Dutkiewicz, S., Follows, M., and Ito, T. (2006). Atmospheric carbon dioxide in a less dusty world. *Geophysical research letters*, 33(3).

Passow, U. and Carlson, C. A. (2012). The biological pump in a high co2 world. *Marine Ecology Progress Series*, 470:249–271.

Poje, A., Ozgokmen, T., Lipphardt, B., Haus, B., Ryan, E., Haza, A., Jacobs, G., Reniers, A., Olascoaga, M., Novelli, G., Griffa, A., Beron-Vera, F., Chen, S., Coelho, E., Hogan, P., Kirwan, A., Huntley, H., and Mariano, A. (2014). Submesoscale dispersion in the vicinity of the deepwater horizon spill. *Proceedings of the National Academy of Sciences*, 111(35):12693–12698.

Puigcorbé Lacueva, V. (2016). *Use of 234Th: 238U disequilibrium to estimate particulate organic carbon export in the upper ocean*. Universitat Autònoma de Barcelona.

Qiu, B., Scott, R. B., and Chen, S. (2008). Length scales of eddy generation and nonlinear evolution of the seasonally modulated south pacific subtropical countercurrent. *Journal of Physical Oceanography*, 38(7):1515–1528.

Qiu, Z., Doglioli, A., and Carlotti, F. (2014). Using a lagrangian model to estimate source regions of particles in sediment traps. *Science China Earth Sciences*, 57:2447–2456.

Resplandy, L., Lévy, M., and McGillicuddy Jr, D. J. (2019). Effects of eddy-driven subduction on ocean biological carbon pump. *Global Biogeochemical Cycles*, 33(8):1071–1084.

Riley, J. S., Sanders, R., Marsay, C., Le Moigne, F. A. C., Achterberg, E. P., and Poulton, A. J. (2012). The relative contribution of fast and slow sinking particles to ocean carbon export. *Global Biogeochemical Cycles*, 26(1).

Robinson, A. R. (1983). *Eddies in marine science*. Clarendon Press.

Rocha, C. B., Gille, S. T., Chereskin, T. K., and Menemenlis, D. (2016). Seasonality of submesoscale dynamics in the kuroshio extension. *Geophysical Research Letters*, 43(21):11–304.

Ruhl, H. A., Bahr, F. L., Henson, S. A., Hosking, W. B., Espinola, B., Kahru, M., Daniel, P., Drake, P., and Edwards, C. A. (2020). Understanding the remote influences of ocean weather on the episodic pulses of particulate organic carbon flux. *Deep Sea Research Part II: Topical Studies in Oceanography*, 173:104741.

Samuelsen, A., Hjøllo, S. S., Johannessen, J. A., and Patel, R. (2012). Particle aggregation at the edges of anticyclonic eddies and implications for distribution of biomass. *Ocean Science*, 8(3):389–400.

Sarmiento, J. L. and Gruber, N. (2006). *Ocean Biogeochemical Dynamics*. Princeton University Press.

Sayre, R. G., Wright, D. J., Breyer, S. P., Butler, K. A., Graafeiland, K. V., Costello, M. J., Harris, P. T., Goodin, K. L., Guinotte, J. M., Basher, Z., Kavanaugh, M. T., Halpin, P. N., Monaco, M. E., Cressie, N., Aniello, P., Frye, C. E., and Stephens, D. (2017). A three-dimensional mapping of the ocean based on environmental data. *Oceanography*, 30(1).

Schubert, R., Gula, J., Greatbatch, R. J., Baschek, B., and Biastoch, A. (2020). The submesoscale kinetic energy cascade: Mesoscale absorption of submesoscale mixed layer eddies and frontal downscale fluxes.

Schubert, R., Vergara, O., and Gula, J. (2023). The open ocean kinetic energy cascade is strongest in late winter and spring.

Shchepetkin, A. F. and McWilliams, J. C. (2005). The regional oceanic modeling system (ROMS): a split-explicit, free-surface, topography-following-coordinate oceanic model. *Ocean Modelling*, 9(4):347–404.

Shcherbina, A. Y., D'Asaro, E. A., Lee, C. M., Klymak, J. M., Molemaker, M. J., and McWilliams, J. C. (2013). Statistics of vertical vorticity, divergence, and strain in a developed submesoscale turbulence field. *Geophysical Research Letters*, 40(17):4706–4711.

Siegel, D., Buesseler, K., Doney, S. C., Sailley, S., Behrenfeld, M. J., and Boyd, P. (2014). Global assessment of ocean carbon export by combining satellite observations and food-web models. *Global Biogeochemical Cycles*, 28(3):181–196.

Siegel, D. and Deuser, W. (1997). Trajectories of sinking particles in the sargasso sea: modeling of statistical funnels above deep-ocean sediment traps. *Deep Sea Research Part I: Oceanographic Research Papers*, 44:1519–1541.

Siegel, D., Fields, E., and Buesseler, K. (2008). A bottom-up view of the biological pump: Modeling source funnels above ocean sediment traps. *Deep Sea Research Part I: Oceanographic Research Papers*, 55(1):108–127.

Siegel, D., Granata, T., Michaels, A., and Dickey, T. (1990). Mesoscale eddy diffusion, particle sinking, and the interpretation of sediment trap data. *Journal of Geophysical Research*, 95(C4):5305.

Siegel, D. A., Buesseler, K. O., Behrenfeld, M. J., Benitez-Nelson, C. R., Boss, E., Brzezinski, M. A., Burd, A., Carlson, C. A., D'Asaro, E. A., Doney, S. C., et al. (2016). Prediction of the export and fate of global ocean net primary production: The exports science plan. *Frontiers in Marine Science*, 3:22.

Siegel, D. A., McGillicuddy Jr, D. J., and Fields, E. A. (1999). Mesoscale eddies, satellite altimetry, and new production in the sargasso sea. *Journal of Geophysical Research: Oceans*, 104(C6):13359–13379.

Siegelman, L., Klein, P., Rivière, P., Thompson, A. F., Torres, H. S., Flexas, M., and Menemenlis, D. (2020). Enhanced upward heat transport at deep submesoscale ocean fronts. *Nature Geoscience*, 13(1):50–55.

Srinivasan, K., McWilliams, J. C., Renault, L., Hristova, H. G., Molemaker, J., and Kessler, W. S. (2017). Topographic and mixed layer submesoscale currents in the near-surface southwestern tropical pacific. *Journal of Physical Oceanography*, 47(6):1221–1242.

Steinberg, D. K., Carlson, C. A., Bates, N. R., Johnson, R. J., Michaels, A. F., and Knap, A. H. (2001). Overview of the us jgofs bermuda atlantic time-series study (bats): a decade-scale look at ocean biology and biogeochemistry. *Deep Sea Research Part II: Topical Studies in Oceanography*, 48(8-9):1405–1447.

Stukel, M. R. and Ducklow, H. W. (2017). Stirring up the biological pump: Vertical mixing and carbon export in the southern ocean. *Global Biogeochemical Cycles*, 31(9):1420–1434.

Stukel, M. R., Song, H., Goericke, R., and Miller, A. J. (2018). The role of subduction and gravitational sinking in particle export, carbon sequestration, and the remineralization length scale in the california current ecosystem. *Limnology and Oceanography*, 63(1):363–383.

Sun, Q., Little, C. M., Barthel, A. M., and Padman, L. (2021). A clustering-based approach to ocean model–data comparison around antarctica. *Ocean Science*, 17(1):131–145.

Taylor, J. R. and Ferrari, R. (2011). Ocean fronts trigger high latitude phytoplankton blooms. *Geophysical Research Letters*, 38(23).

Taylor, J. R., Smith, K. M., and Vreugdenhil, C. A. (2020). The influence of submesoscales and vertical mixing on the export of sinking tracers in large-eddy simulations. *Journal of Physical Oceanography*, 50(5):1319–1339.

Thomas, L. N., Tandon, A., and Mahadevan, A. (2008). Submesoscale processes and dynamics. In Hecht, M. W. & Hasumi, H., editor, *Ocean Modeling an Eddying Regime*, volume 177. American Geophysical Union.

Thompson, A. F., Lazar, A., Buckingham, C., Garabato, A. C. N., Damerell, G. M., and Heywood, K. J. (2016). Open-ocean submesoscale motions: A full seasonal cycle of mixed layer instabilities from gliders. *Journal of Physical Oceanography*, 46(4):1285–1307.

Trull, T., Bray, S., Buesseler, K., Lamborg, C., Manganini, S., Moy, C., and Valdes, J. (2008). In situ measurement of mesopelagic particle sinking rates and the control of carbon transfer to the ocean interior during the vertical flux in the global ocean (vertigo) voyages in the north pacific. *Deep Sea Research Part II: Topical Studies in Oceanography*, 55(14-15):1684–1695.

Umlauf, L. and Burchard, H. (2003). A generic length-scale equation for geophysical turbulence models. *Journal of Marine Research*, 61(2):235–265.

van Sebille, E., Griffies, S. M., Abernathey, R., Adams, T. P., Berloff, P., Biastoch, A., Blanke, B., Chassignet, E. P., Cheng, Y., Cotter, C. J., et al. (2018). Lagrangian ocean analysis: Fundamentals and practices. *Ocean Modelling*, 121:49–75.

Vic, C., Gula, J., Roullet, G., and Pradillon, F. (2018). Dispersion of deep-sea hydrothermal vent effluents and larvae by submesoscale and tidal currents. *Deep Sea Research Part I: Oceanographic Research Papers*, 133:1–18.

Vic, C., Hascoët, S., Gula, J., Huck, T., and Maes, C. (2022). Oceanic Mesoscale Cyclones Cluster Surface Lagrangian Material. *Geophysical Research Letters*, 49(4):e2021GL097488.

Vic, C., Roullet, G., Capet, X., Carton, X., Molemaker, M. J., and Gula, J. (2015). Eddy-topography interactions and the fate of the p ersian g ulf o utflow. *Journal of Geophysical Research: Oceans*, 120(10):6700–6717.

Villa-Alfageme, M., de Soto, F., Le Moigne, F. A. C., Giering, S. L. C., Sanders, R., and García-Tenorio, R. (2014). Observations and modeling of slow-sinking particles in the twilight zone. *Global Biogeochemical Cycles*, 28(11):1327–1342.

Volk, T. and Hoffert, M. I. (1985). Ocean carbon pumps: Analysis of relative strengths and efficiencies in ocean-driven atmospheric co2 changes. *The carbon cycle and atmospheric CO2: natural variations Archean to present*, 32:99–110.

Waite, A., Stemmann, L.and Guidi, L., Calil, P., Hogg, A., Feng, M., Thompson, P., Picheral, M., and Gorsky, G. (2016). The wineglass effect shapes particle export to the deep ocean in mesoscale eddies: The wineglass effect. *Geophysical Research Letters*, 43(18):9791–9800.

Wang, L., Gula, J., Collin, J., and Mémery, L. (2022). Effects of mesoscale dynamics on the path of fast-sinking particles to the deep ocean: A modeling study. *Journal Of Geophysical Research-oceans*, 127(7).

Waniek, J., Koeve, W., and Prien, R. (2000). Trajectories of sinking particles and the catchment areas above sediment traps in the northeast atlantic. *Journal of Marine Research*, 58:983–1006.

Waniek, J. J., Schulz-Bull, D. E., Blanz, T., Prien, R. D., Oschlies, A., and Müller, T. J. (2005). Interannual variability of deep water particle flux in relation to

production and lateral sources in the northeast atlantic. *Deep Sea Research Part I: Oceanographic Research Papers*, 52(1):33–50.

Wekerle, C., Krumpen, T., Dinter, T., von Appen, W.-J., Iversen, M., and Salter, I. (2018). Properties of sediment trap catchment areas in fram strait: Results from lagrangian modeling and remote sensing. *Frontiers in Marine Science*, 5:407.

Wong, C., Whitney, F., Crawford, D., Iseki, K., Matear, R., Johnson, W., Page, J., and Timothy, D. (1999). Seasonal and interannual variability in particle fluxes of carbon, nitrogen and silicon from time series of sediment traps at ocean station p, 1982–1993: Relationship to changes in subarctic primary productivity. *Deep Sea Research Part II: Topical Studies in Oceanography*, 46(11-12):2735–2760.

Wunsch, C. (1981). Low-frequency variability of the sea. *Evolution of physical oceanography*, 342:374.

Wunsch, C. (1998). The work done by the wind on the oceanic general circulation. *Journal of Physical Oceanography*, 28(11):2332–2340.

Yu, X., Garabato, A. C. N., Martin, A. P., Buckingham, C. E., Brannigan, L., and Su, Z. (2019a). An annual cycle of submesoscale vertical flow and restratification in the upper ocean. *Journal of Physical Oceanography*, 49(6):1439–1461.

Yu, X., Naveira Garabato, A. C., Martin, A. P., Gwyn Evans, D., and Su, Z. (2019b). Wind-forced symmetric instability at a transient mid-ocean front. *Geophysical Research Letters*, 46(20):11281–11291.

Zhang, Z., Qiu, B., Klein, P., and Travis, S. (2019). The influence of geostrophic strain on oceanic ageostrophic motion and surface chlorophyll. *Nature Communications*, 10(1):2838.

Zhou, K., Dai, M., Kao, S.-J., Wang, L., Xiu, P., Chai, F., Tian, J., and Liu, Y. (2013). Apparent enhancement of 234th-based particle export associated with anticyclonic eddies. *Earth and Planetary Science Letters*, 381:198–209.

Zhou, K., Dai, M., Xiu, P., Wang, L., Hu, J., and Benitez-Nelson, C. R. (2020). Transient enhancement and decoupling of carbon and opal export in cyclonic eddies. *Journal of Geophysical Research: Oceans*, 125(9):e2020JC016372.

COLLEGE SCIENCES DOCTORAL DE LA MER BRETAGNE ET DU LITTORAL

Université de Bretagne Occidentale

Titre : Impact de la dynamique à petite et moyenne échelles sur le devenir des particules exportées dans l'océan profond

Mots clés : particules qui sédimentent, impacts de la dynamique à mésoéchelle et à sous-mésoéchelle, pièges à particules profonds

Résumé : Les observations à long terme du flux de particules qui sédimentent sont principalement effectuées par des pièges à particules profonds. Dans cette thèse, les impacts de la dynamique à mésoéchelle et à sous-mésoéchelle sur l'export de particules qui s'enfoncent rapidement sont étudiés par le biais d'expériences de suivi lagrangien de particules, backward et forward, en utilisant les résultats d'une simulation à 2 km de résolution de l'océan Atlantique Nord sur une période de 7 ans. Les rétrotrajectoires montrent que les tourbillons de mésoéchelle peuvent transporter des particules sur des centaines de kilomètres jusqu'aux pièges à particules du site de l'observatoire à long terme PAP (16.5°W, 49.0°N). La variabilité mensuelle des sources de particules montre qu'un tourbillon localement dominant sur le site PAP peut piéger efficacement les particules dans un domaine restreint. En partant d'un ensemencement homog`ene de particules à 200 m, les simulations forward révèlent que la saisonnalité et la variabilité spatiale des collectes de particules à 1000 m peuvent résulter uniquement de la dynamique océanique. Analyse de clustering de particules recueillies dans une zone cible de 200 × 200 km suggère les variations saisonnières du nombre de particules dans les classes majoritaires en hiver et au printemps sont liées aux activités tourbillonnaires à mésoéchelle et au développement des fronts. En automne et au début de l'hiver, les classes les plus importantes de particules sont avant tout associées à une dynamique local 'de fond' (définie par de faibles activités tourbillonnaires et frontales)..

Title : Impacts of mesoscale and submesoscale dynamics on the fate of exported particles to the deep ocean

Keywords : sinking particles, mesoscale and submesoscale dynamics, deep-moored sediment traps

Abstract : Long-term observations of the downward particle flux are mainly made by deep-moored sediment traps. In this thesis, impacts of mesoscale and submesoscale dynamics on the export of fast-sinking particles are investigated through backward and forward Lagrangian particle tracking experiments, using outputs from a 2-km resolution simulation of the North Atlantic Ocean over 7 years. The backward simulations show that mesoscale eddies can transport particles from hundreds of kilometers to sediment traps at the long-term observatory PAP site (16.5°W, 49.0°N). The variability of monthly particle sources shows a locally dominant eddy at the PAP site can significantly trap particles within a small region. Starting with a homogeneous seeding of particles at 200m, the forward simulations reveal that the seasonality and spatial variability of particle collections at 1000 m can result from the physical dynamics only. Clustering analysis of particles collected within a 200 × 200 km target zone suggests the seasonal variations of particle amounts In clusters active in winter-spring time are related to the mesoscale eddy activities and the development of fronts. In autumn and early winter, the local background flow (defined by low eddy and frontal activities) contributes most to the particle collection. The results demonstrates how mesoscale dynamics impact the heterogeneity of particle distribution, and thus collection in the deep ocean.